A Data-Driven Neuromuscular Model of Walking and its Application to Prosthesis Control

by

Jared Markowitz

B.S., Carnegie Mellon University (2004)

Submitted to the Department of Physics
in partial fulfillment of the requirements for the degree of

Doctor of Philosophy

at the

MASSACHUSETTS INSTITUTE OF TECHNOLOGY

June 2013

Author .....
Department of Physics
May 24, 2013

Certified by .....
Hugh M. Herr
Associate Professor
Thesis Supervisor

Certified by .....
Leonid A. Mirny
Associate Professor
Thesis Supervisor

Accepted by .....
John Belcher
Associate Department Head for Education

A Data-Driven Neuromuscular Model of Walking and its Application to Prosthesis Control

by

Jared Markowitz

Submitted to the Department of Physics
on May 24, 2013, in partial fulfillment of the
requirements for the degree of
Doctor of Philosophy

Abstract

In this thesis we present a data-driven neuromuscular model of human walking and its application to prosthesis control. The model is novel in that it leverages tendon elasticity to more accurately predict the metabolic consumption of walking than conventional models. Paired with a reflex-based neural drive the model has been applied in the control of a robotic ankle-foot prosthesis, producing speed adaptive behavior.

Current neuromuscular models significantly overestimate the metabolic demands of walking. We believe this is because they do not adequately consider the role of elasticity; specifically the parameters that govern the force-length relations of tendons in these models are typically taken from published values determined from cadaver studies. To investigate this issue we first collected kinematic, kinetic, electromyographic (EMG), and metabolic data from five subjects walking at six different speeds. The kinematic and kinetic data were used to estimate muscle lengths, muscle moment arms, and joint moments while the EMG data were used to estimate muscle activations. For each subject we performed a kinematically clamped optimization, varying the parameters that govern the force-length curve of each tendon while simultaneously seeking to minimize metabolic cost and maximize agreement with the observed joint moments. We found a family of parameter sets that excel at both objectives, providing agreement with both the collected kinetic and metabolic data. This identification allows us to accurately predict the metabolic cost of walking as well as the force and state of individual muscles, lending insight into the roles and control objectives of different muscles throughout the gait cycle.

This optimized muscle-tendon morphology was then applied with an optimized linear reflex architecture in the control of a powered ankle-foot prosthesis. Specifically, the model was fed the robot's angle and state and used to command output torque. Clinical trials were conducted that demonstrated speed adaptive behavior; commanded net work was seen to increase with walking speed. This result supports both the efficacy of the modeling approach and its potential utility in controlling life-like prosthetic limbs.

Thesis Supervisor: Hugh M. Herr
Title: Associate Professor

Thesis Supervisor: Leonid A. Mirny
Title: Associate Professor

Acknowledgments

There are many people I need to thank for helping me complete my thesis work and navigate through my time at MIT. First I must thank Hugh for his guidance, for being a source of inspiration, and for his belief in me. I very much appreciate him giving me the chance to work in the Biomechatronics group and the generosity he has exhibited towards me over the years. I also appreciate the guidance given to me by my thesis committee- Leonid Mirny, Mehran Kardar, and Jeff Gore. I thoroughly enjoyed the classes they taught me here and greatly value both the thoughts they had about my project and the patience they displayed as I rushed to complete this work.

I've also been quite fortunate to encounter several extremely helpful people from other institutions. I owe a huge debt of gratitude to Peter Loan, the author of the SIMM software. Peter has been an invaluable resource the last few years and without his help this thesis would not have been possible[1]. I'd like to thank Dan Lieberman for his generosity in letting me use his motion capture facility as well as Adam Daoud and Anna Warrener for helping me troubleshoot the system. I have also received extremely helpful advice about my work from Brian Umberger, Alena Grabowski, Cara Lewis, and Greg Sawicki. It is truly a privilege to work in a field with so many talented, helpful, and generally exceptional people.

One of the dominant factors in determining the quality of one's graduate career is the environment of their research group. I've been lucky enough to work in a group full of committed, gifted, and friendly people. We have all greatly benefited from the efforts of our administrator, Sarah Hunter, who is truly the glue that holds the group together. We have also all benefited from the excellent advice provided by Bruce Deffenbaugh, who always seems to turn up when most needed. I personally have been privileged to share an office with some of the best and brightest that MIT has to offer- Andy Marecki, David Sengeh (the future president of Sierra Leone), and Luke Mooney. I truly admire the work that they do and greatly appreciate them putting up with my idiosyncrasies. I also must thank Michael Eilenberg and Grant Elliott,

[1]Peter is so committed to helping SIMM users that he brought me a water bottle while I was running the 2011 Chicago Marathon. Pretty exceptional customer service.

who helped me get through some rough times in the lab and have generally been good and loyal friends. I would be remiss not to mention Ernesto Martinez-Villalpando, Ken Endo, David Hill, Madalyn Berns, Pavitra Krishnaswamy, Jiun-Yih Kuan, Reza Safai-naeeni, Elliott Rouse, Olli Kannape, Todd Farrell, and Arthur Petron- it has been a pleasure to work with all of you.

I must also thank my friends and family. I've been lucky enough to make many great friends during my time in Cambridge through the lab, the Tech Catholic Community, and through running. They have greatly brightened my time here and generally made the experience worthwhile. Finally I would like to thank my family- parents Jared and Mary Helen and siblings Geoffrey, Anna, and Kathryn. It is hard to overstate how blessed I am to have them, and it is to them that I dedicate this thesis.

Contents

List of Figures

List of Tables

Chapter 1

Introduction

Bipedal walking relies upon a complex interplay of several different physiological systems. The nervous system directs muscle contraction while receiving feedback on muscle force and state. The muscles actuate the skeleton through elastic structures known as tendons. The skeleton interacts with the environment, which is in turn sensed by the nervous system. This highly coordinated network relies on the function of many different neural and structural components. In this thesis we focus on the latter, evaluating the role of tendon compliance during locomotion.

Tendons vary in shape, size, and function depending on the requirements of the muscles to which they are attached. As the interface between muscle and bone, their properties determine how muscles move. Muscle force, state, and metabolic consumption are all affected by the structural properties of tendon, yet these properties are rarely evaluated in depth. Here we show how proper consideration of these elastic elements can lend insight into the roles of individual muscles during walking as well as improve metabolic cost predictions. We build a data-driven model of human walking that emphasizes the role of compliance and then apply it in the control of a robotic ankle-foot prosthesis.

1.1 Context

Many different approaches have been taken to model human walking. On one side of the spectrum are purely mechanical systems, such as inverse pendulum walkers and passive dynamic robots [48, 11]. In many cases these systems are able to reproduce the gross mechanical features of gait, but must be properly tuned and do not address the sources of skeletal actuation. On the other side are large scale dynamic optimizations [3, 39], which seek to model as many muscles of the leg as possible. These models make some successful predictions but typically significantly overestimate metabolic consumption. The model presented in this thesis represents a middle ground between these two extremes. Below we discuss some previous modeling efforts so as to lend context to the current approach.

1.1.1 Inverse Modeling

Inverse models of locomotion use kinematics measured from motion capture studies to elucidate neural coordination and/or structural features of the leg during walking. Neural coordination has typically been studied through large scale models [3, 39] that replicate the anatomy of the leg as fully as possible. These models include upwards of fifty leg muscles and dynamically optimize to infer muscle activations. While sophisticated they typically significantly overestimate the metabolic cost of walking (by 47% in [3]), likely because they do not carefully model neural-structural interactions. They use stock values for the parameters governing tendon function, failing to capture variation among subjects. These models also do not thoroughly address the issue of redundancy in joint actuation; for a given movement there are many different combinations of muscle function which could produce the same joint torque.

Another inverse modeling approach is to infer muscle-tendon structure through mechanical approximations to muscle function. Endo et al [19] built a model that uses clutch-spring units in place of most of the major muscles of the leg. This amounts to the assumption that muscles operate isometrically when activated, which is known to

be energetically efficient [53]. While simple, the Endo model is able to reproduce the kinetics and energetics of human walking. However it cannot be used to explore the interaction of neural and structural elements as both are included in the clutch-spring units.

Krishnaswamy et al [35] have successfully explored the interaction in question for the human ankle during walking. They use EMG data to estimate muscle activation and a kinematically clamped optimization procedure to infer the muscle-tendon morphologies of the muscles spanning the ankle. Their results suggest that proper scaling of the parameters governing tendon function is essential for inferring muscle force, state, and metabolic consumption. In this thesis we refine the method of [35] and extend it to the full leg.

1.1.2 Forward Modeling

Forward dynamic models of locomotion assume neural control schemes in order to produce walking given a set of initial kinematic conditions. One such model is the reflex walker of Geyer and Herr [21], which relies on physiologically-motivated guesses of linear reflex loops. While neural control is known to include both feedforward and feedback components, this model is able to produce stable, terrain adaptive walking using only feedback. An extension of the model [47] produces speed adaptive behavior by tuning reflexive control parameters. While intriguing, these models are hard to verify against ground truth as their hypothesized neural pathways are difficult to validate. They also use stock parameters to describe tendon force-length characteristics, implying that they would benefit from a means to scale to individual subjects.

1.1.3 Application to Prosthesis Control

Recently forward dynamic, reflex-based neuromuscular models have been applied in the control of robotic limbs [17]. Feedback-based control schemes lend themselves naturally to prosthesis control as they rely only on inputs that may be derived from the on-board sensors of the device. In [17], Eilenberg et al used a simplified version

of the model in [21] to control a robotic ankle-foot prosthesis. They observed terrain adaptive behavior, supporting the idea that controllers based on neuromuscular models can produce biomimetic behavior in robotic limbs.

1.2 Research Objectives

This thesis addresses both scientific and technical objectives. On the scientific side we employ a data-driven approach to estimate the force and state of individual muscles during walking. This is accomplished through the combination of two methods; a hidden state estimation of muscle activation and a system identification of optimal muscle-tendon morphologies. The latter procedure is based upon the hypothesis that the muscle-tendon morphology of the human leg has evolved to minimize the metabolic cost of walking at self-selected speed.

Once a realistic muscle-tendon morphology has been obtained, it may be paired with a reflex-based neural control scheme to produce a forward dynamic model. Such a model may be applied in the control of robotic limbs, and here we apply it to a robotic ankle-foot prosthesis. We evaluate the performance of the control scheme across speed, looking for adaptive behavior.

1.3 Thesis Outline

In Chapter 2 we provide the biomechanical and physiological background information necessary to place this thesis in context. We outline the gross mechanics of human walking, describe the biophysical processes that lead to muscle force generation, and discuss the interactions among neural control, muscle contraction, and muscle-tendon structure. We finish with a more precise statement of the problems to be addressed by this thesis.

In Chapter 3 we present the optimization procedure used to estimate the optimal muscle-tendon morphology of the leg. We discuss data collection and processing techniques, estimation of muscle activation, identification of optimal muscle-tendon

parameter sets, results, and implications of the model.

In Chapter 4 we present a pilot application of our modeling techniques to hardware control, in this case a powered ankle-foot prosthesis. We demonstrate the potential of reflex-based control schemes by observing speed adaptive walking behavior in clinical trials with a bilateral transtibial amputee.

Finally, we discuss the results from a global perspective and address current and future work in Chapter 5.

Chapter 2

Background

Studies of human locomotion apply concepts from several different fields. In this chapter we review the components that are critical to this thesis- the biomechanics of walking, the biophysics of muscle force generation, and the interaction between neural control and muscle-tendon structure. We conclude with a more precise statement of the problems to be addressed by this work.

2.1 Human Walking

The following is a brief introduction to the biomechanics and energetics of human walking. For a more thorough treatment see [42].

2.1.1 Gait Cycle

Human walking is a cyclic motion with a period known as the gait cycle. The gait cycle is defined as the time between consecutive heel strikes (or initial ground contacts) of the same foot. We refer to the time when the relevant foot is on the ground as "stance" phase and the time when that foot is in the air as "swing" phase. In walking stance phase lasts for more than half the gait cycle (about 60% at self-selected speed), leading to a double support phase in late stance. Further divisions of the gait cycle and their functionality are discussed in [42] and are shown in Figure 2-1.

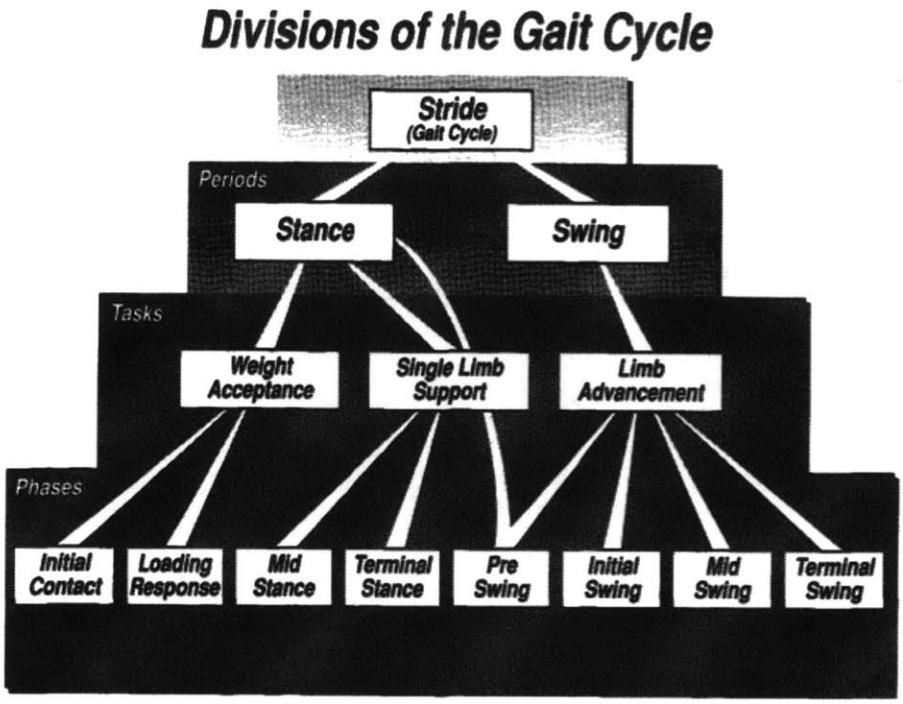

Figure 2-1: Phases of the gait cycle. Figure is reproduced from [42].

2.1.2 Energetics

Energy consumption during walking comes from the need to move the body forward in a gravitational field. To accomplish this, work must be done on the skeleton by the muscles, which requires metabolic energy. The amount of metabolic energy needed has a quadratic dependence with speed, monotonically increasing from slow walking speeds to fast[3]. The metabolic cost of transport (MCOT) is defined as this energy divided by the distance travelled divided by body weight and forms a concave-up parabola with walking speed. The speed at which the minimum occurs is typically in the range of 1.2 m/s to 1.6 m/s and is very close to the subject's self-selected walking speed, leading researchers to believe that human gait is tuned to minimize MCOT.

2.2 Muscles of the Leg

There are more than fifty muscles used to actuate the legs of the human body [3]. Of these muscles we are primarily interested in those that move the leg in the sagittal (front-back) plane, and specifically those that provide significant torque contributions normal to this plane during walking. Some of these muscles span only one joint (i.e. the soleus actuates only the ankle) while others span two joints (i.e. the hamstrings actuate the knee and the hip). The former group of muscles is referred to as monoarticular while the latter is called biarticular.

Representative drawings of the major muscles of the leg are displayed in Figure 2-2. At the ankle we evaluate the soleus (SOL), gastrocnemius (GAS), and the tibialis anterior (TA) muscles. The first two of these are on the posterior (back) of the leg, are joined by the Achilles tendon, and serve to extend the ankle.[1] The soleus spans only the ankle, while the biarticular gastrocnemius actuates both the knee and the ankle. The tibialis anterior is a smaller muscle and is located on the anterior (front) of the shin, serving to flex the ankle.

At the knee we once again include the effects of the gastrocnemius as well as two monoarticular and two other biarticular muscles. The monoarticular knee extensors are comprised of the powerful vastii (VAS) group, while the monoarticular knee flexor is the much weaker biceps femoris short head (BFSH). Two other biarticular muscles span both the knee and the hip; on the anterior side there is the rectus femoris (RF; an extensor) while on the posterior side there is the hamstring (HAM) group. The hamstrings are comprised primarily of the semimembranosus (SMEM), biceps femoris long head (BFLH), and semitendinosus (STEN) muscles which together play a large role in actuating both the knee and the hip.

At the hip, the rectus femoris serves as a source of flexion torque while the hamstrings provide extension torque. In addition to these the hip is actuated by several monoarticular muscles. Since the hip requires fuller three dimensional actuation than the knee and ankle, many of its muscles act in more than one plane. Promoting

[1] At the ankle, extension is often referred to as plantarflexion and flexion is referred to as dorsiflexion.

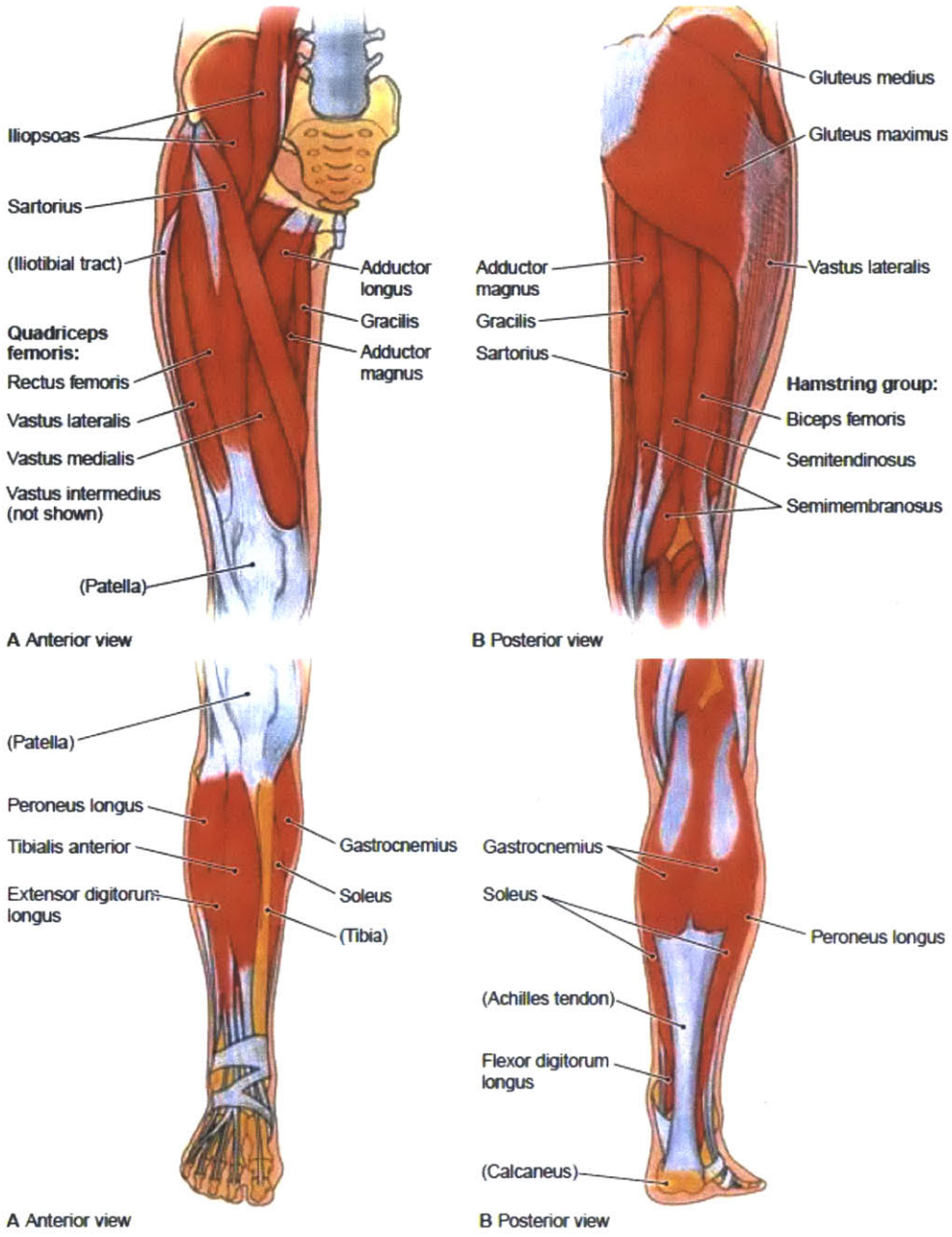

Figure 2-2: Major muscles and tendons of the leg. Source: http://encyclopedia.lubopitko-bg.com

movement primarily in the sagittal plane are the flexors (illiacus (ILL), psoas (PSO)) and extensors (lower gluteus maximus (GMAX)). Causing movement primarily in the coronal (left-right) plane but also providing significant torque normal to the sagittal plane are the upper gluteus maximus, gluteus medius (GMED), adductor magnus (ADDM), and adductor longus (ADDL). The upper gluteus maximus and gluteus medius primarily move the leg outward, or abduct the hip. Conversely the adductors move the hip in toward the center of the body. During walking the hip abductors and the adductor magnus provide extension torque normal to the sagittal plane while the adductor longus provides flexion torque.

2.3 Muscle Physiology

In this section we briefly describe the structure of muscles and mechanisms by which they generate force.

2.3.1 Structure

Muscles are the biological motors that actuate the skeleton, enabling motion. They are tension actuators connected to bones by tendons, which are nonlinear elastic structures. The muscle-tendon unit has a net length and velocity that is determined by the orientation of the joints they span and thus may be inferred from motion capture data. More information is needed to determine the individual lengths of the muscle and tendon.

Muscles themselves are comprised of several well-defined sub-units. Going from large to small these divisions are muscles, fascicles, fiber bundles, fibers (i.e. cells), myofibrils, myosin, and actin filaments. The actin (thin filaments) and myosin (thick filaments) are arranged in a hexagonal manner.

2.3.2 Contraction Dynamics

Muscle contraction dynamics are controlled by the nervous system through action potential trains delivered to the alpha motor neuron. These action potentials are conveyed to the neuromuscular junction through the axon of the alpha motor neuron via activation of voltage-gated sodium channels. The arrival of the pulse train at the neuromuscular junction prompts an influx of Ca^{2+} ions through voltage-gated calcium channels. The incoming Ca^{2+} ions cause the plasma membrane to release acetylcholine into the extracellular space, which in turn activates nicotinic acetylcholine receptors on the neuromuscular junction. This activation opens the intrinsic sodium/potassium channels of the junction, allowing sodium to rush into the muscle cell and potassium to filter out.

This flow of ions results in an action potential which propagates through the cell via transverse tubules, depolarizing the interior of the muscle fiber. The depolarization wave affects the membranes of the sarcoplasmic reticula, causing them to release calcium ions into the interior of the cell. This calcium binds to the troponin C of the thin filaments, allowing the troponin to allosterically modulate the tropomyosin. In resting muscle the tropomyosin sterically blocks myosin binding sites on the actin filament, but this modulation allows the tropomyosin to move and thereby allow access to the actin filament. Myosin then binds to these sites (in the "strong" state), forming cross bridges and releasing energy stored by the myosin. The myosin subsequently relaxes, rotating its globular head while releasing ADP and inorganic phosphate. This allows the filaments to slide past each other longitudinally and the muscles to contract. ATP then binds to the myosin, causing actin to be released and the myosin to be in the "weak" binding state. The ATP is subsequently hydrolyzed by the myosin, moving back to the "cocked back" formation seen at the start of cross bridge formation. The process then repeats as long as ATP and calcium are present near the thin filament. For a visualization of this sliding filament process see Figure 2-3.

Once the action potentials stop firing, the Ca^{2+} ions leave the troponin molecules and are taken back into the sarcoplasmic reticulum. The tropomyosin reverts to its

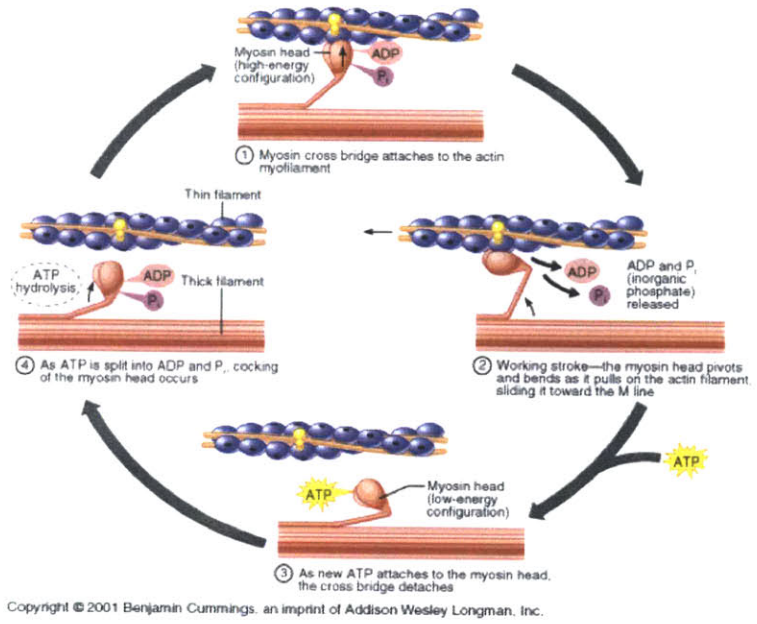

Figure 2-3: Illustration of the sliding filament theory of muscle contraction. Image credit: Benjamin Cummings, Addison Wesley Longman, Inc.

resting state and the binding sites on the actin once again become blocked, halting muscle contraction.

2.3.3 Muscle Force Generation Models

Models of the contraction dynamics specified above take many forms, depending on the goals of the problem at hand. Famous isotonic release and thermodynamic experiments by A.V. Hill [25] and others have indicated that muscle force generation may be modeled in terms of a neural command, the muscle length, and the muscle velocity. The origins and specific definitions of these three inputs are as follows:

Activation: Muscle activation reflects the neural input to a muscle, which can modulate contraction through the release of calcium ions from the sarcoplasmic reticulum. It is defined as the relative amount of calcium bound to troponin in a muscle, and therefore is a quantity averaged over many muscle fibers. As defined it ranges from 0 to 1, with higher values indicating more potential for cross bridge formation and higher muscle forces.

Length: The length of a muscle affects its output force due to the sliding of filaments discussed above as well as the passive elasticity of the muscle fibers. The result of the former is bell-shaped active force-length relation (stemming from the formation of cross bridges) which scales with activation. The result of the latter is a quadratic increase with length, independent of activation.

Velocity: The velocity dependence of muscle force stems from the finite amount of time that cross bridges take to form; if the filaments contract too rapidly fewer cross bridges will form and less force will be generated. On a macro scale this resembles a muscle "viscosity," with the muscle output force decreasing as the fiber shortens more rapidly.

The effects of these three inputs are known to be multiplicative and nearly separable [56], with the contractile element force F_{CE} being given by

$$F_{CE}(t) = \alpha(t) f_l(l_{CE}(t)) f_v(v_{CE}(t)). \tag{2.1}$$

Here α is activation, $f_l(l_{CE}(t))$ is the active force-length relation, and $f_v(v_{CE}(t))$ is the force-velocity relation. The passive aspect of the force-length relation is known as the parallel elasticity and it provides an additional contribution F_{PE}, with the total muscle force then being

$$F_m(t) = F_{CE}(t) + F_{PE}(t). \tag{2.2}$$

It should be noted that more sophisticated muscle models exist that do not assume the separability of the activation, force, and velocity terms. However, as was the case with this study, the small performance gains that may be derived from these models often do not justify their additional complexity.

2.4 Tendon Physiology

As mentioned above, tendons are elastic structures that connect muscle to bone. They act in series to the muscle actuators and are connected at oblique angles known as

pennation angles. They are passive and are composed of parallel arrays of collagen fibers, with a dense regular piece of connective tissue encased in a dense irregular outer sheath. Tendons come in various shapes and sizes, depending on function. The largest and strongest tendon in the body is the Achilles, which connects the soleus and gastrocnemius to the base of the foot.

The force-length curve of tendons is non-linear and can be modeled as an offset exponential. Its slope (the tangent modulus of elasticity) increases for low strains (in the so-called "toe" region) and remains approximately constant for high strains. The curve can be fit using four parameters- a slack length, a reference strain, a shape factor, and an overall scaling factor. These parameters are further discussed in Section 3.1.4. While most models (including ours) assume tendon action to be lossless, it should be noted that studies of animal tendons show losses of $6\% - 11\%$ of stored energy due to viscous effects while shortening at physiological rates [60, 56].

As the intermediary between force sources (muscles) and load (the skeleton), tendons play a large role in movement. They determine the impedance seen by the muscles while modulating the force seen by the load.

2.5 Neural-Structural Interactions

The interactions of the neural controller, muscle actuator, and skeletal "plant" are summarized in Figure 2-4. The nervous system controls the driving signal seen by the muscles. The muscles then act through the tendons to actuate the skeleton and negotiate the environment as desired. The properties/morphologies of the tendon are critical, as they determine the muscle lengths and velocities required to produce the desired output behavior. Tendons allow muscles to both operate with high metabolic efficiency [2] and to regulate their force and state, which are then communicated to the neural controller via reflexive feedback. This interplay may be understood through the lens of muscle impedance modulation. The nervous system conveys "intent" to

[2]Muscle metabolic consumption is largely a function of muscle velocity, as will be discussed in Chapter 3.

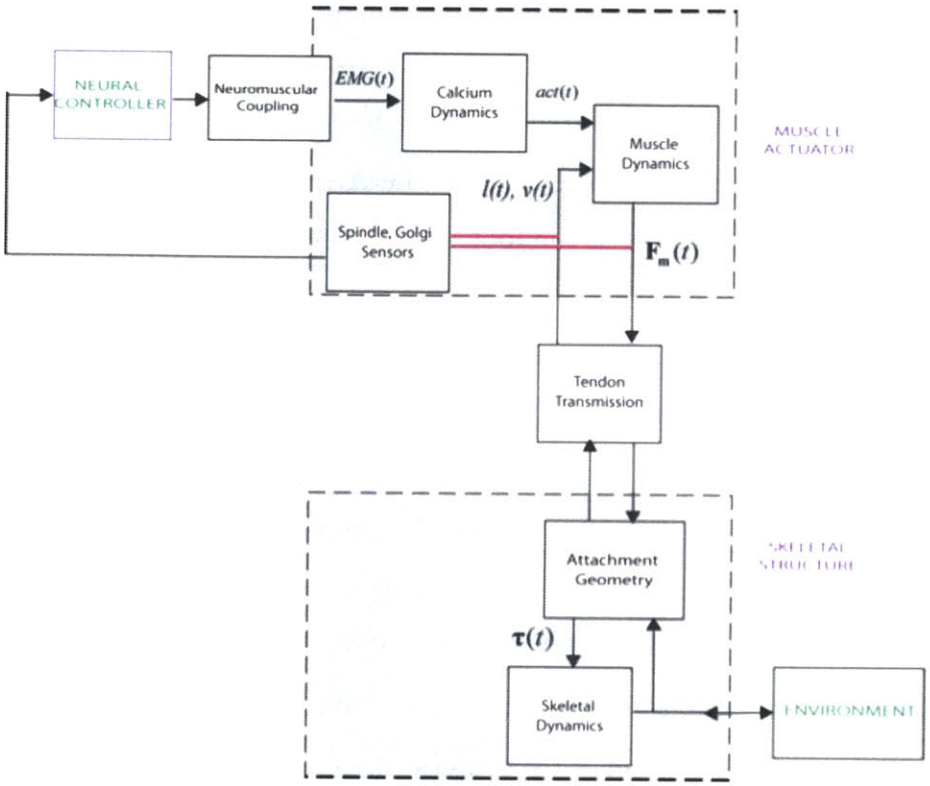

Figure 2-4: Flow chart describing neural-structural interactions. Artwork from Cajigas 2009 via Krishnaswamy 2010.

the muscles while the tendons produce a "feel" for the environment. The intermediary between the two is muscle impedance, which may be evaluated by studying muscle force and state.

2.6 Neural Control and the Role of Reflexes

Human motor control is believed to be composed of both a feedforward neural drive and a reflexive feedback component [33],[55]. As shown in Figure 2-4, reflexes dynamically link muscle force and state to muscle activation. While it is not known what proportion of the neural signal comes from the feedforward signal and how much comes from the feedback signal, models controlled with only local reflexive feedback loops have been shown to produce walking simulations that qualitatively agree with

human gait dynamics and muscle activations [21].

Having a neuromuscular model driven by only feedback would be useful for controlling robotic prosthetic limbs. In this application there is no feedforward driving signal, but the joint state of the prosthesis may be sensed and fed back to the controller. The joint state can be mapped to muscle-tendon length, which, when combined with a reflex structure, can be used to drive a muscle model. The output forces of the muscle model would then be mapped to desired torque of the device, allowing the loop to be closed. Eilenberg et al [17] observed terrain adaptive behavior when applying this method to control a robotic ankle foot prosthesis.

2.7 Problem Statement

This background information provides context for a more precise formulation of our objectives. We seek to build a data-driven model of walking that enables determination of the force and state of each modeled muscle throughout the gait cycle. Doing so would allow us to resolve the contributions of each muscle to joint torque, solving the redundancy problem and providing a basis to investigate neural control strategies. Mathematically we have, at each joint:

$$\tau(t) = \sum_i F_i(t) r_i(t) \tag{2.3}$$

$$l_{MTC,i}(t) = l_{t,i}(t) + l_{m,i}(t)\cos(\theta_i(t)) \tag{2.4}$$

$$F_i(t) = F_{t,i}(t) = F_{m,i}(t)\cos(\theta_i(t)) \tag{2.5}$$

$$F_{m,i}(t) \propto \alpha_i(t) f_l(l_{CE,i}(t)) f_v(v_{CE,i}(t)) + F_{PE}(l_{CE,i}(t)) \tag{2.6}$$

$$F_{t,i}(t) = f_{t,i}(l_{t,i}, \vec{m}_i) \tag{2.7}$$

Assuming that the muscle-tendon lengths $l_{mtc,i}$ can be estimated from geometry, the remaining unknowns are the muscle activations $\alpha_i(t)$, muscle states $l_{CE,i}(t)$, and muscle-tendon morphologies $\vec{m}_i$. In this inverse approach we estimate the hidden

state $\alpha_i(t)$ using EMG data. We then hypothesize that the human body has evolved to minimize the metabolic cost of walking at self-selected speed. We apply this hypothesis to determine the unknown muscle-tendon morphologies $\vec{m}_i$ and muscle states $l_{CE,i}(t)$, evaluating the results against empirical studies. The methods and results of this inverse optimization problem are presented in the next chapter.

Once this inverse problem is solved, the results may be applied in the control of robotic limbs. In Chapter 4 we discuss how an optimal reflex structure was wrapped around this model and used to control a powered ankle-foot prosthesis.

Chapter 3

Muscle-Tendon Morphology Optimization

As previously described, neuromuscular walking models may be improved by placing a greater emphasis on the role of compliance. Here we describe a method for obtaining more accurate metabolic cost and muscle state estimates by determining the muscle-tendon morphology for an individual human. To achieve this we first collected kinematic, kinetic, electromyographic, and metabolic data from five subjects. The kinematic data were used to estimate muscle-tendon states and moment arms, the kinetic data were used to estimate joint moments, and the EMG data were used to estimate muscle activation. We performed a kinematically-clamped, multi-objective optimization of the parameters that govern the force-length curve of each tendon, searching for parameter sets that simultaneously matched the collected kinetic data and minimized metabolic cost. In the following sections the specifics of this method as well as its results are discussed.

Subject	Age	Mass	Leg Length	Ethnicity	Sport	Min. MCOT
DH	24	80.3 kg	0.953 m	African	Basketball	1.32 m/s
MC	24	72.3 kg	0.927 m	Caucasian	Running	1.49 m/s
JB	29	68.9 kg	0.933 m	Caucasian	Running	1.31 m/s
BC	26	65.0 kg	0.902 m	Caucasian	Running	1.38 m/s
DC	25	65.4 kg	1.028 m	Caucasian	Running	1.47 m/s

Table 3.1: Relevant characteristics of study participants.

3.1 Methods

3.1.1 Data Collection

Kinematic, kinetic, electromyographic, and metabolic data were collected from five adult males in a study approved by the MIT Committee on the Use of Human Subjects and conducted at the Harvard University Skeletal Biology Lab. The heights, weights, ethnicities, and favorite sports of the study participants are listed in Table 3-1. All subjects were male and of at least moderate athletic ability, with the runners all being at a semi-professional level. This group was chosen because EMG signals recorded from participants with athletic backgrounds are typically cleaner than those obtained from sedentary individuals. All subjects were pre-screened to avoid gait pathologies and current injuries. Further details on each data modality are as follows:

Metabolic Data The required data sets were collected in two phases. After informed consent was obtained, the subjects were first outfitted with a portable oxygen consumption mask attached to a Cosmed $K4B^2$ VO_2 system. This system employs a standard open-circuit gas analysis technique to estimate metabolic energy consumption based on measurements of oxygen inhaled and exhaled [7]. The subjects[1] were then asked to stand still for seven minutes while a basal measurement was recorded. They then walked barefoot on an instrumented treadmill for seven minutes at each of six speeds (0.75 m/s, 1.00 m/s, 1.25 m/s, 1.50 m/s, 1.75 m/s, and 2.00 m/s), allowing the variation of metabolic energy expenditure to be measured across speed. These results were

[1]Basal trials were recorded for BC, DC, and JB.

quickly tabulated and used to estimate the walking speed where the metabolic cost of transport (MCOT) was minimal (Table 1).

Once the metabolic cost measurements were completed, the oxygen consumption mask and Cosmed system were removed and the participants were outfitted for the second phase. In this second phase kinematic, kinetic, and electromyographic data were collected for two minutes of barefoot walking at each of seven speeds; the six listed above and the speed where the subject's MCOT was found to be minimal. The methods for collecting these three data types were the following:

Kinematic Data An infrared camera system (8 cameras, Qualisys Motion Capture Systems, Gothenburg, Sweden) was used to track the motion of subjects as they walked in the capture volume. Reflective markers were placed at 43 (bilateral) locations on the participant's body and their three dimensional trajectories were recorded at 500 Hz. The marker locations were chosen specifically to track joint motion, as prescribed by the Helen Hayes marker model.

Kinetic Data An instrumented force plate treadmill (Bertec Corporation, Columbus, OH) was used to measure the ground reaction forces of the subjects as they walked. Foot contact centers of pressure were also recorded. The treadmill had two side-by-side belts, ensuring that each foot would be measured separately. The sampling rate for these observations was 1000 Hz.

Electromyographic Data A surface EMG system (Motion Lab Systems, Baton Rouge, LA) was used to record activity in fourteen muscles of one leg of each subject (tibialis anterior, soleus, medial gastrocnemius, vastus lateralis, biceps femoris shorthead, rectus femoris, semimembranosus, biceps femoris long head, illiacus, gluteus maximus (lower), gluteus maximus (upper), gluteus medius, adductor longus, and adductor magnus). Symmetry was assumed for the other leg, and all channels were sampled at 1000 Hz. The signals were recorded at the surface using pre-gelled bipolar electrodes (Electrode Store Model BS-24SAF, part number DDN-20) and amplified 20 times by pre-amplifiers (Motion Lab

Systems, part number MA-411). Prior to walking trials a maximum voluntary contraction (MVC) trial was conducted for each muscle group wherein the participant was asked to work that particular group as hard as possible. These trials were used for normalization purposes in muscle activation estimates.

The second phase was conducted separately from the first for practical reasons; with long trials markers would occasionally become dislodged and the EMG surface connections eventually degraded.

3.1.2 Data Processing Procedures

The following steps were taken to produce the required model inputs and output references.

Metabolic Cost Estimation

The metabolic data were used as both (i) a means to find the walking speed where the MCOT was minimal and (ii) a way to estimate the metabolic cost of walking across speed. As mentioned previously, we hypothesize that the human body has evolved to maximize the metabolic efficiency of walking at a preferred speed, and this "self-selected" speed is taken to be where the MCOT is minimal. Hence the metabolic data determine the speed where the model should be trained while providing target metabolic consumption values for the model to replicate at all recorded speeds.

As mentioned above, our system uses a standard open-circuit gas analysis technique to estimate metabolic energy consumption based on measurements of oxygen inhaled and carbon dioxide exhaled [7]. Specifically, the formula for metabolic energy expenditure in kJ is

$$\text{Metabolic Energy Expenditure} = 20.964 V \Delta O_2, \tag{3.1}$$

where V is the ventilation rate (pulmonary or exhaust) and ΔO_2 is the oxygen concentration difference in the inspired and expired air. This equation is known to have an accuracy of $\pm 3\%$. The metabolic cost of transport (MCOT) is then defined as

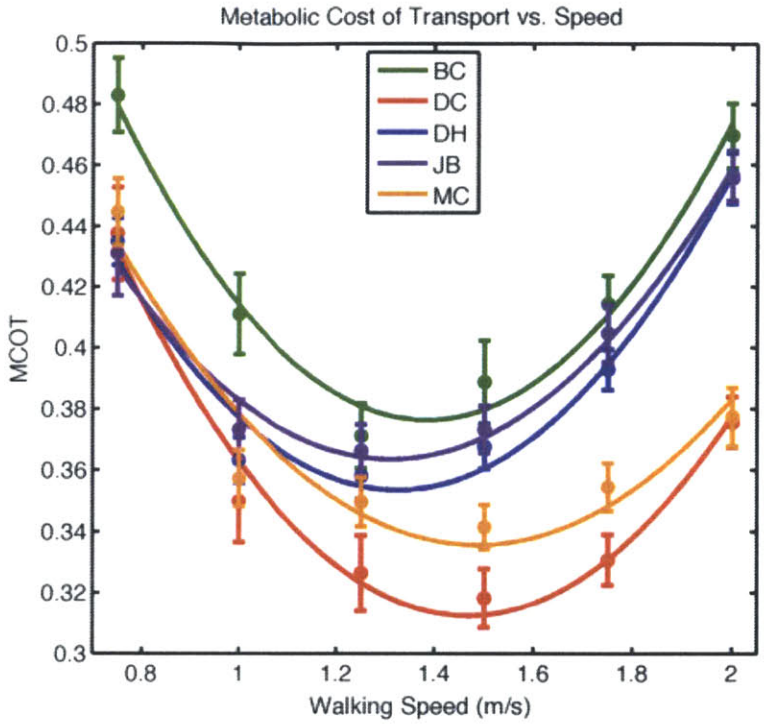

Figure 3-1: Metabolic cost of transport is plotted vs. walking speed for each participant.

$$\text{MCOT} = \frac{\text{Metabolic Energy Expenditure}}{\text{Distance Travelled} \times \text{Body Weight}} \tag{3.2}$$

and typically has a minimum value of about 0.35, which occurs at a walking speed in the range of 1.2 m/s - 1.6 m/s. To determine the walking speed where MCOT was minimal for our participants we used a quadratic fit of the MCOT vs. speed plot, as shown in Figure 3-1. The resulting speeds for each subject are shown in Table 3-1.

Joint States and Moments

To formulate our inverse optimization problem we require joint angle and moment trajectories. These quantities describe motion on a macro scale and may be estimated using the collected motion capture and force plate data. The motion capture data sets are comprised of tracked marker trajectories in 3D space, each representing an anatomical landmark. The force plate data sets include ground reaction force (GRF) vectors and the location of the center of pressure (COP) of each GRF.

After collection, the motion capture trajectories are labelled and have their gaps filled via a spline-based interpolation algorithm in the Qualisys Track Manager (QTM, Qualisys Motion Capture Systems, Gothenburg, Sweden) software. The raw force plate data are processed and low pass filtered with a cutoff of 50 Hz in MATLAB (Mathworks, Natick, MA). The two data sets are synced and exported to SIMM (Software for Musculoskeletal Modeling, Musculographics Inc., Evanston, IL).

The SIMM software was chosen for this analysis because of its unparalleled anatomical accuracy. It provides reasonable, subject-specific representations of body segments, joints, and muscle-tendon units. It also allows the user to access subject-specific parameter scalings, which proved critical for our analysis. SIMM is based on a model of an "average" human body that was formulated through cadaver studies and may be scaled and tweaked for any individual. The scaling is obtained through an inverse kinematic fit to a static trial and is applied in determining the kinematics for each subsequent walking trial. The kinematic output is combined with the force plate data to compute joint torque profiles via inverse dynamics. This step is performed by the SIMM Dynamics Pipeline using the SDFAST (PTC, Needham, MA) software.

Several post-processing steps were performed to produce the average torque profiles that were used in the ensuing analysis. First the data sets were broken into gait cycles as determined by the force plate data. Gross outlier gait cycles were discarded and the remaining time series were normalized in time to percent gait cycle and averaged. Plots of typical angle and torque profiles and their variation across speed are shown in Figures 3-1 and 3-2. Note that while SIMM produces a full 3D body representation, only motion in the sagittal (front-back) plane was considered for this model.

Muscle-Tendon States and Moment Arms

To study force production by muscles, we must have a means to estimate muscle-tendon lengths and moment arms. These quantities are related to joint angles through complex musculoskeletal geometry, which is modeled in SIMM using wrap objects.

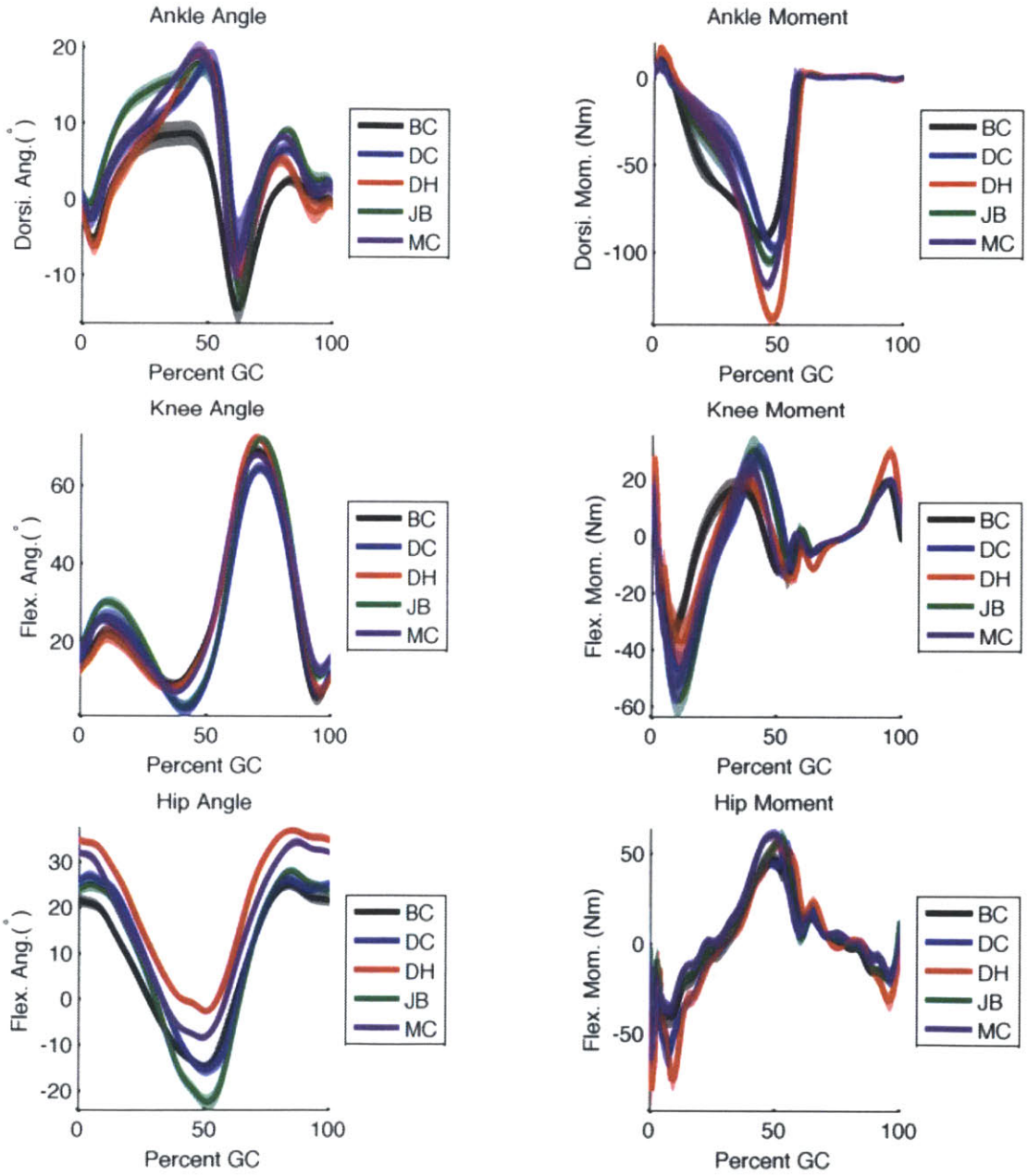

Figure 3-2: Ankle, knee, and hip angle and moment trajectories for all subjects walking at 1.25 m/s.

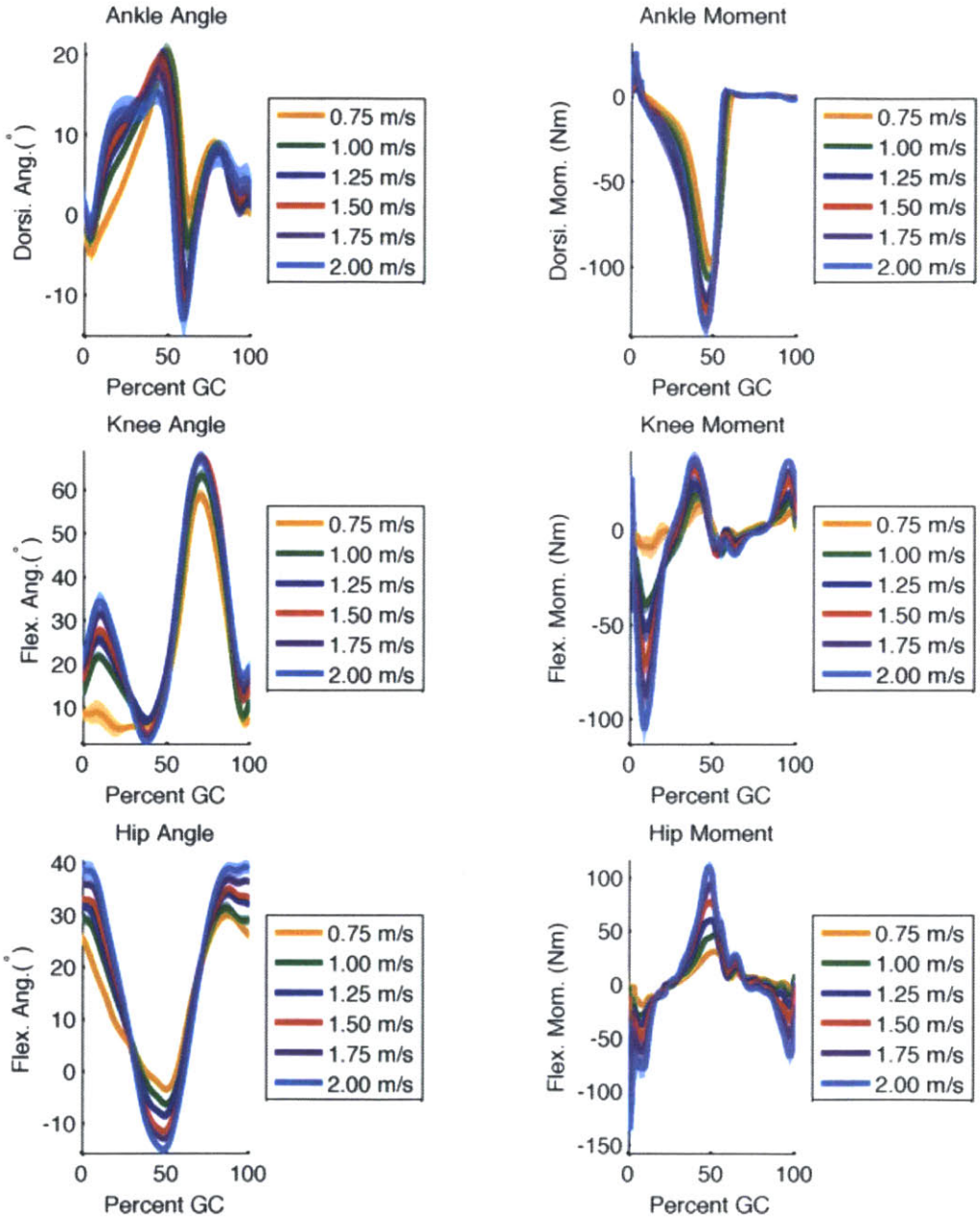

Figure 3-3: Variation of ankle, knee, and hip angle and moment trajectories for one subject across speed.

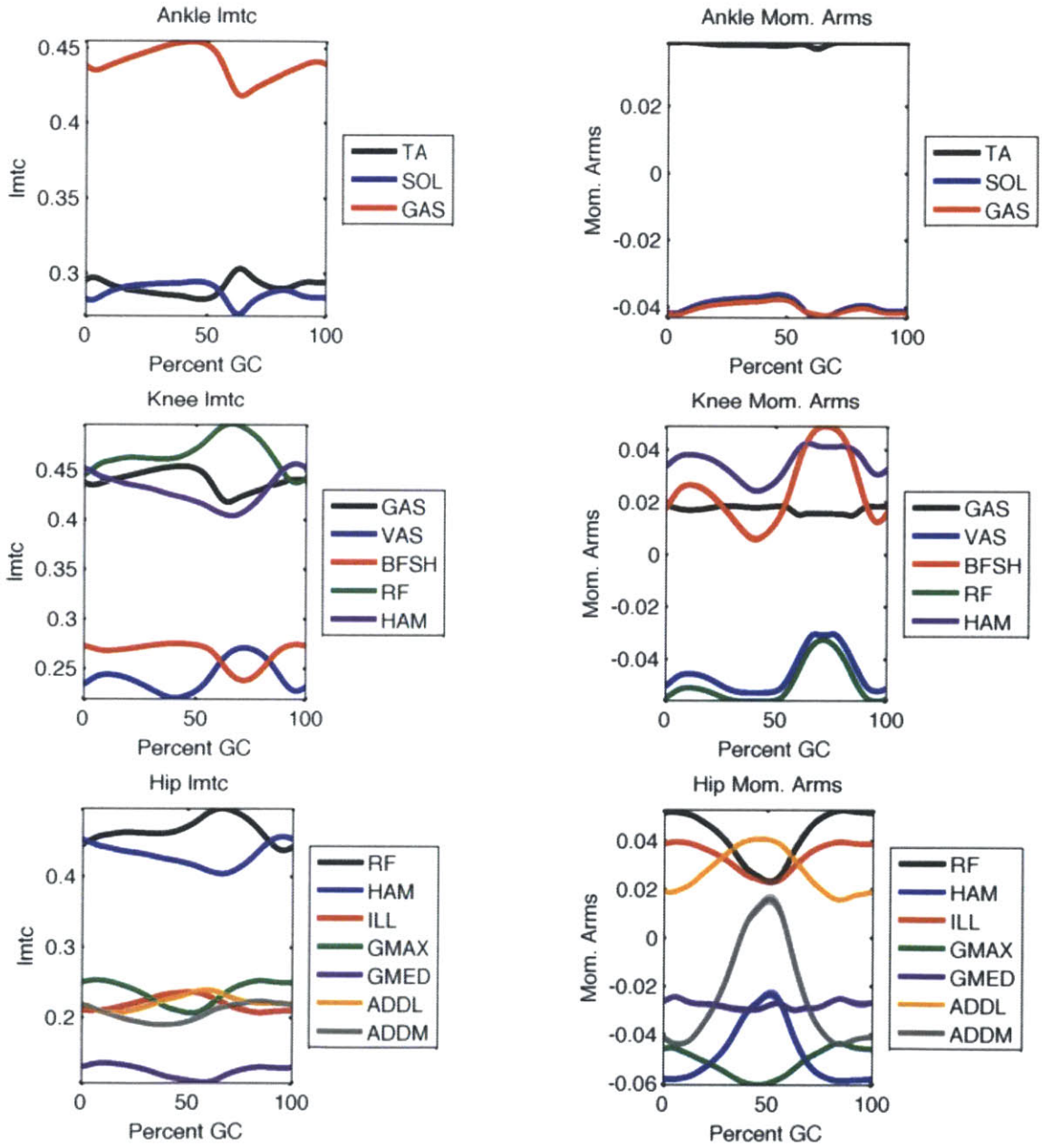

Figure 3-4: Muscle-tendon unit lengths and moment arms for one subject walking at 1.25 m/s.

The wrap objects are derived using information from cadaver studies and digitized bone surfaces[15]. The inputs to the applied method are joint angles and SIMM's subject-specific musculoskeletal scaling, which are then used to determine muscle-tendon lines of action and the quantities we seek.

To produce the profiles used as input to the model, we follow the same post-processing steps as were used with joint angles and moments. Specifically we break the time series into gait cycles, discard outliers [2], normalize to percent gait cycle, and average. Plots of typical muscle-tendon lengths and moment arms are shown in Figures 3-3 and 3-4.

3.1.3 Muscle Activation Estimation

The final required input for our inverse optimization problem is muscle activation, which represents the control signal from the nervous system to the muscles. This signal may be estimated using recordings from surface electromyography (EMG). Below we recap the biophysical processes involved in muscle activation, the information contained in EMG signals, and the mathematical methods employed in estimating muscle active state.

Biophysics of Muscle Activation

As described more fully in Section 2-3, muscle contraction is initiated by action potential trains delivered to the alpha motor neuron. The arrival of this neural signal starts a process that results in the release of calcium ions from the sarcoplasmic reticulum (SR). These calcium ions diffuse through the cell, binding to troponin and enabling cross bridge formation and thereby muscle contraction. Mathematically the release of calcium ions from the SR may be modeled as a rapid jump process, while the spread of calcium through the cell and its binding to troponin may be modeled as a slower diffusion process. Activation is defined as the relative amount of calcium bound to troponin in a muscle (averaged over all cells) and therefore gives a direct

[2]The outliers for muscle-tendon length and moment arm were assumed to be the same as those for joint angle/moment, as joint angle can be mapped to the former two quantities.

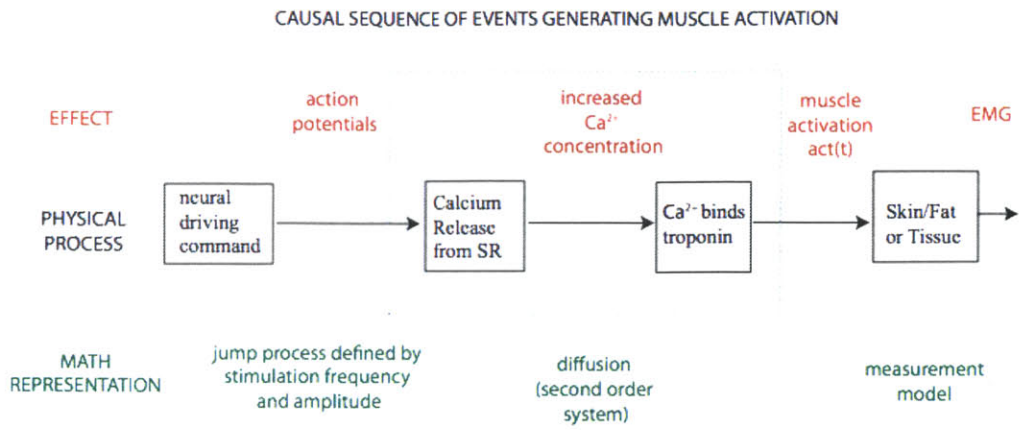

Figure 3-5: Biophysics of muscle activation. Figure credit: Krishnaswamy M.S. Thesis.

measure of the capability of the muscle to generate force in a given state. It may be estimated using surface EMG measurements, which record a net potential that reflects the action potentials, depolarization currents, and ion flows within the muscle. All of these processes are observed through the filter of skin and fat. The physiology, mathematical representation, and measurement information for the muscle activation process are summarized in Figure 3-5.

Neural Excitation Estimation

Many algorithms have been developed for estimating neural excitation from EMG signals. All such methods seek to determine the driving signal behind the modulated noise that is measured. The standard means to do this is to find an envelope for the signal through the use of a low pass filter. This maximal likelihood method was first investigated by Hogan [28, 29] and has since been slightly modified to account for artifacts in the data [10]. A Bayesian method developed by Sanger [45] has also seen wide-spread use recently. For this application we evaluated both methods, finding the main difference in performance to be the slightly later timing of the estimates from the Sanger method. We chose to use the Sanger method because its timing was more

aligned with the required muscle moment profiles. Below we describe the details of this Bayesian method; for further details on low pass implementation see [10].

The Sanger Bayesian method was developed to more accurately resolve sudden jumps in neural activity. It models the underlying driving signal as the result of a jump-diffusion process, namely

$$dx = \epsilon(dW) + (U - x)dN_\beta. \tag{3.3}$$

This equation is to be interpreted in the Ito sense, with x being the neural driving signal, dW being the differential of standard Brownian motion with rate α, dN_β being the differential of a counting process with β events occurring per unit time (the jump term), and U being a uniformly distributed random variable in $[0, 1]$. Without the driving dN_β term this equation would amount to a random walk. The boundary conditions are defined to keep $x(t)$ in the interval $[0, 1]$ and are given by

$$dx = \begin{cases} (1 - x)\delta(t - t_0), & \text{if } x(t_0) > 1 \\ (0 - x)\delta(t - t_0), & \text{if } x(t_0) < 0. \end{cases} \tag{3.4}$$

An approximate solution for the evolution of the probability density of x is the Fokker Planck Equation,

$$\frac{\partial p(x,t)}{\partial t} = \epsilon \frac{\partial^2 p(x,t)}{\partial x^2} + \beta \left[1 - p(x,t)\right]. \tag{3.5}$$

To evaluate this one must define a measurement model for the signal, and Sanger uses

$$P(\text{emg}|x) = \frac{\exp(-\text{emg}/x)}{x}. \tag{3.6}$$

Here $P(\text{emg}|x)$ is the conditional probability of observing rectified emg = |EMG| given driving signal x. This model reflects the observed Laplacian distribution of EMG signals and wraps all elements of the measurement- the various fibers and electrical sources, the filter of skin and fat, the placement and impedances of the

electrodes- into one equation. Combining this with Bayes' Rule

$$P[x(t)|\text{emg}(t)] = \frac{P[\text{emg}(t)|x(t)]P[x(t)]}{P[\text{emg}(t)]} \tag{3.7}$$

and approximating (3.5) using second differences one can solve for the maximum a posteriori (MAP) estimate of $x(t)$, i.e. find the $x(t)$ that maximizes $P[x(t)|\text{emg}(t), \text{emg}(t-1), ..]$.

While Sanger does not make any claims about the physiological relevance of the resulting driving signal $x(t)$, we may gain some insight by noting the similarities between his model and the biophysics of muscle excitation outlined above. The jump process can be mapped to the release of Ca^{2+} ions from the SR while the diffusion term may be mapped to the slower spread of calcium ions through the cell and their binding to troponin sites. Hence the driving signal $x(t)$ reflects the neural excitation and distribution of calcium ions during muscle contraction. However it does not take into account the delay caused by calcium-troponin binding dynamics, and since the jump rates are symmetric for both increasing and decreasing $x(t)$ it does not model the known disparity between activation and deactivation time constants [60]. Hence further filtering is required to adequately model muscle activation.

Activation Estimation

Neural excitation and the muscle active state are linked by a series of slow, second order events. These include the drift and diffusion of calcium ions as well as calcium-troponin binding dynamics. Activation buildup is initiated by the the release of calcium ions from the SR and terminated by those ions unbinding from the troponin and being re-absorbed by the SR. The process of activation is known to proceed with a faster time constant than that of deactivation [60, 53], with both numbers being a function of muscle composition (muscles with a higher fast twitch concentration have smaller time constants). While it would be ideal to incorporate all of this into a modified Sanger model (i.e. to allow for variable jump rates in Equation 3.3), a simpler approach is to apply a shaping filter to the estimated neural excitation. We

chose the latter approach and employed a relation derived by Raasch [51]:

$$\dot{\alpha} = \begin{cases} (u-\alpha)\left[u/\tau_{\text{act}} + (1-u)/\tau_{\text{deact}}\right], & u \geq \alpha \\ (u-\alpha)/\tau_{\text{deact}}, & u < \alpha. \end{cases} \tag{3.8}$$

Here u is the neural excitation, α is activation, and τ_{act} and τ_{deact} are the activation and deactivation time constants, respectively. The values of these time constants for each muscle are listed in Table 3-2. An example of the neural excitation and activation estimates for one subject's medial hamstring (semimembranosus) muscle is plotted in Figure 3-6. As described above, the Sanger estimate provides a slightly later excitation profile than the low pass filter [3] The activation estimates are delayed relative to and remain elevated longer than the excitation signals, as discussed above.

Implementation

The following steps were taken to implement the activation estimation algorithms described above:

Preprocessing: As in Sanger's work, the raw EMG data first had its mean removed and then was clipped at 5 standard deviations.[4] The signal was rectified and normalized to the value where it was clipped.

Excitation Estimate: The preprocessed data were evaluated using the Sanger algorithm discussed above. Two small errors in the algorithm were corrected in the published code and the ϵ and β constants were adjusted to 1/2 $(1000/Fs/2)$ and 5×10^{-31}, respectively, to allow the weaker signals to be captured. It was found that these parameter tunings increased the sensitivity of the algorithm while preserving its timing. Their downside was a slight loss of sharpness in the turn on/turn off of muscle excitations, but this would have been lost in the ensuing activation filter and averaging anyway. The resulting excitation estimates

[3]Some authors include a 40 ms delay when using low pass filters[4], likely to account for this timing discrepancy.

[4]Sanger used 3 standard deviations while Krishnaswamy [35] used 5 standard deviations.

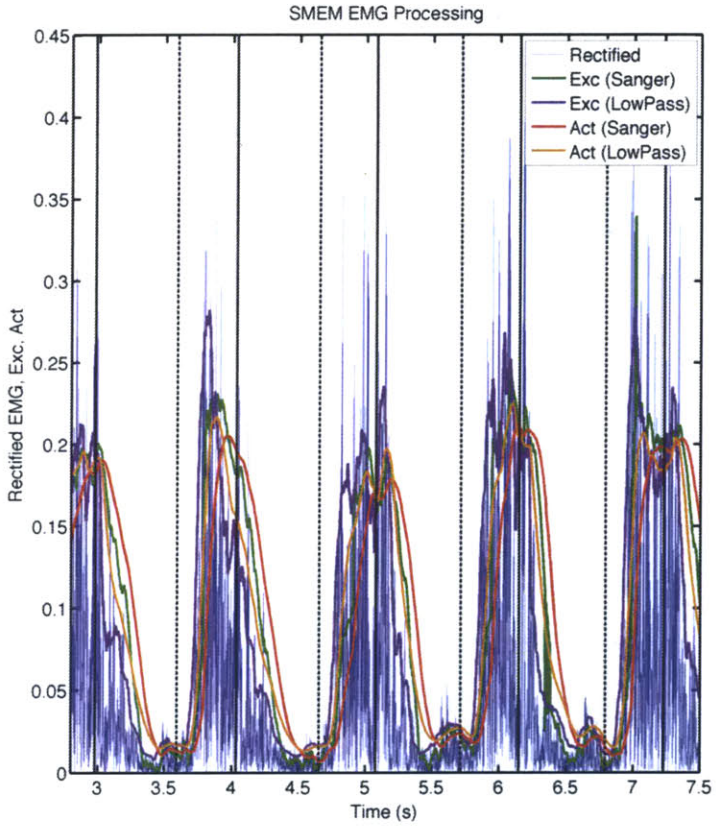

Figure 3-6: EMG processing of the semimembranosus (medial hamstring) muscle. The solid vertical lines are heel strikes of the observed leg while the dashed vertical lines are toe off events.

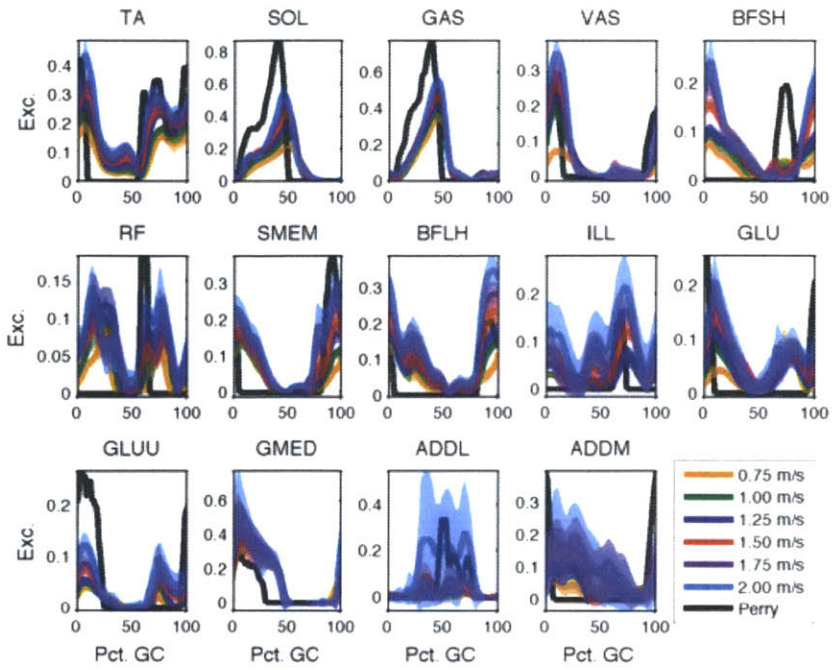

Figure 3-7: Mean neural excitation trajectories across speed for all subjects with reasonable profiles. The estimates were obtained via the Sanger Bayesian method and are compared to the literature values in Perry's *Gait Analysis* [42].

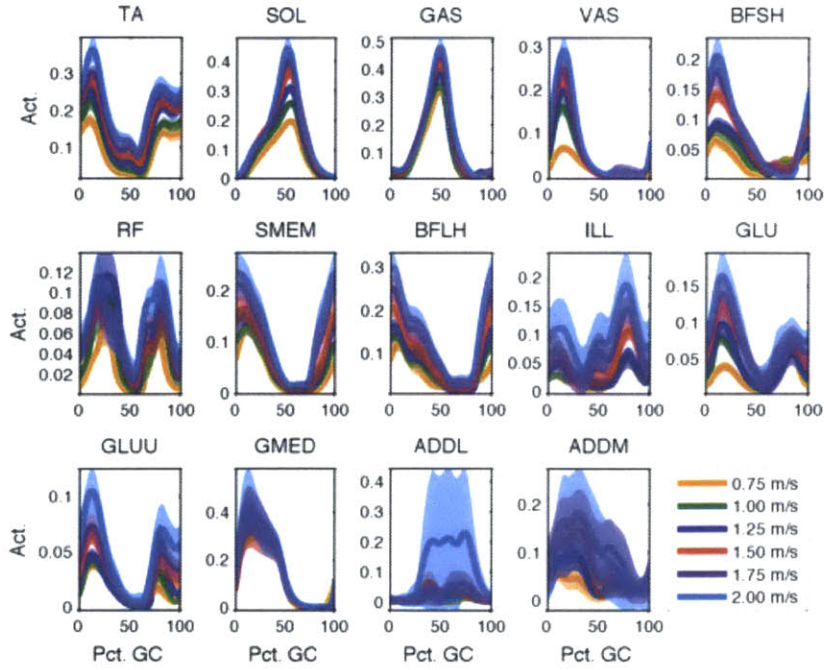

Figure 3-8: Mean activation trajectories across speed for all subjects with reasonable profiles. The estimates were obtained using the Sanger Bayesian method.

were then re-normalized by their values during maximal voluntary contraction (MVC) trials.

Thresholding The excitation estimates were thresholded by setting any measurement below a defined value to zero. This had the effect of removing the noise floor and making the surface EMG estimates more closely resemble the cleaner signals obtained through the use of fine wire EMG [42].

Activation Estimate: The excitation estimates were passed through the filter of Equation 3.8 to generate activation estimates.

Removal of Outliers, Averaging: The activation estimates were then broken into gait cycles (based on the synced force plate data) and obvious outliers were removed from the data sets. These outliers were caused by a large number of different factors- motion artifacts, faulty electrode connections, abnormal subject strides, etc. The results were then averaged over all gait cycles for each speed and subject.

Addressing Missing Data: Despite our best efforts, some data channels were obviously faulty. This problem typically occurred in measurements of muscles spanning the hip and was caused by the relatively complicated geometry of that joint, the preponderance of associated motion artifacts, the muscles being located deep beneath the skin, and the relative lack of access to that area. In the event that a channel was not salvageable for a given subject, the trajectory of that muscle was taken to be the average of the trajectories for that muscle in all subjects where the measurement was acceptable. Further details of this procedure are available in Appendix A. We found that we had sufficient data to model all desired muscles (Figure 3-9) except the adductor longus (ADDL) and adductor magnus (ADDM).

Plots of the average excitation and average activation profiles across walking speed for all subjects are shown in Figures 3-7 and 3-8.

3.1.4 Muscle-Tendon System Identification

Having estimated muscle-tendon lengths and muscle activations from the data, we may now turn to evaluating muscle force and state. As discussed in Section 2.7, knowledge of these quantities leaves the fascicle states $l_{CE,i}(t)$ and muscle-tendon morphologies $\vec{m}_i$ as the only remaining unknowns in the system. A choice of one implies the other, and we identify the muscle morphologies under the hypothesis that they have evolved to minimize the metabolic cost of walking at self-selected speed. In the following we describe an optimization procedure that uses this hypothesis to infer values for the morphological parameters $\vec{m}_i$ and thereby estimate muscle fascicle state.

System Model

Our system is defined to include all muscles that make significant contributions to the components of ankle, knee, and hip torque perpendicular to the sagittal plane during walking. These muscles are described in Section 2.2. Several muscle groups were lumped together for simplicity; this was deemed appropriate if all muscles within a group have similar lines of action and are activated concurrently during walking. The model is shown in Figure 3-9. For each muscle the net effect of all tendinous attachments are modeled as one elastic element in series with the muscle. In addition to the muscle-tendon units a passive ligament was included at the hip to prevent hip overextension around toe off. This element modeled the contributions of the iliofemoral ligament and was taken to be a simple rotary spring:

$$\tau_{HFL} = -K_{HFL}(\theta_{hip} - \theta_{0,HFL}). \tag{3.9}$$

Note that both the moment and the angle in this equation are defined with flexion being positive. The equations describing muscle, tendon, and joint level dynamics are given below.

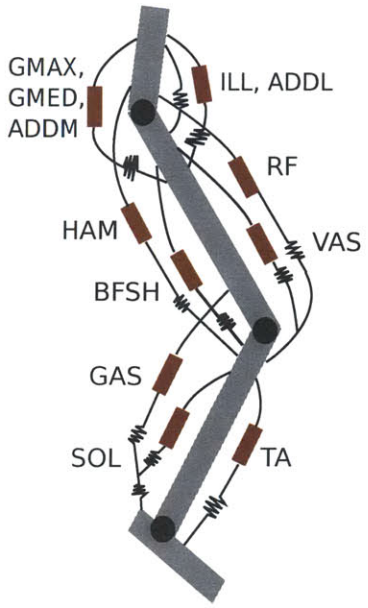

Figure 3-9: System model. Note that the soleus and gastrocnemius tendons were modeled separately in the final iteration

Muscle	Percent FT	τ_{act} [ms]	τ_{deact} [ms]	w	K	v_{max} [l_{opt}/s]	θ_0
TA	25%	68	76	0.49	6.60	6.0	5°
SOL	20%	71	79	0.80	6.24	6.4	25°
GAS	50%	57	62	0.61	8.40	4.0	17°
VAS	50%	57	62	0.55	8.40	4.0	5°
BFSH	35%	64	70	0.75	8.40	5.2	23°
RF	65%	49	65	0.76	9.48	2.8	5°
HAM	35%	64	70	0.75	7.32	5.2	15°
ILL	50%	57	62	0.74	8.40	4.0	7°
GMAX	45%	59	65	0.77	8.04	4.4	0°
GMED	50%	57	62	0.77	8.40	4.0	19°
ADDL	35%	64	70	0.74	7.32	5.2	6°
ADDM	45%	59	65	0.75	8.04	4.4	3°

Table 3.2: Muscle-specific model parameters. Muscle fiber compositions, w, τ_{act}, and τ_{deact} were taken from [52].

Muscle Dynamics The biophysics of muscle contraction and the models that are used to describe it are discussed in Section 2.3. Here we specify the Hill type muscle model used in this study, which is similar to the model in [21]. It contains a contractile element (CE) that represents the active muscle fibers and a parallel elasticity (PE) that represents the elastic structures surrounding the muscle. The force produced by the contractile element is

$$F_{CE} = \alpha F_{max} f_l(l_{CE}) f_v(v_{CE}), \tag{3.10}$$

where α is the muscle activation, l_{CE} is the contractile element length, $v_{CE} = \dot{l}_{CE}$ is the contractile element velocity, and F_{max} is its maximum isometric force. $f_l(l_{CE})$ and $f_v(v_{CE})$ are the active force-length and force-velocity relations and are given by

$$f_l(l_{CE}) = \frac{-1}{w^2}\left(\frac{l_{CE}}{l_{opt}}\right)^2 + \frac{2}{w^2}\left(\frac{l_{CE}}{l_{opt}}\right) - \frac{1}{w^2} + 1 \tag{3.11}$$

and

$$f_v(v_{CE}) = \begin{cases} \frac{v_{max}+v_{CE}}{v_{max}-Kv_{CE}}, & v_{CE} < 0 \\ N - \frac{(N-1)(v_{max}-v_{CE})}{7.56Kv_{CE}+v_{max}}, & v_{CE} \geq 0. \end{cases} \tag{3.12}$$

In (3.10) l_{opt} is the fascicle length where maximal active force is produced and w determines the width of the active force-length relation. In (3.11) v_{max} is the maximal muscle velocity, K is a curvature constant, and $N = 1.5$ is the muscle force (in units of F_{max}) at the muscle's maximum lengthening velocity. The active force-length relation (3.10) comes from [54] and was chosen because, while similar to the relation in [21], it allows scaling based on fiber composition. The parallel elasticity produces force according to

$$F_{PE}(l_{CE}) = \begin{cases} F_{max}\left(\frac{l_{CE}-l_{opt}}{l_{opt}w}\right)^2, & l_{CE} \geq l_{opt} \\ 0, & l_{CE} < l_{opt}. \end{cases} \tag{3.13}$$

Note that this quadratic elastic element is only engaged for $l_{CE} \geq l_{opt}$. Finally, we

include a buffer elasticity

$$F_{BE}(l_{CE}) = \begin{cases} F_{max}\frac{2}{w}\left(\frac{l_{CE}-l_{opt}(1-w)}{l_{opt}}\right)^2, & l_{CE} \leq l_{opt}(1-w) \\ 0 & l_{CE} > l_{opt}(1-w) \end{cases} \tag{3.14}$$

that prevents the muscle fascicle from shortening excessively. It is a rarely engaged numerical tool and does not reflect a physical characteristic of muscle. The total force produced by the muscle fascicle is then

$$F(\alpha, l_{CE}, v_{CE}) = F_{CE}(\alpha, l_{CE}, v_{CE}) + F_{PE}(l_{CE}) - F_{BE}(l_{CE}). \tag{3.15}$$

The inputs α, l_{CE}, and v_{CE} all vary with time.

Tendon Dynamics As described in Section 2.4, tendons are non-linear elastic elements that join muscle to bone. Their force-strain relation may be modeled as [56]:

$$F_{SE}(\lambda) = \begin{cases} F_{max}\frac{\exp\left(\frac{K_{sh}}{\lambda_{ref}}\lambda\right)-1}{\exp(K_{sh})-1}, & \lambda > 0 \\ 0, & \lambda \leq 0 \end{cases} \tag{3.16}$$

where

$$\lambda = \frac{l_{SE} - l_{sl}}{l_{sl}} \tag{3.17}$$

is the strain of the tendon beyond its slack length l_{sl}. Here F_{max} is the maximum muscle isometric force, K_{sh} is a shape factor, and λ_{ref} is a reference strain. K_{sh} determines where the force-length curve transitions from its flat lower ("toe") region to its nearly linearly behavior for large strains. λ_{ref} is the strain where $F_{SE} = F_{max}$.

The four parameters defining this tendon model (F_{max}, l_{sl}, K_{sh}, and λ_{ref}) are all morphological. The first two represent the size and the geometry of the muscle-tendon unit while the last two represent material properties of the tendon itself. It is these parameters that we will optimize to determine muscle state and force.

Muscle-Tendon Complex Dynamics Muscle and tendon act in series but are typically oriented obliquely. The angle between the two is known as the pennation angle θ and varies with time. The forces exerted by the tendon (SE), muscle (CE), and muscle tendon complex at large are:

$$F_{MTC}(t) = F_{SE}(t) = F_{CE}(\alpha(t), l_{CE}(t), \dot{l}_{CE}(t))\cos(\theta(t)). \tag{3.18}$$

The total length of the muscle tendon complex is

$$l_{MTC}(t) = l_{SE}(t) + l_{CE}(t)\cos(\theta(t)). \tag{3.19}$$

The pennation angle $\theta(t)$ varies so as to keep the width of the muscle approximately constant [60] and so can be written as a function of fascicle length:

$$\theta(l_{CE}) = \sin^{-1}\left(\frac{l_{opt}\sin(\theta_0)}{l_{CE}}\right). \tag{3.20}$$

Here the angle θ_0 is the pennation angle when $l_{CE} = l_{opt}$ (which is very near the resting length of the muscle [56]). It was found that allowing this angle to vary was necessary to obtain muscle fascicle trajectories that produced human-like metabolic cost estimates.

Joint Dynamics Finally we note that all muscles contribute to joint torque through their time-varying moment arms $r_i(t)$:

$$\tau_{mod} = \sum_i F_{MTC,i}(t) r_i(t). \tag{3.21}$$

We seek to determine each muscle-tendon force $F_{MTC,i}(t)$ and thereby resolve the issue of redundancy in joint actuation.

Model Inputs

There are two categories of inputs for each muscle in our model: (i) $\alpha(t)$, $l_{mtc}(t)$, and $r_(t)$- all estimated from the data and (ii) muscle-tendon morphological parameters $\vec{m}_i$

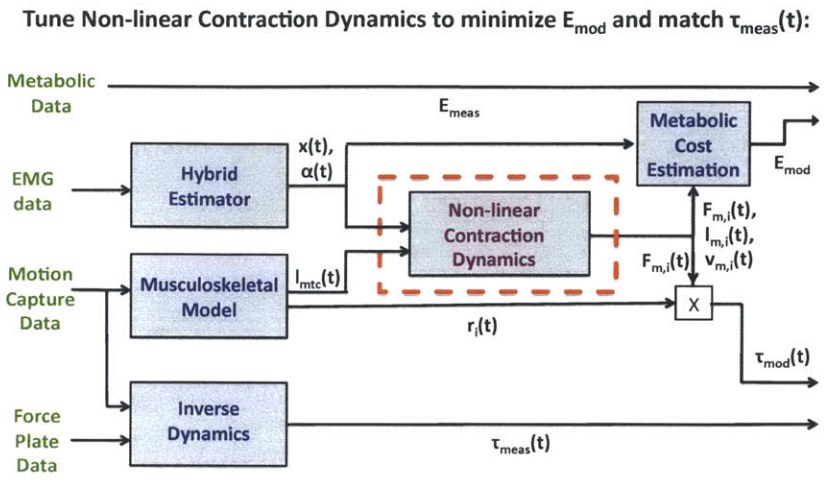

Figure 3-10: Muscle-tendon system identification procedure.

which will be identified via optimization. A flow chart of the procedure is shown in Figure 3-10.

Data Each muscle of the model was provided with fixed, averaged trajectories of $\alpha(t)$, $l_{mtc}(t)$, and $r_(t)$. Average trajectories were chosen as the model represents a simplified version of the actual *in vivo* system and we expected it to deal better with averaged rather than individual trajectories. This was especially critical with the activation estimates, as the EMG measurements were much more prone to noise and artifacts than the motion capture and force plate data sets.

Morphological Parameters Given the data inputs to the model, the muscle fascicle force and state are determined by the Hill-type contraction dynamics. These dynamics are parameterized by several values; notably muscle maximum isometric force F_{max}, length where active muscle force is maximal l_{opt}, fiber composition FT, tendon slack length l_{sl}, tendon shape factor K_{sh}, and tendon reference strain λ_{ref}. We evaluated the consequences of varying all of these variables, finding differing levels of

sensitivity for each. In the final analysis we fixed all of the variables to which the model was insensitive, choosing to vary F_{max}, K_{sh}, λ_{ref}, and an overall scaling factor for l_{sl} and l_{opt}. This last factor was chosen to ensure that the muscle operated in reasonable regions of its force-length space while preventing overfitting. The ratio l_{sl}/l_{opt} is known to vary significantly amongst muscles but not significantly in the same muscle amongst subjects [15], justifying this choice.

Parameter Identification Problem

To find the parameters that produce correct muscle force and state estimates we require an additional assumption. To that end we hypothesize that the muscle-tendon morphologies of the muscles comprising the leg have evolved to minimize the metabolic cost of walking at self-selected speed. Given the fundamental importance of bipedal walking as a means of transport this assumption seems plausible. Here we define self-selected speed to be the speed where MCOT is minimal. We seek a solution set of morphologies $\vec{m}_i$ that match the measured joint torques at the ankle, knee, and hip while using the smallest possible metabolic cost. To find that set we perform a multi-objective optimization with metabolic and kinetic cost functions, as described below.

Metabolic Cost Function Muscle metabolic consumption is known to depend on several factors including size, excitation level, activation level, length, velocity, force, and active force production [53]. Empirical studies on muscle shortening [25] and and lengthening [57] have demonstrated the rough shape of metabolic cost when plotted against muscle contraction velocity. It is intuitive that the metabolic cost of shortening is significantly higher than that of lengthening, as the muscle does positive work on the skeleton during shortening. A summary plot of these empirically observed trends is shown in Figure 3-11.

In this work we estimate metabolic consumption for each muscle through a relation derived by Umberger et al[53],[52]. This function has demonstrated exceptional predictive power in a number of applications and is the most widely-accepted metabolic

cost measure in the field. It expresses metabolic power per unit mass $\dot{E}$ as the sum of four terms:

$$\dot{E} = \dot{h}_A + \dot{h}_M + \dot{h}_{SL} + \dot{w}_{CE}. \tag{3.22}$$

Here $\dot{h}_A$ is the activation heat rate, which is associated with the transport of Ca^{2+} ions from the sarcoplasmic reticulum. $\dot{h}_M$ is the maintenance heat rate; both it and the shortening/lengthening heat rate $\dot{h}_{SL}$ are due to actomyosin interaction. $\dot{w}_{CE}$ is the mechanical work rate of the contractile element, normalized to muscle mass. For a given muscle, these terms depend on F_{max}, l_{opt}, FT (the percentage of fast-twitch muscle fiber), neural excitation, muscle activation, CE length, CE velocity, CE force, and CE isometric force. For a full mathematical description of these terms see [53] and the supplementary materials of [52].

To estimate full body metabolic cost, we first integrate $\dot{E}$ for each muscle of the leg, multiply by the appropriate muscle mass, and sum. Only one leg was modeled here so we assumed symmetry for the purposes of estimating cost in the other leg. For each muscle i the mass M_i is estimated to be

$$M_i = \frac{\rho F_{max,i} l_{opt,i}}{\sigma}, \tag{3.23}$$

where $\rho = 1059.7\text{kgm}^{-3}$ is the density of muscle and $\sigma = 0.25\text{MPa}$ is its specific tension. The metabolism for the rest of the body is estimated by multiplying the remaining mass by the measured basal rate E_{bas} ([W/kg]) of standing. The final metabolic cost in the model C_{met} in a time window T is then

$$C_{met} = \sum_i \left(M_i \int_0^T \dot{E}_i(t)\, \mathrm{d}t \right) + \left(M - \sum_i M_i \right) \dot{E}_{bas} T, \tag{3.24}$$

where M is total body mass and the sums are taken over all modeled muscles in both legs.

Kinetic Fit Cost Function In addition to minimizing metabolic cost, we seek solutions that most accurately reproduce the measured joint torques. We define the

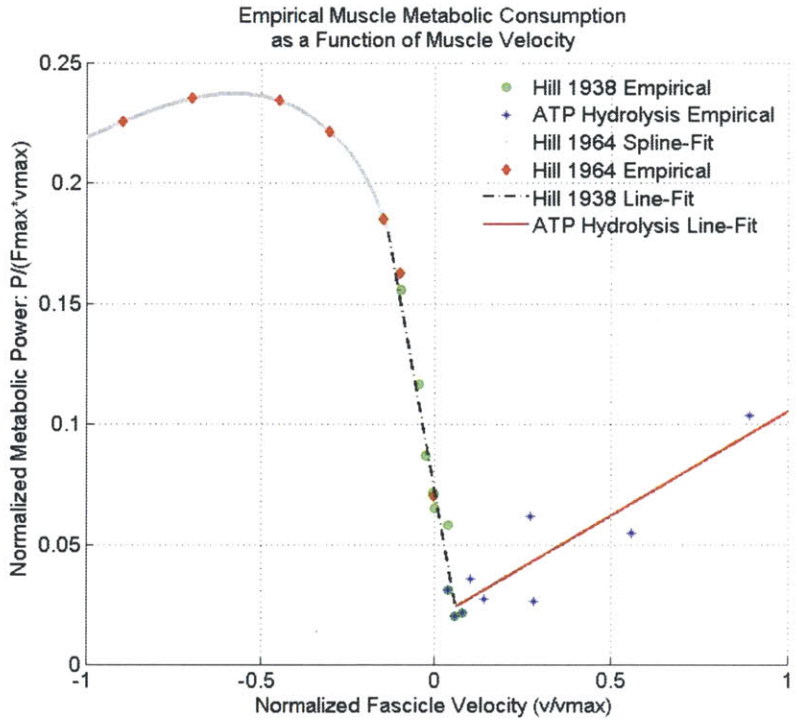

Figure 3-11: Empirically motivated metabolic cost function from [35].

corresponding cost C_{kin} as

$$C_{kin} = 1 - \frac{R^2_{ankle} + R^2_{knee} + R^2_{hip}}{3}, \tag{3.25}$$

where the coefficient of determination R^2 is defined to be

$$R^2 = 1 - \frac{\sum_i (y_{dat,i} - y_{mod,i})^2}{\sum_i (y_{dat,i} - \bar{y}_{dat,i})^2}. \tag{3.26}$$

In this way we measure the agreement of the model's kinetic output with the corresponding measured moments.

Optimization Implementation

The optimization of muscle tendon parameters $\vec{m}_i$ was implemented as a multiobjective optimization using the metabolic and kinetic costs C_{met} and C_{kin} described above. Below we elaborate upon (i) the tuning choices made, (ii) the optimization bounds, and (iii) the optimization algorithm.

Tuning Choices Many options regarding model and optimization variables were investigated before settling on the following tunings:

- F_{max}, K_{sh}, λ_{ref}, and a scaling factor that multiplies both l_{opt} and l_{sl} while preserving their ratio were chosen as the final muscle-tendon optimization variables. Optimization of just l_{sl} (as opposed to scaling l_{sl} and l_{opt}) was found to have similar results but sometimes led to upper leg muscles operating in unexpected regions of the force-length curve. A constrained optimization that varied l_{sl} and l_{opt} separately was also evaluated but found to have difficulty converging to a reasonable region. Optimization of muscle fiber composition and the normalization factor for scaling of neural excitation signals were also explored but decided against as neither was found to significantly impact results.

- Both the low pass filter and Sanger methods for estimating neural excitation were evaluated for use in the optimization. The Sanger method was chosen due to its more consistent timing with the required muscle activation profiles.

- Both the modified Geyer muscle model described above and model derived by Van Soest et al[54] and tweaked by Umberger et al[53] were investigated for application in the model. The Van Soest model accounted for activation and length dependence in the muscle force-velocity relation but its results were not found to significantly differ from those of the modified Geyer model. Hence the simpler, more numerically stable modified Geyer model was employed.

- The soleus and gastrocnemius tendons were modeled separately after finding that little change was incurred by including a separate compliance representing the Achilles.

- Due to the poor quality of the EMG signals gathered from the adductor longus and adductor magnus and their relatively small torque contributions normal to the sagittal plane, these two muscles were removed from the initial analysis. However a second analysis was conducted wherein these muscles (and the other

Parameter	Lower Bound	Upper Bound
F_{max}	$0.5 * F_{max,SIMM}$	$3.0 * F_{max,SIMM}$
l_{sl}, l_{opt} mult.	Ensure $l_m < l_{opt}(1+w)$	Ensure $l_m \geq l_{opt}(1-w)$
K_{sh}	2	5
λ_{ref}	0.02	0.09
θ_{HFL}	$-\pi/18$	$\lvert\min(\theta_{hip})\rvert$
K_{HFL}	0	$2 * \max(\tau_{hip})/\lvert\min(\theta_{hip})\rvert$

Table 3.3: Parameter bounds for optimization problem.

muscles of the hip, who also had poor EMG quality) were excited by profiles from literature [42]. Results of both analyses are given below.

- Each optimization solution was allowed to run for two gait cycles so as to sufficiently account for initial numerical transients. It was found that adding more gait cycles did not significantly impact the results, so we chose to evaluate two to minimize computational burden.

Bounds There are four parameters to be optimized for each muscle in the model with two additional parameters describing the hip flexor ligament. The bounds for these optimization variables were based upon values taken from the literature and scaled values from SIMM, as shown in Table 3.3. The maximum isometric force (F_{max}) values for each muscle were constrained to fall in a window surrounding the scaled value from SIMM. The scaling factor for l_{slack} and l_{opt} was chosen to ensure the muscle fascicle length stayed within reasonable physiological operating ranges. The bounds for K_{sh} and λ_{ref} were taken from [56]. The bounds for the spring constant of the hip flexor ligament was chosen so that the ligament could provide anywhere from none to all of the required hip flexion moment near toe off. The engagement angle was chosen so that the tendon could engage with the hip no more than 10° flexed, as its physiological role is to prevent overextension.

Optimization Algorithm The model was constructed using MATLAB and Simulink (The Mathworks, Natick, MA). Computations were carried out using the Mathworks Cloud Center, a computer cluster operated through Amazon Web Services. The opti-

Optimizer Setting	Value
PopulationSize	1000
EliteCount	25
Generations	100
MutationFcn	mutationadaptfeasible
CrossoverFraction	0.8
Vectorized	On
PopInitRange	Full Space

Table 3.4: Optimization settings in MATLAB.

mization algorithm employed was MATLAB's gamultiobj, a controlled elitist genetic algorithm that is a variant of the NSGA-II algorithm [14]. The relevant algorithm settings are given in Table 3-4. Note that both the population size and number of generations were taken to be deliberately large to force the optimizer to thoroughly search the space.

3.2 Results

The optimization scheme described above was run for each of the five study participants. Parameters were sought that both minimized the metabolic cost of transport of self-selected speed walking and maximized the fit to the kinetic data. Because we found the results to be limited by the poor quality of the EMG measurements in the muscles spanning the hip we present results under two conditions; first using only measured EMG profiles and then with the excitation profiles for the monoarticular muscles spanning the hip (ILL, GMAX, GMED, ADDL, ADDM) being replaced by profiles from the literature [42]. The second case is not ideal but demonstrates the potential for improvement in model results if reliable EMG profiles can be obtained around the hip.

A typical solution space is shown in Figure 3-12. The red dots represent the Pareto front; that is the set of solutions where it is not possible to improve upon one objective without compromising on the other. Each point along that front is optimal for some choice of weighting of the two objectives. In the ideal scenario the

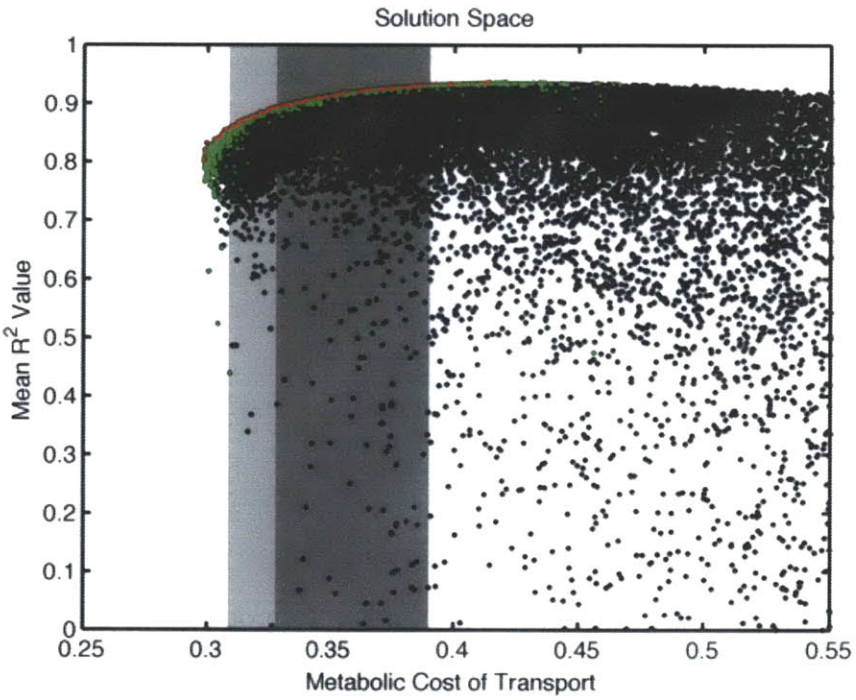

Figure 3-12: Typical solution space for optimization problem.

solution space would form a sharp corner and the Pareto front would converge to one solution that optimizes both objectives. That is not seen to be the case in our problem, possibly because of imperfections in the data and inaccuracies introduced by the lumping together of muscles. Hence our task is to find the region of the Pareto front where the solutions predict the true human muscle behavior.

3.2.1 Choosing an Optimal Solution

To choose an optimal parameter set, we examine all solutions along the Pareto front. As can be seen from Figure 3-12, three regions are evident. On the left are solutions with relatively low metabolic cost but which fail to track the measured joint torque profiles. The performance of these solutions is typically accounted for by F_{max} values that are too small. On the far right are solutions with the best kinetic agreement but high metabolic costs. In essence these solutions are overfitting; they try to drive one or more muscles harder than they should so as to force agreement with the observed kinetics. Un-modeled muscles and deficiencies in the data sets (EMG in particular)

preclude a perfect fit, so this extra effort is non-physical. The solutions that represent the human should be somewhere between these two extremes, producing a good kinetic fit at a reasonable metabolic cost.

To determine where the optimal solution lies, we consult the metabolic energy budget of each subject. Figures 3-13 (all excitations estimated from EMG) and 3-14 (monoarticular hip muscle excitations from literature) plot the fraction of full body metabolic cost consumed by each muscle as a fraction of the maximal average R^2 that the model achieves for kinetic fit. As can be seen from the plots, the budget is fairly consistent for low to moderate average R^2 and energy expenditure, then sees one or a few muscles begin to dominate as the high R^2/metabolic cost range is approached. Typically one to three muscles overexert themselves to force a marginally better kinetic fit, differing from the distribution of cost at lower energies. Physically this would lead to fatigue of the muscle in question, or in it being modeled as much larger than its actual size (since muscle mass is proportional to F_{max}). Hence for each optimization we chose a cutoff point just before the questionable muscles begin to ramp up their loads. The optimal solution is defined as the point along the Pareto front with maximal kinetic fit below this cutoff. It should be noted that for some subjects the vastus lateralis (VAS) increases its load along virtually the whole Pareto front. This is likely due to the large size of this modeled muscle; if it does not adequately match the knee extension moment in early stance the optimizer will throw progressively more energy into that muscle to improve the fit, which dominates the metabolic cost. In this case we based the cutoff upon a different muscle so as to capture the sudden change in regime described above. As can be seen from the figures, the approach worked more cleanly when excitation profiles from the literature were employed at the hip (as should be expected). Table 3.5 displays the cutoffs and muscles upon which they were based for each case.

3.2.2 Metabolic Cost Predictions

The optimal solutions are plotted with respect to their solution spaces and measured metabolic cost in Figures 3-15 and 3-16. In these figures the dark gray bands are the

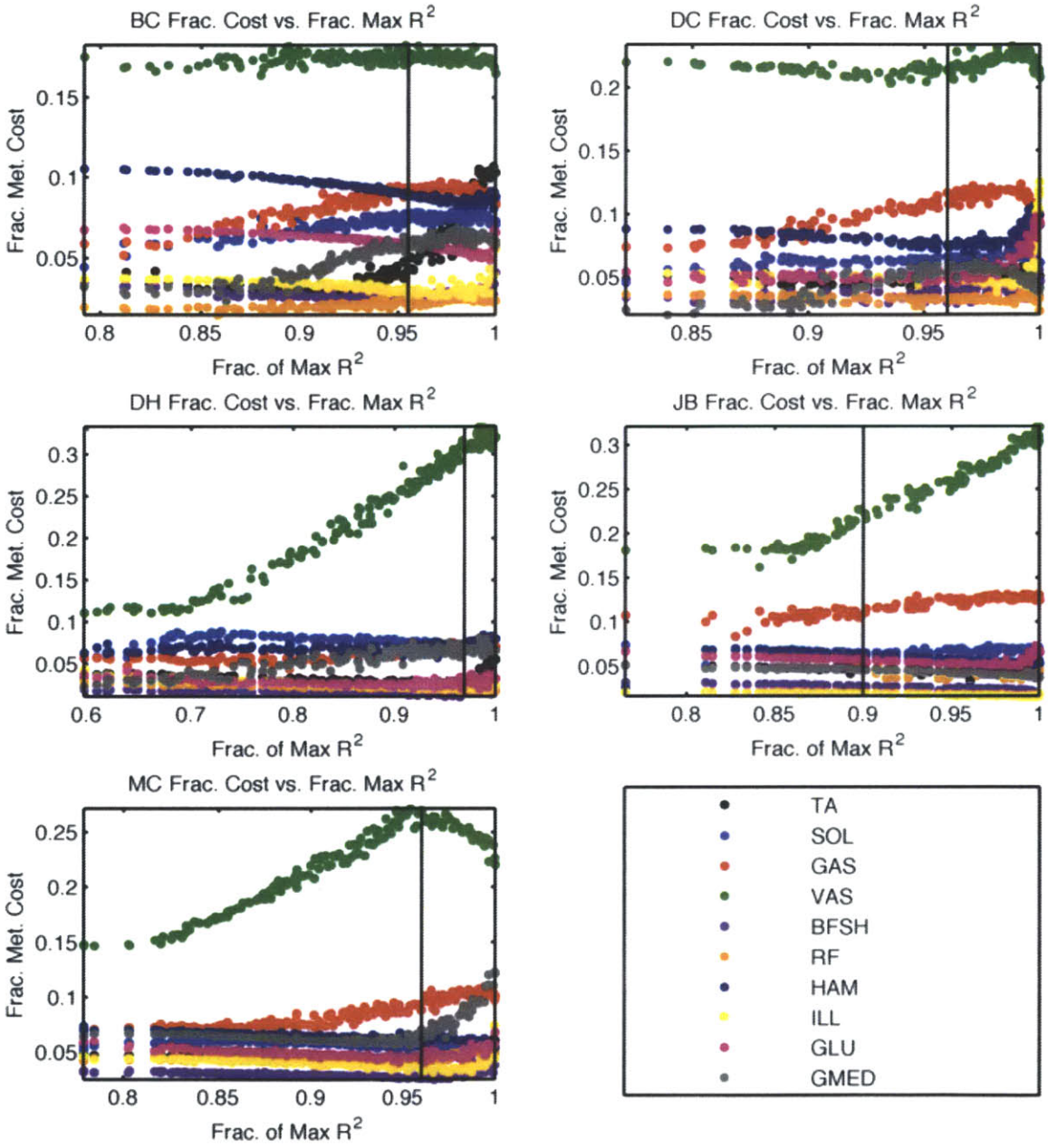

Figure 3-13: Metabolic budgets for all subjects plotted vs. kinetic agreement. The vertical line in each plot represents the chosen cutoff point. Here hip muscle excitations were estimated using only collected EMG data.

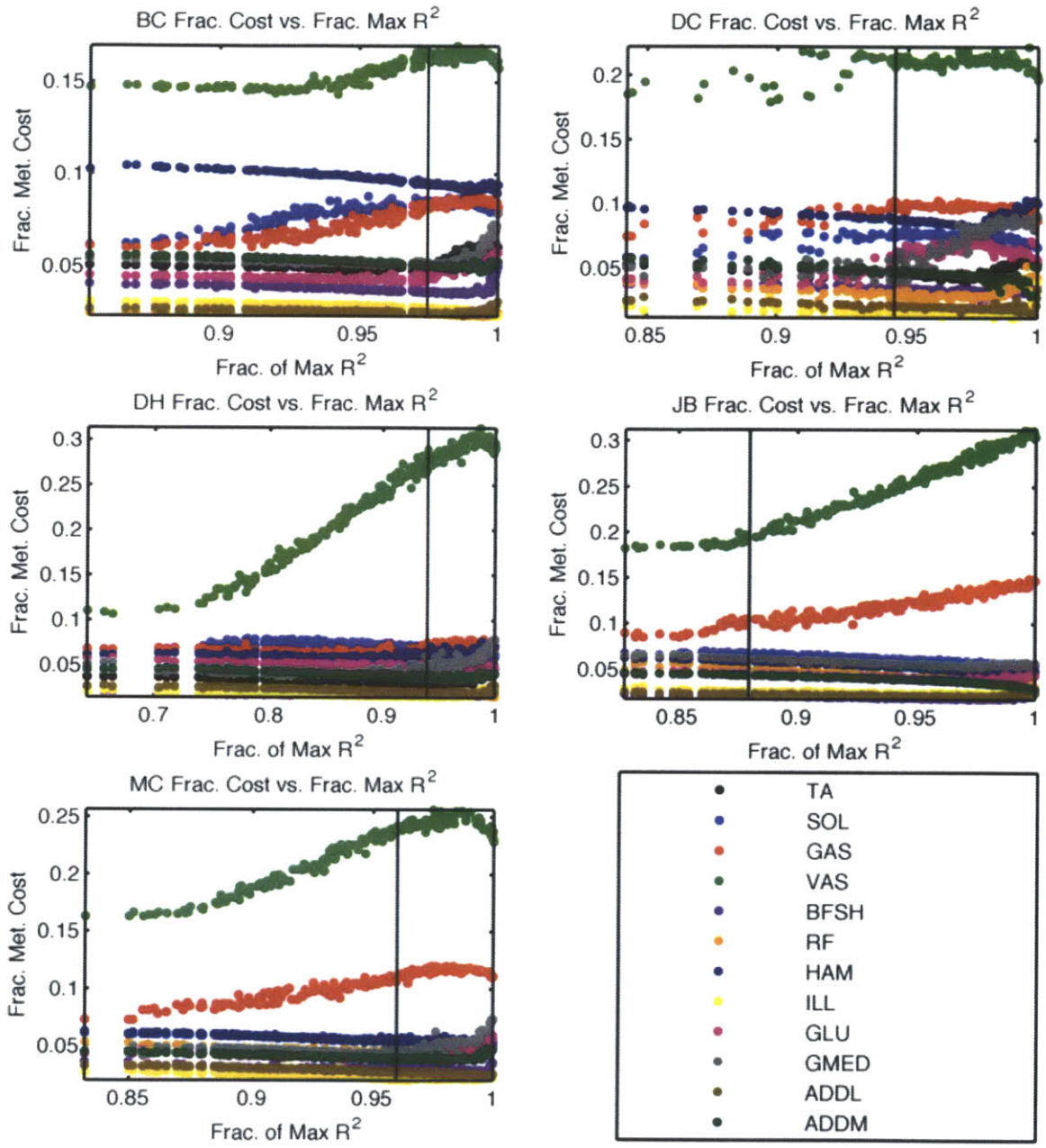

Figure 3-14: Metabolic budgets for all subjects plotted vs. kinetic agreement. The vertical line in each plot represents the chosen cutoff point. Here literature values [42] were used to estimate neural excitations in the monoarticular muscles spanning the hip.

	Mono. Hip Excitations from Data		Mono. Hip Excitations from [42]	
Subject	Cutoff R^2 (% of Max.)	Muscles Based Upon	Cutoff R^2 (% of Max.)	Muscles Based Upon
BC	0.955	TA	0.975	TA, GMED
DC	0.960	VAS, GMAX	0.945	GMED
DH	0.970	TA	0.940	GMED
JB	0.900	GAS	0.880	GAS, VAS
MC	0.960	GMED	0.960	GMED

Table 3.5: Cutoffs used to determine optimal solutions and the muscles they were based upon.

full range of minimal MCOTs observed from all subjects while the light gray bands are the minimal MCOT for the subject being plotted.

The numerical MCOT estimates from both methods are compared with the empirically measured values in Table 3.6. From these we see that both methods produce accurate metabolic cost predictions when averaged over all subjects. However only the method which includes literature-derived excitation estimates at the hip allows for accurate metabolic prediction for individual subjects. This is not surprising given the noisy nature of our data sets and the relatively pristine condition of the wire EMG data sets obtained in [42]. There is undoubtedly some inter-subject variation unaccounted for when using these profiles with the rest of our data set; however the most critical piece for the analysis is the timing of the excitation profiles and these are known to be relatively consistent across subjects.

We can also visualize the ability of the model to estimate metabolic cost by looking at the superposition of all solution spaces and where it falls relative to empirically measured metabolic cost (Figure 3-17). We observe that (for both methods of deriving hip muscle excitations) the solutions begin to transition from high cost, maximal kinetic fit to low cost, poor kinetic fit in the region of human metabolic cost.

3.2.3 Resolving Redundancy in Joint Actuation

One of the stated objectives of this work was to resolve the redundancy in joint actuation, i.e. to determine the contributions of each modeled muscle to joint torque. With estimated muscle-tendon lengths, moment arms, activations, and morphologies in hand we can now evaluate the roles of individual muscles. Figure 3-18 shows the

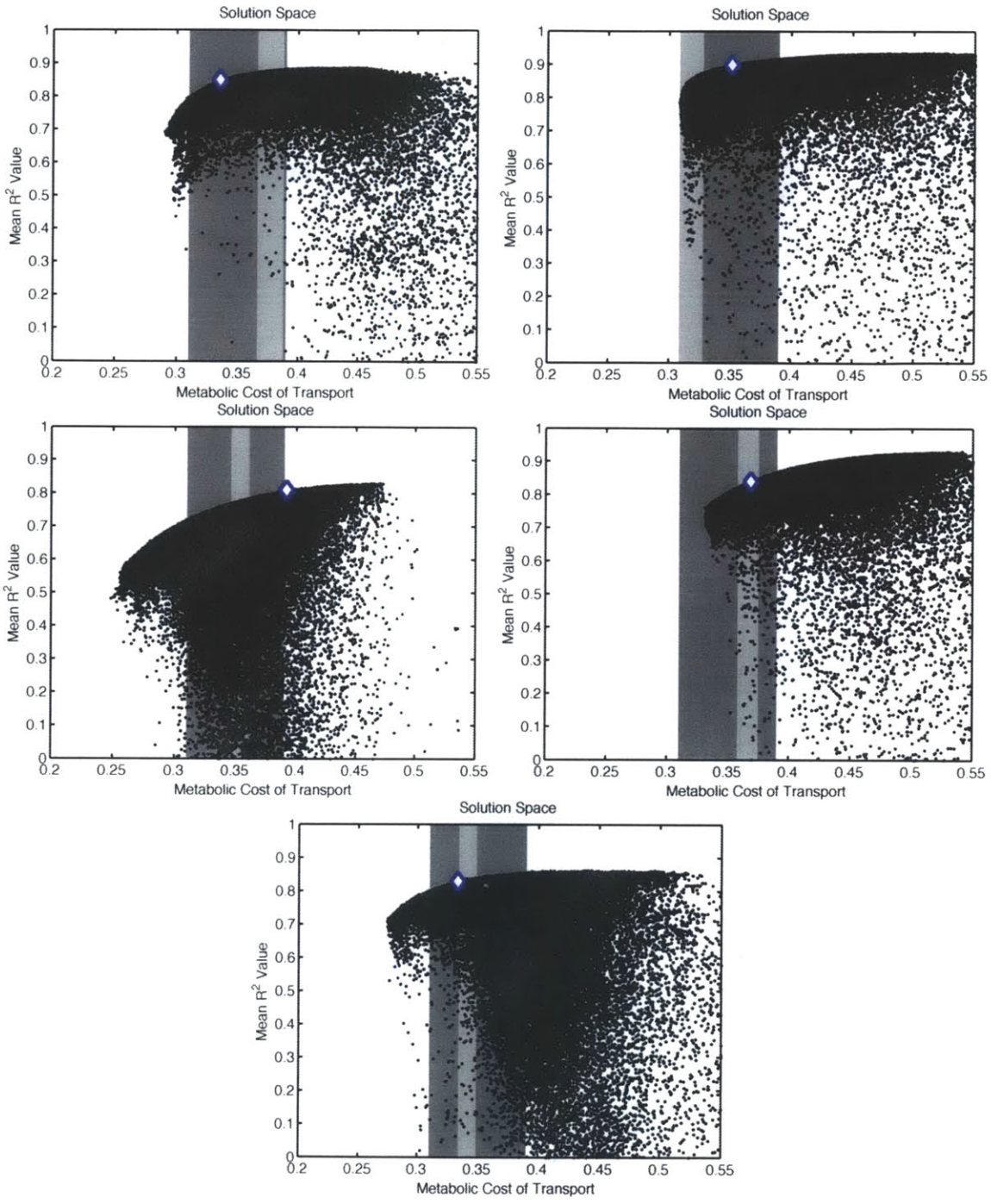

Figure 3-15: Best solution for each participant and its relation to measured MCOT (light gray band) and MCOT range for all participants (dark gray band). Here hip muscle excitations were estimated using only collected EMG data.

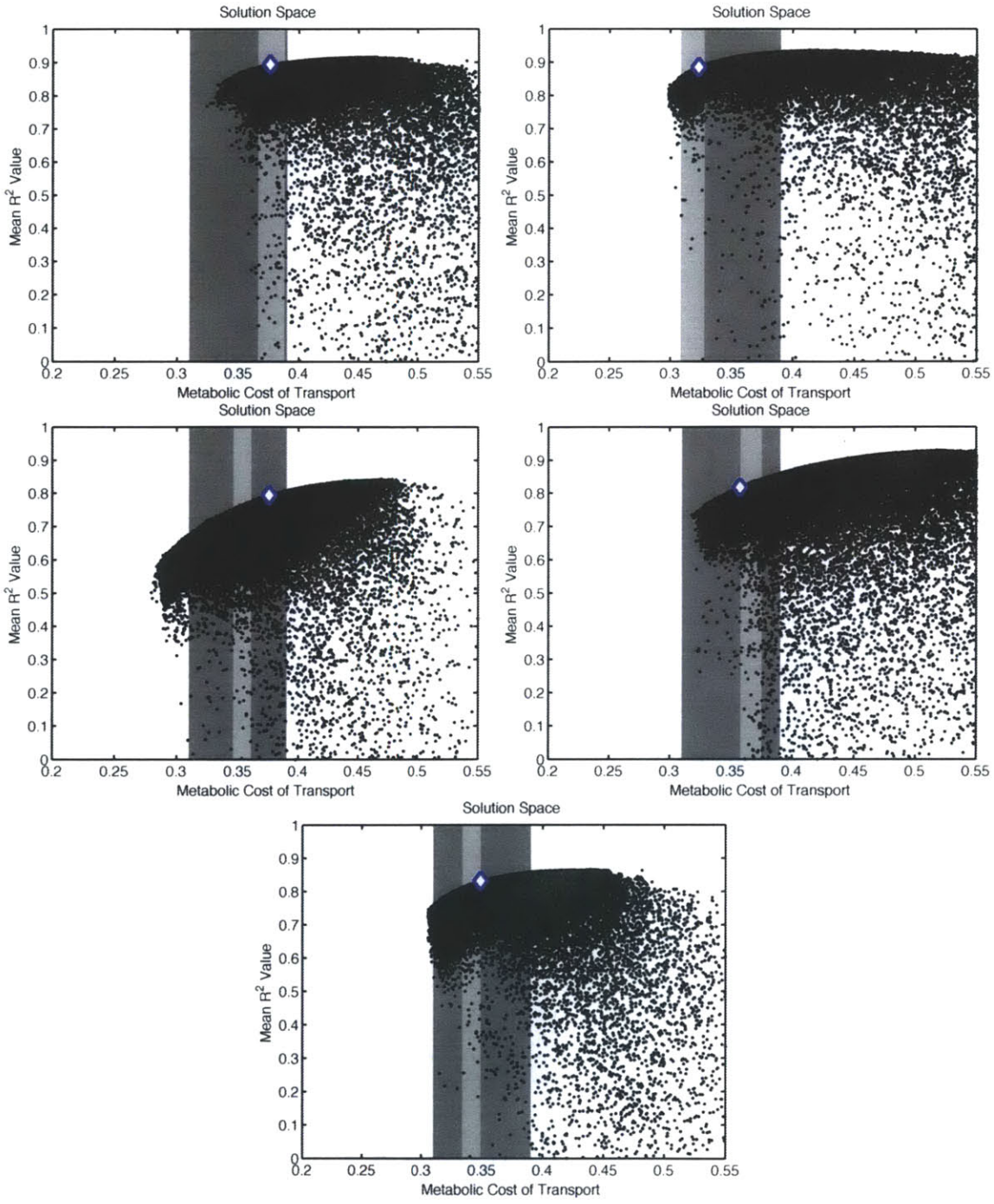

Figure 3-16: Best solution for each participant and its relation to measured MCOT (light gray band) and MCOT range for all participants (dark gray band). Here literature values [42] were used to estimate neural excitations in the monoarticular muscles spanning the hip.

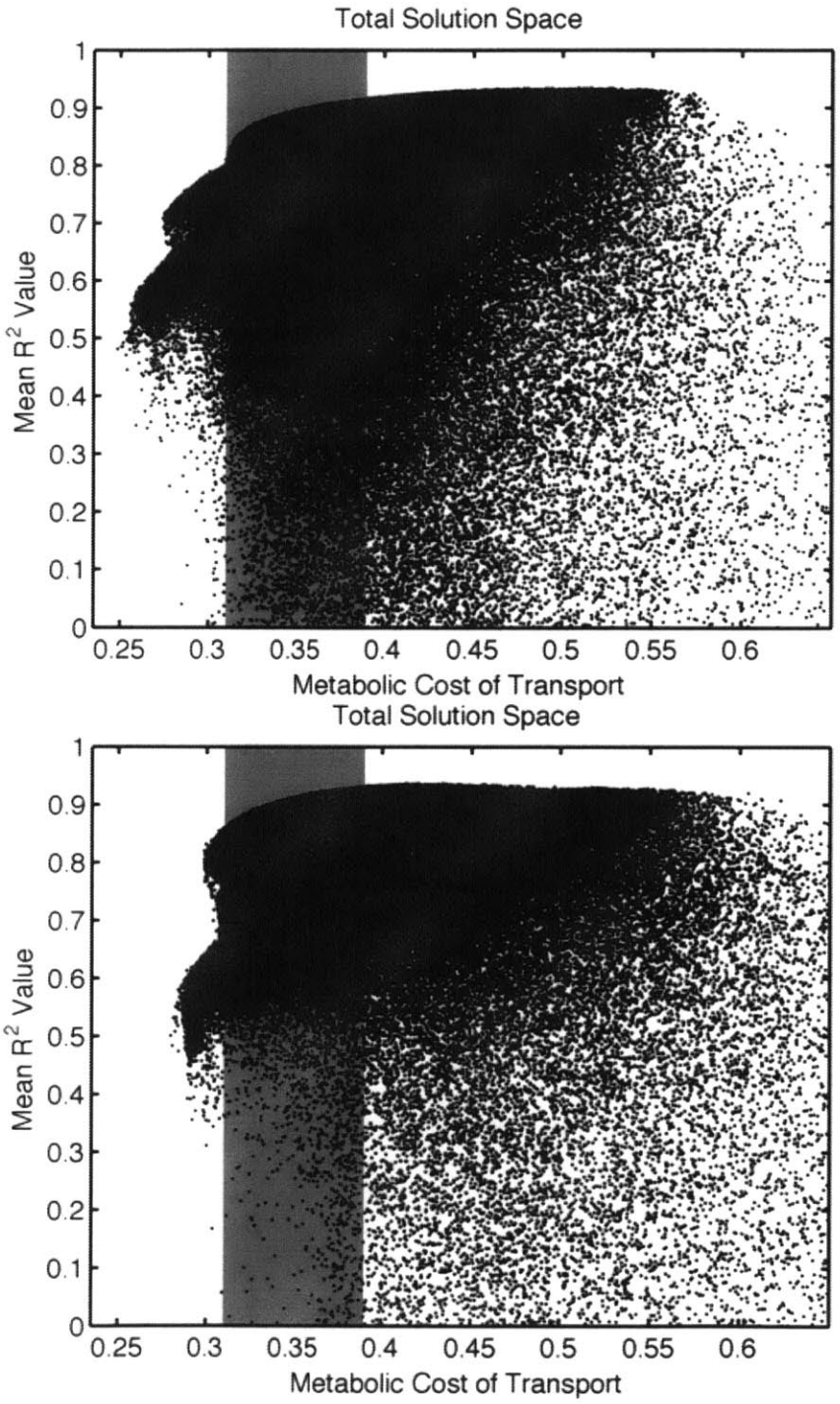

Figure 3-17: Total of all solution spaces. The top plot was formed using hip muscle excitations derived exclusively from EMG data while the bottom plot was formed using literature profiles [42] to estimate neural excitations for the monoarticular muscles spanning the hip.

Subj.	Empirical MCOT	Mod. MCOT (Data)	Mod. MCOT ([42])
BC	0.38 ± 0.01	0.34	0.38
DC	0.32 ± 0.01	0.35	0.32
DH	0.35 ± 0.01	0.39	0.38
JB	0.37 ± 0.01	0.37	0.36
MC	0.34 ± 0.01	0.33	0.35
Mean	0.35 ± 0.02	0.36 ± 0.02	0.36 ± 0.02

Table 3.6: Metabolic cost estimates from data and both versions of the model. The first model column uses monoarticular hip excitations from the data while the second uses profiles from [42].

breakdowns at the ankle, knee, and hip for one subject. It should was observed that the muscle-by-muscle breakdown was quite consistent among our five subjects.

3.2.4 Evaluating Muscle State

As discussed previously, knowledge of joint kinematics, muscle-tendon morphology, and muscle activation allows for the exploration of muscle force and state. Figure 3-19 shows the length and velocity trajectories for each muscle fascicle for one subject. Both the fascicle length and velocity predictions are fairly consistent among subjects, with the exception of the overall offset of the fascicle length relative to l_{opt}. However if the fascicle length is expressed in terms of strain relative to its length at heel strike, all subjects show similar fascicle length trajectories.

In general, muscle fascicle state is very difficult to measure. Ultrasonography is the only current means to obtain these profiles, and it is really only practical for the relatively short, distal muscles of the leg. In figure 3-20 we compare our fascicle trajectories with the profiles available from published ultrasound studies. In each case we plotted the appropriate muscle for only the subject who was most closely matched to the average height and weight of the empirical study. The soleus and gastrocnemius profiles came from Ishikawa et al[31], while the vastus lateralis profile came from Chleboun[9]. In all cases qualitative agreement is observed. We believe that observed differences come from (i) the difference in walking speed between our

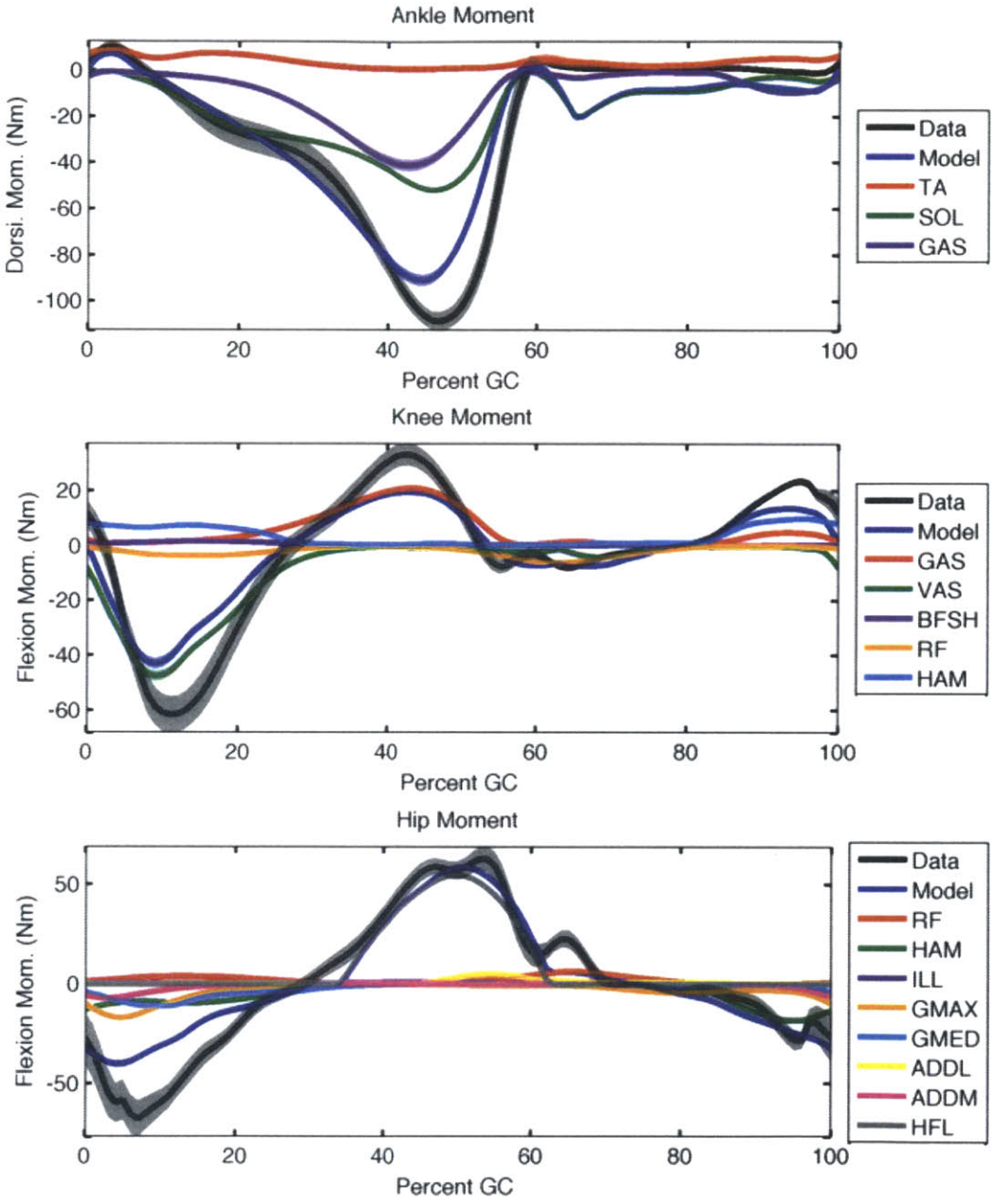

Figure 3-18: Contributions of individual muscles to joint torques for one subject.

study and the literature, (ii) natural variation in the kinematics of early stance, which affects the initial muscle length for normalization, and (iii) uncertainty in the breakdown of what constitutes muscle and what constitutes tendon in such studies.

Knowledge of muscle force and state also allows for the power output of the muscle tendon unit to be broken into individual contributions from the muscle and tendon. These outputs are plotted for one subject in Figure 3-21. Note the large contribution of the tendon (red), particularly in the more distal muscles where tendons are longer relative to the fascicle.

3.3 Discussion

In this study we have investigated the interplay of neural control and muscle-tendon structure in human walking. Using a hidden state estimator for muscle activation and an optimization-based system identification technique for inferring structural parameters we have generated estimates of muscle metabolic consumption, force, and state. Metabolic consumption is found to quantitatively match empirical measurements in four out of five subjects and on average. While *in vivo* measurements of muscle fascicle length are rare, our model does qualitatively match published profiles for the soleus, medial gastrocnemius, and vastus lateralis. We hope that future empirical studies, perhaps with implantable sensors, will be able to further validate the results of our model.

There are many observations and predictions that can be made using our estimated muscle state profiles. As can be seen in Figure 3-11 and was emphasized in [19], muscle is metabolically efficient when operating isometrically. This quality is utilized in our results as the tibialis anterior, soleus, gastrocnemius, biceps femoris short head, rectus femoris, illiacus, gluteus maximus, and gluteus medius all undergo long stretches of the gait cycle where they are nearly isometric. A.V. Hill [26] demonstrated that skeletal muscle maximizes its operating efficiency while shortening at $v_{CE} \approx -0.17 v_{max}$, and nearly all of the muscles of the leg are seen to spend a portion of the gait cycle operating in that region. Hill also showed that muscles maximize their

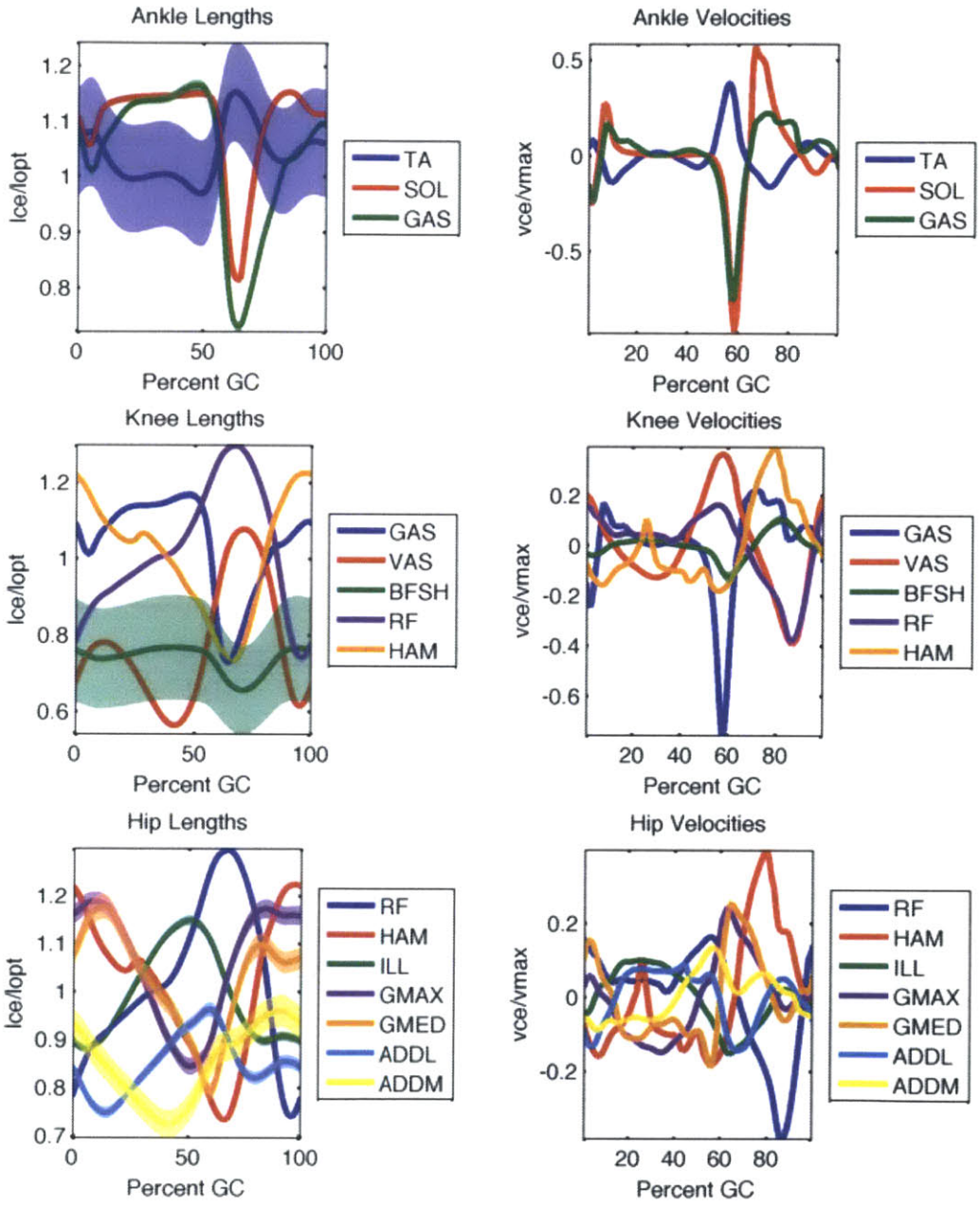

Figure 3-19: Muscle fascicle length and velocity trajectories for one subject.

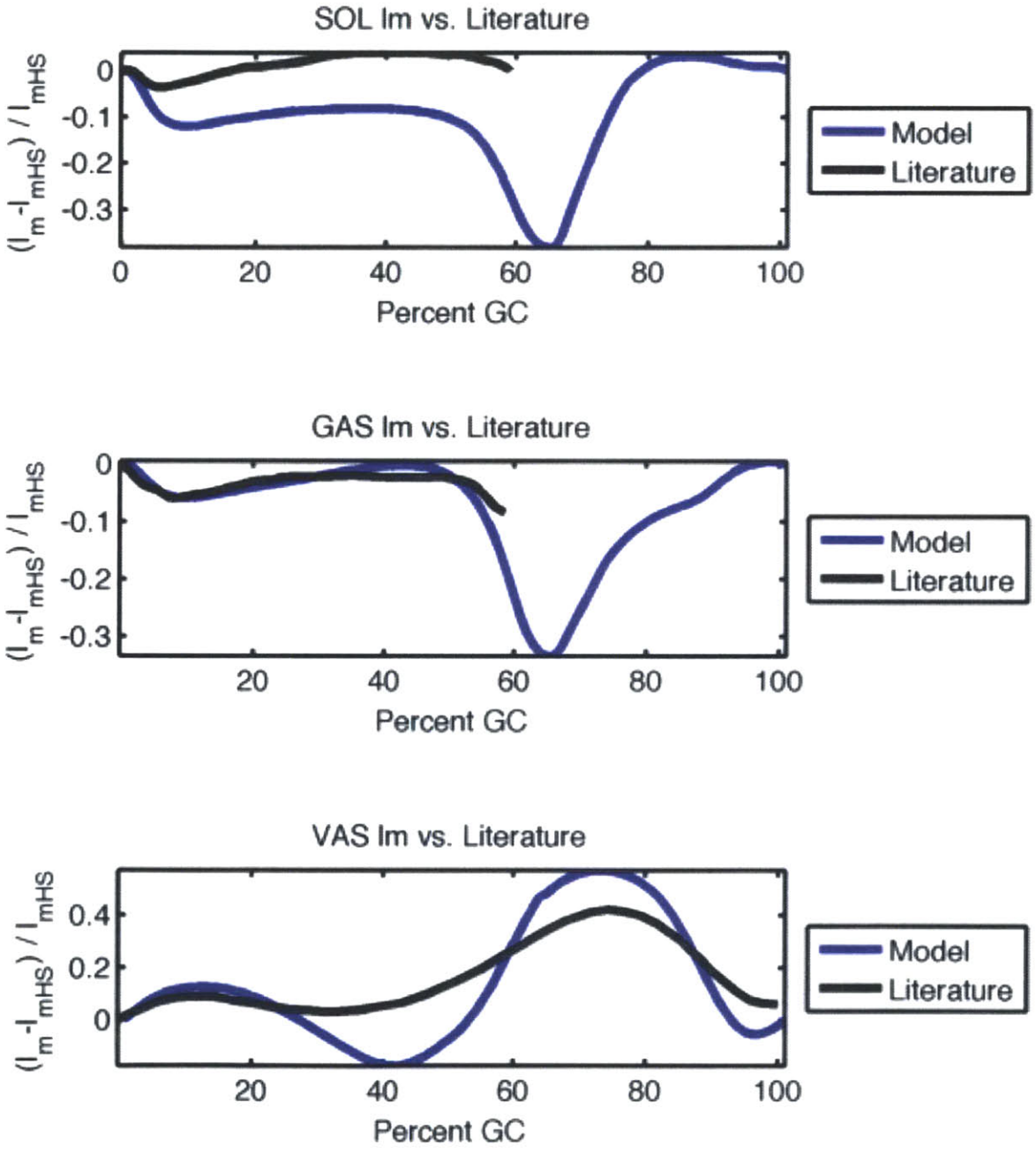

Figure 3-20: Comparison of modeled fascicle lengths to trajectories measured via ultrasound.

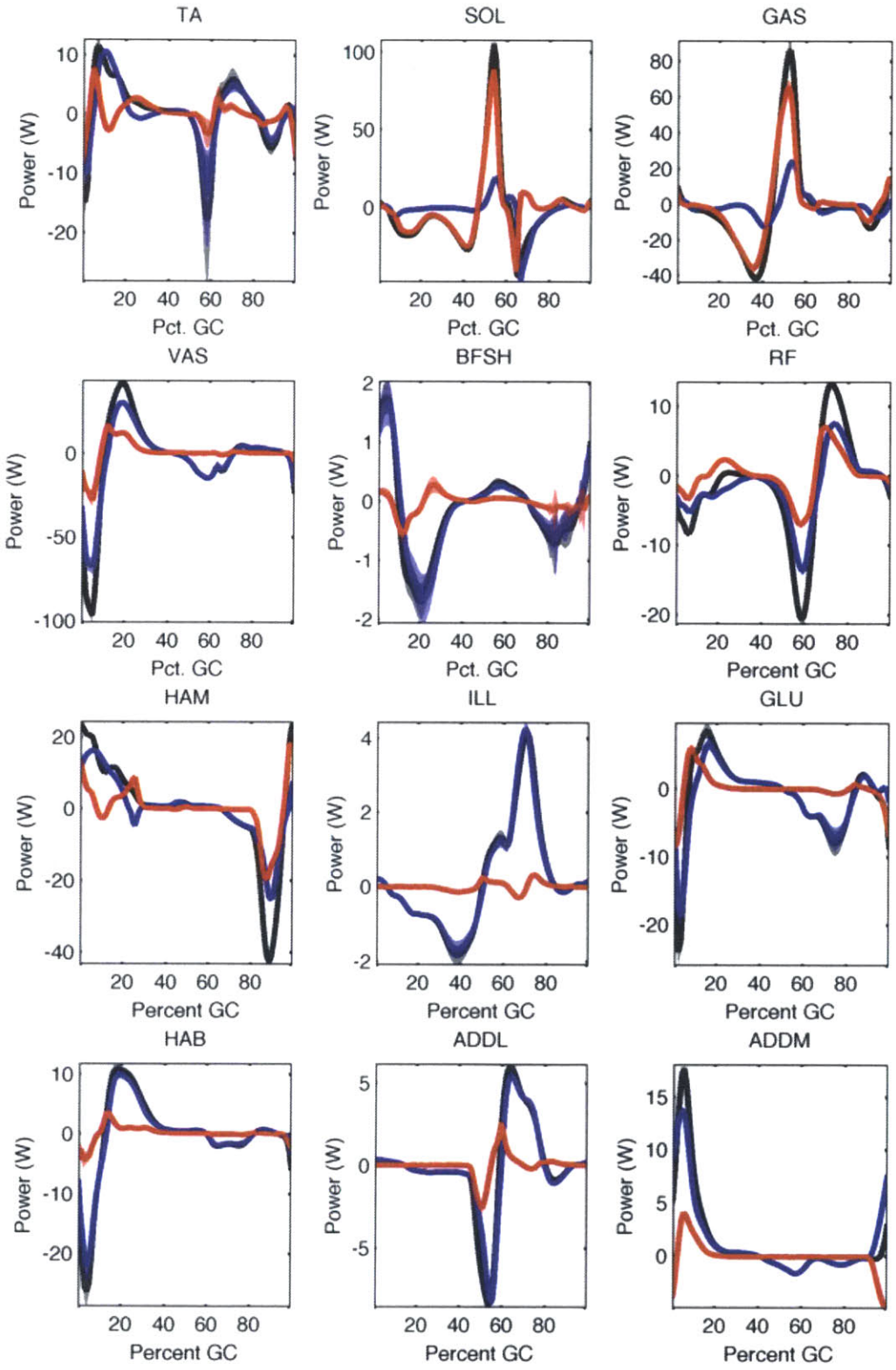

Figure 3-21: MTU, muscle, and tendon powers for all muscles. In the figures the black traces are the muscle-tendon unit power outputs, the blue traces are the muscle power outputs, and the red traces are the tendon power outputs.

power output at around $v_{CE} \approx -0.30 v_{max}$ [26]. In our study we see that the soleus and gastrocnemius operate near that speed just before toe-off, providing the power required to transition from stance to swing. However most other muscles appear to move more slowly during self-selected speed gait, seeking to maximize efficiency.

While our approach does provide several predictions that corroborate with empirical measurements, it is somewhat limited by our data set and some of the assumptions made in building the model. Most notable is the poor quality of the EMG data in the muscles spanning the hip. As seen above, the metabolic predictions of the model may be improved by using literature-based data for the neural excitations of the monoarticular muscles spanning that joint. While this does not account for subject-to-subject variation it should at least provide the correct timing for neural stimulation profiles, and our results indicate that this is of critical importance. We would likely improve our results by using fine wire EMG to measure these muscles, enabling predictions under a broader set of conditions. In particular we would like to validate our model for walking at different speeds. As one walks faster the hip muscles significantly increase their activation; without proper EMG data this scaling is unknown so the model is missing a fundamental input. One could imagine determining the muscle-tendon parameters using measurements of walking at self-selected speed and then applying and testing them under a variety of different conditions-differing speeds, differing terrains, possibly even running.

One other way the model could be improved is through the inclusion of more muscles. For instance the deficiency exhibited in ankle moment during late stance is likely due to the exclusion of smaller plantar flexor muscles which are known to engage during that time [42]. Similarly the lumping of the three hamstring muscles (semimembranosus, semitendinosus, and biceps femoris short head) may be responsible for some of the deficiencies observed in the knee flexion moments throughout the gait cycle. Further resolution of these and other muscle groups where the muscle activations are not quite concurrent and the muscle-tendon lines of action are not quite aligned would likely prove beneficial. A thorough data collection using wire EMG on this expanded muscle set could greatly improve the predictive power of this

approach.

Chapter 4

Pilot Application to Powered Ankle-Foot Prosthesis Control

Control schemes for powered ankle-foot and knee prostheses would benefit greatly from a means to make them inherently adaptive to different walking speeds. One approach to achieving this is to emulate the intact human leg, as it is capable of seamless adaptation. Human locomotion is known to be governed by the interplay among legged dynamics, morphology, and neural control including spinal reflexes. It has been suggested that reflexes contribute to the changes in joint dynamics that correspond to walking at different speeds. It is therefore natural to seek adaptive prosthesis behavior through control by a neuromuscular model driven by reflexes. In this chapter we describe the application of a simplified version of our model in the control of a powered ankle-foot prosthesis[1] . The control scheme was tested by a transtibial amputee walking at three speeds and seen to produce speed adaptive behavior; net ankle work increased with walking speed, highlighting the benefits of applying neuromuscular principles in the control of adaptive prosthetic limbs.

[1]This chapter is taken largely from [37].

4.1 Background

The human ankle generates net positive mechanical work during gait at moderate to fast walking speeds. During stance phase, commercially available ankle-foot prostheses only store and release elastic strain energy and thus cannot generate net ankle work. To restore biological ankle function, self-contained powered prostheses have recently been developed with the capability to reproduce physiological levels of net mechanical work [5],[27],[50]. While these prostheses can reduce the metabolic cost of the wearer [6], many control challenges remain in realizing the potential of these devices for walking under diverse conditions, such as varying terrains and speeds. Toward this end, we here focus on the advancement of a speed adaptive control strategy for a powered ankle-foot prosthesis.

To develop a speed adaptive controller, we consider the biomechanical changes in human ankle behavior across speed. A change in walking speed corresponds to a change in the relationship between ankle joint state (angle and derivatives) and joint torque. One way to encode these speed-adaptive variations in a prosthetic control scheme is to program the prosthesis with fixed mathematical functions defined by parameters that vary across speed [50]. However, this strategy requires supervisory controllers to explicitly vary function parameters as walking speed changes [50]. An alternative is a method described in [30], which uses tibia global angular position and angular velocity to measure gait cycle location regardless of stride length, thus enabling speed adaptation. This has the advantage of not requiring walking speed measurements from the device, preventing measurement errors and latency in parameter changes from affecting performance. We propose another method to achieve inherent speed adaptability by implicitly encoding speed-correlated torque-state variations in a biophysically inspired function. This method also does not require an explicit measurement of walking speed and may provide more potential for adaptability over a broader range of conditions.

Such a function can be developed by emulating muscle reflexes, i.e. muscle behaviors that are mediated by neural circuits that are confined to the spinal cord [33].

It has been suggested [55] that afferent feedback is important in enabling walking speed-dependent biomechanical changes. Reflexes offer a dynamic means to rapidly communicate mechanical changes to the neuromuscular system, and so may enable joint power generation to be appropriately timed across speed [55]. Thus, reflexes may provide a biophysical basis for closed-loop feedback control of ankle dynamics across speed.

Human motor control is believed to be composed of both a feedforward neural drive and a reflexive feedback component [33],[55]. Nonetheless, models controlled with only local reflexive feedback loops are able to produce walking simulations that qualitatively agree with human gait dynamics and muscle activations [21]. This purely feedback-based approach has been applied to a powered ankle-foot prosthesis to control it as if it were driven by a human muscle with a local force feedback reflex [17]. This system exhibited slope-adaptive behavior but the use of a force-feedback reflex alone, without parameter interventions, did not result in the biological trend of increasing net ankle work across speed [16]. Empirical studies such as [2] have established the existence of length-based as well as force-based afferent feedback to the plantar flexors during stance in walking. Hence, other reflexes may be required in tandem with force feedback to produce speed-adaptive functionality, although the specific reflex pathways required and the quantitative details of their contributions are not yet known.

Here we propose that a neuromuscular modeling framework, when duly considering the interplay between musculoskeletal dynamics and neural control, can provide insight into reflex pathways contributing to ankle function in walking gait. Specifically we hypothesize that a neuromuscular model composed of length, velocity, and force feedback in the posterior leg muscles, when used to control a powered ankle-foot prosthesis, can exhibit speed-adaptive behavior by producing a trend of increasing ankle joint net work with increasing walking speed. To evaluate this hypothesis, we first developed the proposed modeling framework based on kinematic, kinetic and electromyographic gait data from an intact-limbed subject. We then used the resulting neuromuscular model to control a powered ankle-foot prosthesis worn by a

transtibial amputee walking at three distinct speeds.

4.2 Methods

4.2.1 Modeling

Reflexes, among other neural pathways, dynamically link muscle force and state to muscle activation [33]. To specify a reflex-based controller one would require profiles of muscle force, state, and activation, all of which are difficult to access. Muscle state has a nonlinear dependence on tendon action and joint mechanics. Activation cannot be known *in silico* without quantifying the neural control pathways involved, which are unknown a priori and are what we set out to find in the first place. As a resolution to this difficulty we chose to estimate activations from electromyographic (EMG) data of healthy walking subjects, since the data already incorporates the dynamic effects of neural control within the subject. With the activations (effective control commands) and ankle angles from gait data, we actuated a dynamical model of the plant (consisting of ankle muscle-tendon units) and estimated muscle state profiles. The estimates of muscle state and activations were used to derive a reflex architecture that may contribute significantly to walking, as well as to quantify reflex parameters that are consistent with the muscle-tendon dynamics. This overall framework, shown in Figure 1, emphasizes the interplay of legged dynamics with neural control.

The biological data forming the basis of the above modeling scheme were composed of kinematic, kinetic and EMG measurements. Data were collected with approval from the MIT Committee on the Use of Humans as Experimental Subjects at an instrumented motion analysis facility in the MIT Computer Science and Artificial Intelligence Lab. After obtaining informed consent, a healthy male participant was asked to walk barefoot at self-selected speed (1.25 m/s). Standard motion capture techniques (described in [35]) were employed to collect the kinematic and kinetic data. Surface EMG recordings were obtained from the soleus, medial gastrocnemius, lateral gastrocnemius and tibialis anterior muscles of one randomly chosen leg in the

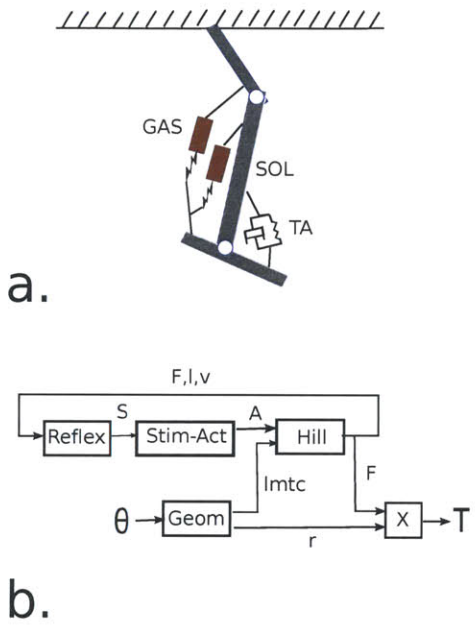

Figure 4-1: (a) Musculoskeletal model applied in prosthesis controller. The two plantar flexors are modeled as muscle-tendon complexes while the dorsiflexor is modeled as a unidirectional rotary spring-damper. (b) Block diagram describing an individual reflex-based controller. The input is composed of joint angles θ (ankle and knee for GAS; just ankle for SOL) and the output is the muscle contribution T to ankle torque. The four blocks represent the geometrical mapping from angle to l_{mtc} and ankle moment arm (Geom) , the reflex structure (Reflex) , the stimulation-to-activation dynamics (Eq. 3, block Stim-Act), and the Hill-type muscle model [21],[17] (Hill).

presence of a physician. A total of 25 walking trials within 5% of self-selected speed were collected. The walking trials were repeated on multiple days (with consistent calibrations) to test the robustness of modeling and estimation techniques to day-to-day differences.

Muscle activations were estimated from EMG data using a technique reported in [35]. Standard preprocessing techniques [10] were applied to the signal before applying a causal, recursive, and vectorized implementation of the Bayesian algorithm described in [45]. This algorithm models muscle activation as a slow diffusion process driven by calcium sourcing and sinking jump processes and produces an output $x(t)$. This output does not take into account the difference in activation and deactivation rates, which is critical to the timing of activation buildup. Consequently $x(t)$ was passed through the calcium-activation dynamics described in [60]:

$$\frac{d\alpha(t)}{dt} + \left[\frac{1}{\tau_{act}}(\gamma + (1-\gamma)x(t))\right]\alpha(t) = \frac{1}{\tau_{act}}x(t), \tag{4.1}$$

where $0 < \gamma = \frac{\tau_{act}}{\tau_{deact}} < 1$. The activation time constant τ_{act} was set to be $9 - 10$ ms with the deactivation time constant set to $45 - 50$ ms [60], [59],[56].

All steady state walking data and resulting estimates therefrom were split into gait cycles, time-normalized to percent gait cycle (%GC) coordinates, and ensemble averaged for modeling and analysis. Ankle joint angles and muscle contributions to ankle torques were obtained by processing the motion capture data in SIMM [15] (Software for Interactive Musculoskeletal Modeling, MusculoGraphics Inc., Evanston, IL).

The muscle activations, joint angles and joint torques were used to estimate individual muscle force and state profiles in walking, using a muscle-tendon model and a method from [35] as described below.

The dynamics of the primary leg muscle-tendon units contributing to ankle function in normal walking were modeled. The anatomical correlates of the model (shown in Figure 1) include the large muscle-tendon units actuating ankle rotation in the sagittal plane - namely the soleus and gastrocnemius (with medial and lateral heads

represented as one effective muscle) plantar flexors with the Achilles tendon split amongst them, and the tibialis anterior dorsiflexor. All three muscle-tendon units[2] were modeled using (a) Hill-type muscle dynamics [21],[17] and (b) a common non-linear tendon model [38]. Each muscle and tendon were dynamically connected in series at a fixed pennation angle with each other.

Morphological parameters (muscle maximum isometric force, tendon shape factor, reference strain and slack length) defining the model were chosen as those that most efficiently relate the muscle activations and biological joint angles with the biological joint torques [35]:

$$M(\vec{m}, \alpha(t), \theta(t)) \rightarrow [C, \tau(t)] \tag{4.2}$$

where the model M is actuated with muscle activations $\alpha(t)$ and joint angles $\theta(t)$ from the biological gait data, and muscle-tendon parameters $\vec{m}$ are obtained as those that minimize metabolic consumption C, subject to the constraint of matching the output torque $\tau(t)$ to the biological ankle torque. C was computed using empirical measures of muscle metabolic power as a function of contractile element velocity [25],[36]. Bounds on the morphological parameters were chosen to ensure consistency with values reported in the literature [60], [59],[56]. Because of errors starting up the model the cost C was counted starting at 4% of the gait cycle and ran until the end of stance (since the the swing cost was small and relatively flat in the parameter space). The errors starting up the model came from two sources. First, since impact dynamics are highly variable and thus the input data shows increased variability immediately following heel strike, it is difficult to fit the model torque to the experimental average during this phase of gait. Secondly, the model has state (muscle fascicle length and velocity) and since there is no input data before heel strike (the model is only trained on stance) there is a brief interval required for the model to converge to the correct fascicle state. Note that the plantar flexors that are the dominant torque sources in the ankle [42] are inactive during the omitted period. Using the values of

[2]The tibialis anterior was modeled in the same way as the plantar flexors here but replaced with a rotary spring-damper in the prosthesis controller described later.

$\vec{m}$ thus obtained and the inputs $\alpha(t)$ and $\theta(t)$, estimates of muscle force and state profiles were calculated by numerically solving the muscle-tendon model in MATLAB Simulink®[35].

As noted in [35], the resulting model provides empirically inaccessible estimates of individual muscle force. It also results in muscle-tendon morphologies that can be used to predict empirically realistic individual muscle states [35]. Since the morphological features link joint level leg dynamics with neural activations, it is a scheme well suited toward identifying the reflexes that facilitate the interplay of legged dynamics with neural control [35].

Reflexes respond to changes in muscle force and state (relayed by the spindle and golgi tendon sensors in muscles) to contribute to neural stimulation of the muscle and in turn muscle activation [33]. Therefore trends in the muscle force, state, and activation profiles may be used to identify feedback control pathways that contribute to observed state changes. If one ignores the effects of non-reflexive neural drive, a purely feedback-based control structure may derived. In reality feedback does not fully characterize the neural contributions to muscle activation in human gait; for instance central pattern generators (CPG) may also play a role [8], [40]. Nonetheless researchers have suggested that distal muscle-tendon units (such as those spanning the ankle) are likely to be primarily influenced by feedback pathways since they have greater proprioceptive feedback and are more influenced by contact forces [21],[13]. With this in mind we use the observed trends in the estimated muscle variables to motivate a feedback-based control model and evaluate its performance.

Figure 4-2 shows vertically aligned plots of the estimated gastrocnemius muscle activation, force, length, and velocity. It is apparent that there is an early stance period of muscle stretch and low activation, followed by a coincident rise in activation and near-isometric operation in mid-stance. This sequence of events points to a possible contribution from the stretch reflex amongst contributions from other reflex pathways. A notable feature in the mid-stance profiles is the similarity in shapes of force and activation profiles. This positive correlation between force and activation could be facilitated by positive force feedback. The primary characteristic seen in

late stance is that of muscle shortening and a coincident fall in activation. It is possible that the change from isometric operation to concentric operation (shortening) drives the fall in activation via length and velocity feedback pathways. Similar trends were observed in the soleus muscle. From here on we focus on only the soleus and gastrocnemius muscles as these provide the dominant contribution to ankle torque during stance phase in walking[42].

While the analysis above motivates our purely feedback-based control architecture, it does not quantify the mathematical form of the reflexes or the control parameters defining the feedback functions. Here we specify a simple linear feedback structure similar to that used by [21] for both plantar flexor muscles, wherein changes in muscle length, velocity and force are communicated to the spinal cord (with a delay) and are amplified by a gain to collectively generate neural stimulation to the muscle. The stimulation $x(t)$ of an individual muscle is given by

$$\begin{aligned} x(t) = G_F(F(t-\Delta t_F) - F_o)u(F-F_o) \\ +G_l(l(t-\Delta t_{lv}) - l_o)u(l-l_o) \\ +G_v(v(t-\Delta t_{lv}) - v_o)u(|v|-v_o), \end{aligned} \tag{4.3}$$

where G_F, G_l, and G_v are the gains and Δt_F, Δt_l, and Δt_v are the time delays for the force, muscle length, and muscle velocity terms respectively. The functions $u(F-F_o)$, $u(l-l_o)$, and $u(|v|-v_o)$ are unit step functions that ensure the feedback terms are only enabled when the threshold values of F_o, l_o, and v_o (all positive) are exceeded. The time delays represent the path length from muscle to spinal cord and spinal cord back to the neuromuscular junction. Each delay was taken to be 20 ms [22],[49], [34]. The stimulation defined in (3) translates to muscle activation $\alpha(t)$ via the dynamics of cross-bridge formation as specified in equation (1).

The free parameters governing the relation between muscle force and states $F(t)$, $l(t)$, and $v(t)$ and neural stimulation $S(t)$ are the gains G_F, G_l, and G_v and thresholds F_o, l_o, and v_o. Although a static inspection of trends in the muscle activation, force,

and state profiles was used above to motivate the reflex architecture, the unknown parameters were identified with a fitting scheme that included the dynamical muscle-tendon model. This was done so as to account for effects of the Hill-type muscle dynamics and the tendon action in a self-consistent manner. The six parameters were chosen so as to minimize the mean squared error between the feedback-driven activation and the muscle activation estimated from EMG data. The fit was implemented using a genetic algorithm followed by gradient descent in an effort to avoid the numerous local minima that occurred in the mean squared error. The muscle-tendon parameters were taken to be fixed to their optimal values (determined via (2)) while fitting the reflex parameters, with each muscle being treated separately. The enforced bounds for each parameter were determined using the force, length, and velocity profiles given by the muscle-tendon model driven by biological data. Specifically, the reflex gains were allowed to range from zero to a gain that would dominate the net muscle activation, given these nominal force, length, and velocity profiles. The threshold on the length term was allowed to range from the minimum to maximum contractile element length in stance, while the velocity threshold was allowed to vary from zero to the maximum absolute value of velocity observed in stance. The boundaries on the force threshold were chosen to ensure that positive force feedback was engaged sufficiently early to make a large contribution, as expected from [21].

4.2.2 Application to Prosthesis Control

This neuromuscular model was then applied to produce an entirely feedback-based controller for a powered ankle-foot prosthesis. The ankle controller took as input ankle angle, knee angle, and walking state (stance or swing phase) and produced plantar flexor torque based on the neuromuscular models of the soleus and gastrocnemius. The start of the gait cycle in the hardware controller was defined to be consistent with the biological data. Dorsiflexion torque was provided using a unidirectional rotary spring-damper to model the contribution of the tibialis anterior (TA) dorsiflexor. The dorsiflexor choice was made for simplicity and justified by the comparably small amount of torque produced by the dorsiflexors during stance [42], which could ade-

quately be represented by a spring engaged in early stance [41]. Details are described below.

To evaluate the viability of our model for controlling a prosthesis across speed, the model was used to control a prosthetic apparatus comprising a powered ankle-foot prosthesis and an instrumented actuated knee brace worn by an amputee. The ankle and knee joint states of the apparatus were measured and used to provide realtime input to the neuromuscular model simulated by an on-board microcontroller. The resulting torque command from the neuromuscular model was used to produce ankle torque while a knee controller adjusted the torque produced by the knee brace. This configuration, shown in Figure 3, was set up to enable the prosthetic apparatus to behave as if it were a human lower-leg with reflex-controlled muscles acting at the ankle.

4.2.3 Powered Ankle-Foot Prosthesis

As in [17], this study made use of a powered ankle-foot prosthesis (iWalk, LLC, Cambridge, MA [32]) having a size and weight (1.8 kg) similar to the intact biological ankle-foot complex. The prosthesis included a brushless motor, ballscrew transmission, and Kevlar leaf-spring that together comprised a series-elastic actuator (SEA) [43]. The specifications of this drivetrain are listed in Table 1. The SEA was capable of producing torque about the revolute ankle joint, analogous to the torque produced by the plantar flexor and dorsiflexor muscles about the human biological ankle joint. The robotic ankle's theoretical torque capability exceeded 300 Nm. A unidirectional parallel spring engaged when the ankle was dorsiflexed and thereby assisted the SEA during walking [5]. A compliant carbon-fiber leaf-spring attached to the base of the prosthesis acted as a foot.

4.2.4 Knee Clutch

Since the gastrocnemius acts at both the ankle and knee, a spring-clutch was mounted at the knee brace to provide the knee flexion action of the gastrocnemius. The

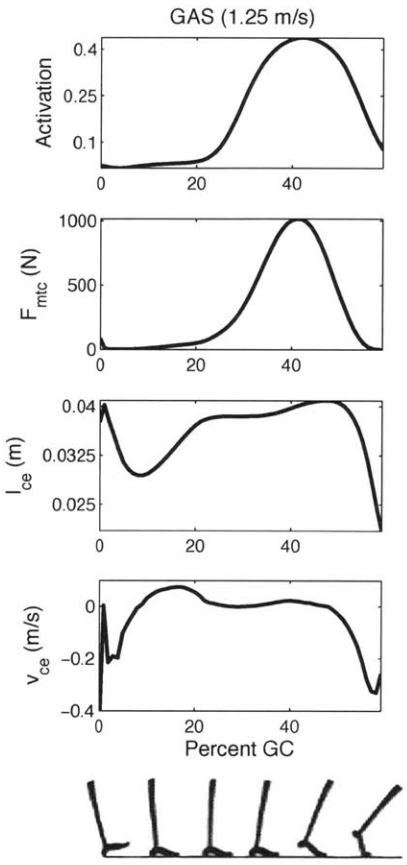

Figure 4-2: Gastrocnemius activation, force, contractile element length, and contractile element velocity estimated by the data-driven muscle-tendon model. Only stance phase is shown, with zero percent gait cycle representing heel strike (as is the case in subsequent figures).

Parameter	Units	Value
Series Spring: Plantar. Torque	Nm/deg	8.38
Series Spring: Dorsi. Torque	Nm/deg	27.23
Parallel Spring	Nm/deg	14.66
Ankle Transmission Ratio	-	175 - 205

Table 4.1: Specifications for the ankle-foot prosthesis. The ankle transmission ratio took its minimum value at maximum (17 degrees) dorsiflexion and maximum value at maximum (24 degrees) plantar flexion. The series spring stiffness is direction dependent. The reported spring constants are nominal values. In practice they vary with angle and applied torque as governed by the geometry of the linkage and series spring design. However, these variations were experimentally evaluated and subsequently calibrated out.

mechanism consisted of a toothed clutch at the free end of a coil spring (spring stiffness of 66,500 N/m) which acted as a knee flexor on a polycentric knee brace. The brace was integrated into a prosthetic socket connected to the ankle-foot prosthesis. When the clutch was engaged via solenoid action, the free end of the spring locked with respect to the socket and the spring stretched as the knee straightened. The force developed by the spring produced a flexion torque at the knee joint. Conversely, when the clutch disengaged no torque was applied at the knee joint. The spring acted on the knee joint with a moment arm that varied between 0.02 m and 0.03 m as a function of knee angle. This moment-arm function was designed so the apparent knee stiffness matched that of the biological knee during level-ground walking [20],[18].

4.2.5 Angle Measurements

The ankle angle and knee angle of the prosthetic apparatus provided the primary control inputs to the neuromuscular model. To measure joint angle, an AM8192B sensor from Renishaw (Gloucestershire, United Kingdom [58]) was used to measure the field angle of a magnet mounted at the joint. Since the foot had some inherent compliance, its deflection during walking contributed to the overall ankle angle. Therefore, the measured ankle torque and estimated forefoot spring constant of 22.72 Nm/deg were used to estimate foot deflection from forefoot loading. This deflection was added to the joint angle measurement for input to the plantar flexors in the neuromuscular model and for data analysis. A potentiometer at the knee provided an estimate of knee joint angle.

Once measured, the ankle and knee angles were passed to lookup tables that estimated the muscle-tendon unit lengths and ankle moment arms of the modeled plantar flexors. These lookup tables were based off of the musculoskeletal geometry of the intact subject, as determined by SIMM. The output muscle-tendon unit lengths and moment arms were then used by the neuromuscular model to compute commanded torque.

4.2.6 Electronics

A Microchip Technology Incorporated PIC32MX575F512H, a single-chip, 32-bit, DSP oriented microcontroller running at 500 Hz was used to run the neuromuscular model in real-time using the angle and torque sensor data from the hardware as input. Sensor and internal states could be sent to a data-collection computer via an onboard IEEE 802.11g wireless radio.

4.2.7 Control

For control purposes, the gait cycle was divided into stance and swing phases. The phases of gait were determined using the state transitions described in [17]. These transitions were triggered using moment estimates from strain gauges embedded in the prosthetic pyramid on the powered ankle-foot prosthesis. During stance phase, the neuromuscular model provided the primary torque command to the ankle. Since in biology the plantar flexor muscles dominate ankle torque during the stance phase of walking [42], neuromuscular models were used to represent them. However since the action of the tibialis anterior and other dorsiflexors resembles that of a linear spring early in the stance phase[41] when the torque contribution of the plantar flexors is small[42], the TA was modeled, for simplicity, as a unidirectional virtual rotary spring-damper of the form:

$$\tau_{TA} = \begin{cases} -(K_P\theta + K_V\dot{\theta}) & K_P\theta + K_V\dot{\theta} > 0 \\ 0 & K_P\theta + K_V\dot{\theta} \leq 0 \end{cases} \tag{4.4}$$

where τ_{TA} is the TA ankle torque contribution, K_P is the spring constant, K_V is the damping constant, θ is the ankle angle and $\dot{\theta}$ is the ankle angular velocity. K_P was fit to best match the ankle torque-angle relation of the intact-limbed subject early in the stance phase (3.04 Nm/deg) and K_V was experimentally set to 0.0524 Nm-s/deg to prevent prosthesis foot oscillations at foot-flat. To prevent the TA from fighting the plantar flexors during late stance, once the magnitude of τ_{TA} dropped to zero during a given stance phase, τ_{TA} was suppressed to zero for the remainder of stance (as in

[17]). During the swing phase, the plantar flexors were turned off by reducing the reflex stimulations to their baseline values and the TA was made to be bidirectional to enable full-control of the ankle joint. The TA impedance was also increased during the swing phase (experimentally tuned to $K_P = 3.84$ Nm/deg, $K_V = 0.122$ Nm-s/deg) for achieving early ground clearance. When well into the swing phase, the impedance of the TA was reset to the stance phase setting in preparation for heel strike. The knee clutch was engaged shortly after maximum knee flexion in stance phase, as the clutch passively locked once under load. Once the knee angle returned to the engagement angle later in stance phase, the clutch released automatically.

4.2.8 Torque Generation and Measurement

Physical torque at the ankle joint was generated by both the motorized drive train and the parallel spring. The ankle angle sensor and known parallel spring stiffness were used to estimate the parallel spring torque contribution and the remaining desired torque was commanded to the motor (Figure 3). The motor current was enforced using closed-loop current control with a custom motor controller comprising an H-bridge driven with Pulse Width Modulation.

The total ankle torque was computed by adding the SEA torque contribution to the parallel spring torque estimate. The SEA torque contribution was estimated using the series spring deflection and the calibrated stiffness of the series spring. The deflection, in turn, was computed by comparing ankle angle to motor angle (measured with an optical shaft encoder). The knee torque was estimated using a linear potentiometer at the coil spring for spring force along with a moment arm function relating linear force to knee torque.

4.2.9 Clinical Experiments

Clinical experiments were approved by MITs Committee on the Use of Humans as Experimental Subjects (COUHES). After giving informed consent, a healthy active bilateral transtibial amputee participant, height and weight matched to the intact-

limbed subject, was fitted with the prosthetic apparatus. The participant donned the actuated prosthetic apparatus on his right leg and wore a conventional passive transtibial ankle-foot prosthesis on his left leg. Following initial walking trials for natural adjustment, the subject was asked to walk at three different speeds (0.75 m/s, 1.0 m/s, and 1.25 m/s) across a 5.3 m long path. For each walking trial, the participant began walking approximately 3 m from the beginning of the pathway and stopped walking approximately 3 m past the end of the path. The beginning and end of the 5.3 m path were labeled with markers on the ground. A stopwatch was used to verify the average walking speed for each trial by noting when the subjects center of mass passed over each of the markers. A total of 39 trials were captured.

4.2.10 Data Processing

Only steady state gait cycles within 10% of the 3 target speeds were used for analysis. All gait cycles were re-sampled to span 1000 points. The net work was calculated for each individual gait cycle by numerically integrating ankle torque over ankle angle from heel strike to toe-off. An ensemble average net work across gait cycles was then calculated for each trial.

4.3 Results

4.3.1 Modeling

The optimized muscle-tendon parameters and fit reflex parameters for the dominant ankle plantar flexors (soleus and gastrocnemius) are shown in Table 2. The reflex parameter fit was seen to converge within tolerance, with the objective function having a negligible slope/curvature ratio for each parameter at the minimum. The fit was conducted 10 times on each muscle starting with differing initial populations in the genetic algorithm with little effect on the final parameters.

Figure 4 shows the fit to soleus activation and the resulting muscle dynamics. The R^2 values for the activation, force, length, and velocity fits were 0.83, 0.92, and 0.95,

Parameter	Units	Min. Val.	Max. Val.	Fit Val.
GAS F_{max}	(N)	1398	6990	1759
GAS l_{slack}	(m)	.282	.460	.399
GAS K_{sh}	-	1	5	2.81
GAS λ_{ref}	-	0.02	0.09	0.042
GAS G_f	(1/N)	0	5e-4	1.45e-4
GAS F_o	(N)	0	203	78.3
GAS G_l	(1/m)	0	10	3.66
GAS l_o	(m)	3.05e-2	4.25e-2	3.09e-2
GAS G_v	(s/m)	0	2	0.167
GAS v_o	(m/s)	0	0.278	2.23e-4
SOL F_{max}	(N)	3650	18251	7142
SOL l_{slack}	(m)	.175	.293	.250
SOL K_{sh}	-	1	5	2.25
SOL λ_{ref}	-	0.02	0.09	0.083
SOL G_f	(1/N)	0	1e-4	2.62e-5
SOL F_o	(N)	0	543	10.5
SOL G_l	(1/m)	0	10	2.44
SOL l_o	(m)	0.015	2.87e-2	1.75e-2
SOL G_v	(s/m)	0	2	5.65e-2
SOL v_o	(m/s)	0	0.196	1.29e-3

Table 4.2: Boundaries and fit values for plantar flexor muscle-tendon and reflex parameters. The muscle-tendon parameters were determined as described in [35] and fixed during reflex parameter fitting.

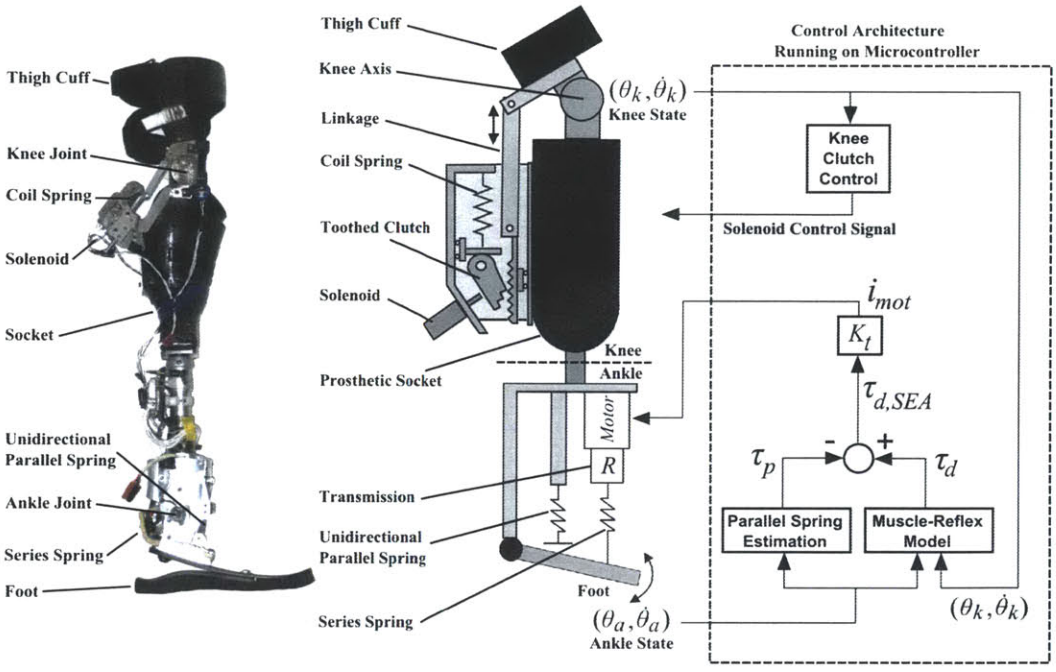

Figure 4-3: Labeled photograph of the prosthetic apparatus and associated labeled schematic and control architecture. The rotary elements in the ankle-foot prosthesis are shown as linear equivalents in the model schematic for clarity. In the control schematic the parallel spring contribution to prosthesis ankle torque, τ_p, was subtracted from the desired ankle torque command from the neuromuscular model, τ_d, to obtain the desired SEA torque $\tau_{d,SEA}$. A motor current command i_{mot} was obtained by multiplying by the motor torque-constant K_t and produced using a custom motor controller (not shown). The knee clutch was engaged via the solenoid depending on knee state as obtained from the knee potentiometer.

respectively. The R^2 values for these fits in the gastrocnemius were 0.90, 0.94, and 0.94 respectively. The figure also shows the contributions of the different reflexes to follow the sequence described above. It was found that the positive force feedback term dominated the fit but was reliant on the length feedback term to time and scale its buildup. These contributions were roughly maintained when the neuromuscular model was applied to biological ankle angles at different walking speeds, as evidenced by Figure 5. Very similar profiles and relative reflex contributions were seen in both plantar flexors.

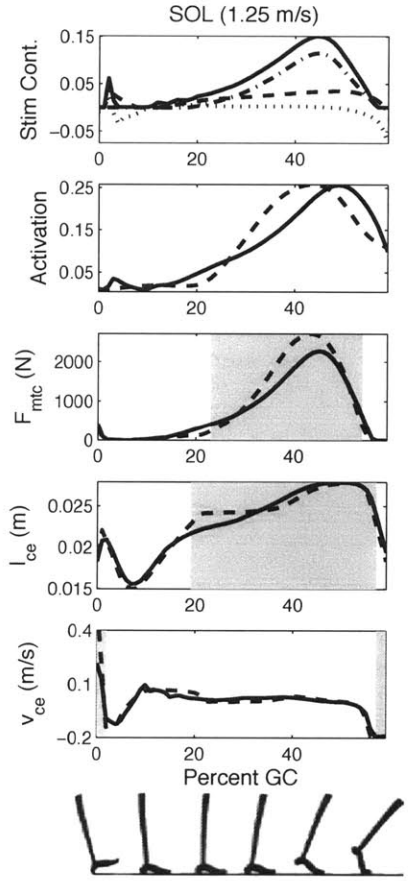

Figure 4-4: Comparison of the soleus muscle dynamics produced by EMG vs. those produced by reflex feedback to the muscle-tendon model. The top plot shows the contributions from the force, length, and velocity terms to the stimulation. Here the stimulation is the solid line, the force term is the dashed-dot line (largest contributor), the length is the dashed line, and the velocity term (which goes negative) is the dotted line. On the rest of the plots the dashed curves are the model outputs given EMG-based activation, while the solid curves are the corresponding variables when the model activation is determined by the reflex structure in (3). The shaded regions indicate the times where the force, length, and velocity feedback terms contribute at least 0.01 to the stimulation. All plots used biological angles for walking trials at 1.25 m/s.

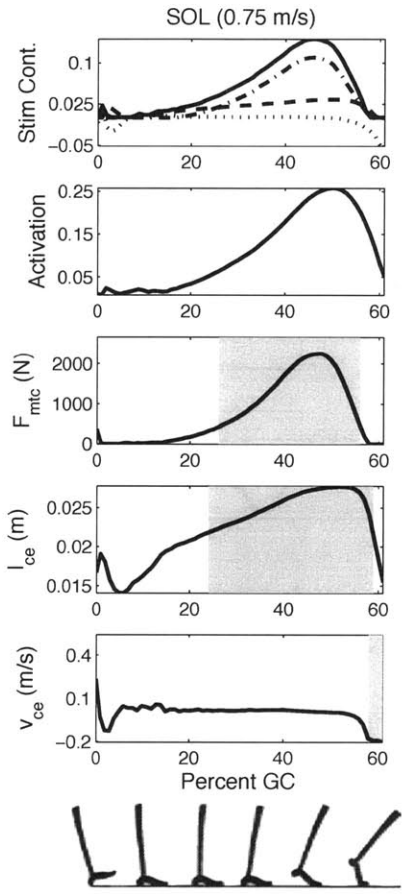

Figure 4-5: Plot of soleus muscle dynamics produced by the reflex-based stimulation (Eq. 3) for input ankle angles from walking trials at 0.75 m/s. The top plot shows the contributions to the stimulation (solid line) from the force (dashed-dot line), length (dashed line), and velocity terms (dotted line). The remaining plots (from top to bottom) show the total activation, muscle force, contractile element length, and contractile element velocity. The shaded regions indicate the times where the force, length, and velocity feedback terms contribute at least 0.01 to the stimulation.

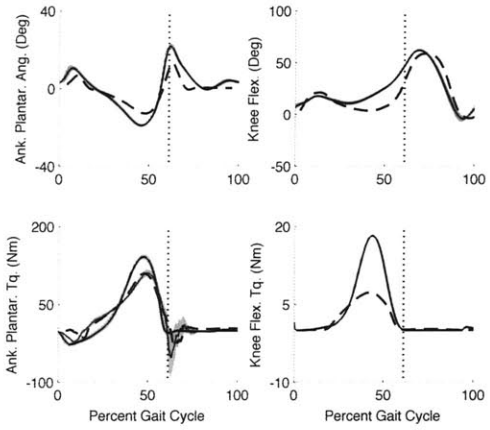

Figure 4-6: Comparison of prosthesis ankle and knee angles and torques during the clinical trials (measured) with those from a height and weight matched subject with intact limbs (biological). Torque that plantar flexes the ankle is defined to be positive and moves the angle in the positive direction. Similarly torque that flexes the knee is positive and increases the knee angle. The biological values are the thick solid lines (with shaded errors) in each plot while the dashed lines are the values measured on the prosthesis. In the ankle torque plot the commanded torque is shown as a thinner solid line, again with shaded error bars. The knee torque plot compares the torque provided by the clutch-spring mechanism to that provided by the natural gastrocnemius in simulation. The vertical line indicates toe off in each plot.

4.3.2 Clinical Trials

The results of the clinical trials are summarized in Figures 6, 7, and 8. Figure 6 shows the mean angle and torque profiles for the ankle-foot prosthesis and knee joint during the 1.25 m/s clinical walking trials. The biological gastrocnemius component of knee torque was estimated for this plot by feeding joint kinematics and EMG from the intact-limbed subject into the model from [35]. The resulting gastrocnemius force was multiplied by the moment arm of this muscle as estimated with SIMM. There is a qualitative agreement in angle and torque profiles between the prosthesis apparatus and those of the intact-limbed subject. However, the ankle angle of the prosthetic apparatus deflected less than the intact biological ankle, resulting in smaller peak torque. The torque produced by the knee clutch was also seen to be smaller than the biological counterpart, implying that the spring in the knee clutch mechanism was too soft.

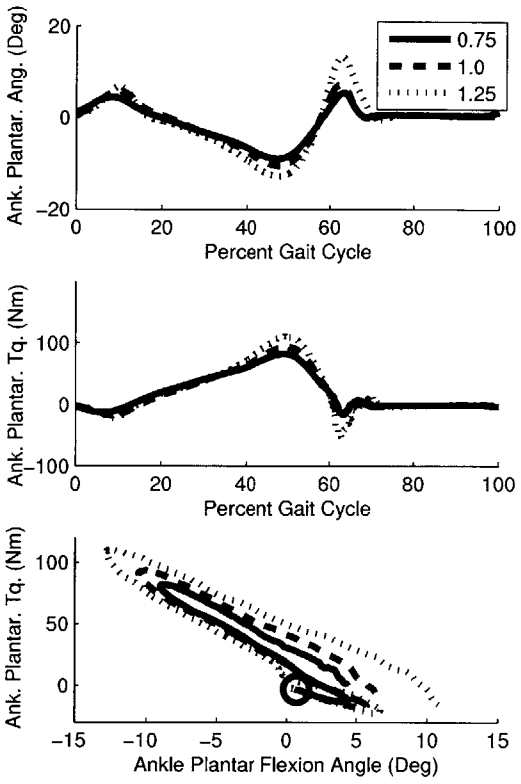

Figure 4-7: Commanded ankle angles, torques, and workloops for three speeds in clinical walking trials. Shown are data for three speeds: 0.75 m/s (solid line), 1.0 m/s (dashed line), and 1.25 m/s (dotted line). In the torque vs. angle plot heel strike is indicated with by a circle.

The ankle-foot prosthesis angle and commanded torque for the three target walking speeds are plotted in Figure 7. The magnitudes of both peak angular deflection and peak torque are seen to increase with walking speed, with both variables aligning in percent gait cycle across speed. The third pane in Figure 7 shows an increase in commanded positive ankle work across speed, a trend that is also observed in intact-limbed individuals [41]. As can be seen from Figure 8, this trend is also reflected in the measured net ankle work.

4.4 Discussion

The reflex-based controller developed in this study produced a trend of increasing net work with walking speed during clinical trials. Looking at the kinematics and

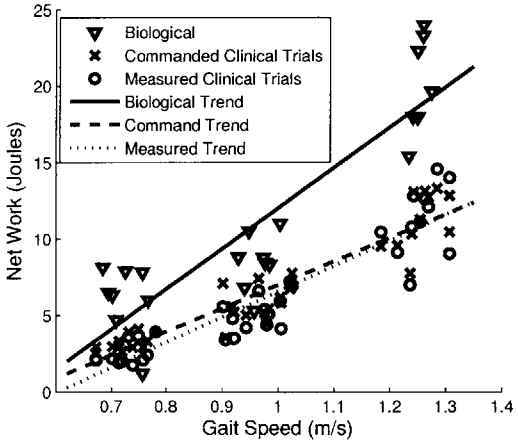

Figure 4-8: Energy output of the ankle across gait speed. Shown are biological data, net work as commanded by the ankle-foot prosthesis during clinical trials, and measured net work during the clinical trials.

dynamics of the prosthetic ankle joint (Figure 7), this trend can be attributed to at least two effects. First, both the peak ankle angle and peak torque increase at faster walking speeds. The angle increase is produced by a combination of kinematic and dynamic changes associated with higher walking speeds, such as increased stride length and higher dynamic loading of the ankle joint. Although the angle and torque are interrelated through the dynamics of the amputee subject, an increase in angle tends to produce correspondingly higher torques[3]. The angle and torque remain aligned in the gait cycle across speed, so increasing both peak values results in a larger work loop and hence more positive net work. The second effect producing the trend in net work is the increased ankle plantar flexion in terminal stance at faster walking speeds. When combined with a torque profile that increases with increasing speed, this further contributes to the trend in net work.

Although the subject is able to influence the ankle behavior by changing walking speed, tracking a desired angle trajectory at will is not possible. The subject is not an infinite impedance position source and is thus reliant on the controller to produce torques that, when interacting with the human dynamics, produce reasonable

[3]This observation was verified in simulation by scaling the biological ankle angle trajectory in magnitude and observing an increased peak torque from the model.

angles. The observed trend in net work therefore implies that the controller is able to effectively modulate ankle joint quasi-static impedance (slope of joint torque vs. state) across speed.

The behavior of the controller can be further understood through simulations that provide the neuromuscular model with biological ankle angles at different speeds. This is possible because the muscle states seen in the controller during clinical trials (with angle input from the prosthesis) are qualitatively similar to those obtained from simulations (with angle input from the intact-limbed subject). It was evident in both simulations and clinical tests that the stimulation profiles provided to the muscles vary little with speed when normalized to percent gait cycle (Figures 4 and 5). This similarity is a result of the consistent timing of the force, length, and velocity reflex contributions throughout stance. The sequence is preserved across speed by the length feedback term, which governs the timing and magnitude of force buildup. The importance of timing is consistent with the findings of Winter [55], who suggested that walking speed is governed by gains and maintains its timing as a result of afferent feedback.

One may compare the results of our study to those of previous works. The positive force feedback term that dominates force production in our model was based on the studies of [44] and [21]. The length term in (3) represents the stretch reflex while the velocity term represents negative feedback controlling the rate of muscle contraction. If the muscle is lengthening too rapidly the velocity term will increase the activation; if it is shortening too quickly the velocity term will reduce activation. Several empirical studies [46], [23], [24], [1], [12], [2] have demonstrated the presence of afferent feedback in the plantar flexors during stance. These studies record the changes in muscle EMG signals when the gait of a subject is perturbed either by changing the inclination of the walking surface or by forcing muscle-tendon length changes using an orthosis. Notably Klint et al. [2] isolated the contributions of force-based and length-based afferent feedback during different intervals of stance at self-selected walking speed. They found that force feedback was dominant in late stance but contributed little during midstance perturbations, where spindle-based feedback likely dominates. This

sequence is similar to that seen in our plantar flexor reflexes, although our modeling was done without perturbations. One further study that would specifically address the role of reflexes in speed adaptation would be a direct comparison of plantar flexor EMG signals during walking at different speeds between a normal and a deafferented subject. If reflexes are dominant in speed adaptation, as postulated in this study, one should see a sluggishness in the adaptation to different speeds of the deafferented subject.

This study extends the work in [17] by considering the structural morphology of the ankle plantar flexors and including length and velocity feedback terms. Speed adaptation is enabled through these changes. It appears that inclusion of the stretch reflex in both plantar flexors was critical for timing and scaling force buildup, thereby enabling an increase in positive net work across speed.

Despite the speed adaptation exhibited by our approach, some limitations are evident. First, the chosen reflex structure does not necessarily reflect the true biological control scheme. The ability to reproduce this scheme would rely on knowledge of the non-reflexive neural drive provided to muscles as well as the true structure of the reflexive feedback. Despite the absence of this knowledge, our scheme provides functional results. A second limitation of our approach was the simple impedance approximation used for the ankle dorsiflexor model. This approximation reduced the quality of the ankle torque fit in early stance; the fit may be improved by including a dorsiflexor muscle model similar to those used for the plantar flexors.

Despite these limitations, this work may serve as a starting point for several natural extensions. Different reflex structures may be explored and the effect of non-reflexive neural drive examined. The interaction of the neuromuscular model with mechanical effects (human dynamics, ground contact forces, etc.) may be better understood by conducting a forward dynamic simulation similar to that in [21]. Our overall approach may be extended to include muscles further up the leg, possibly leading to speed adaptive control schemes for multiple prosthetic joints. Finally, the generality of the approach could be tested by studying the behavior of the reflex-based controller when applied to tasks other than level ground walking. In the design of

adaptive prosthetic limbs, we believe the application of neuromechanical principles are of critical importance.

Chapter 5

Conclusions and Future Work

5.1 Conclusions

This thesis included both scientific and technical aspects. On the science side, an inverse computational framework was established for investigating the interplay between neural control and muscle-tendon structure during walking. The framework was composed of two pieces; (i) a hidden state estimation of muscle activation using EMG data and (ii) an optimization-based system identification procedure for determining muscle-tendon morphology. The approach was used to predict muscle force and state, resolving the contributions of individual muscles to total joint torques during walking. It was able to more accurately predict metabolic consumption than conventional models while providing qualitative agreement with available ultrasound measures of muscle fascicle length. Many other predictions that are not currently testable can be derived from the model including muscle and tendon power profiles, metabolic consumptions of individual muscles, and reflex structures. We hope that future empirical techniques will be able to further validate the predictions of the model.

On the technical side, a controller based on the model was developed for a robotic ankle-foot prosthesis. The controller coupled the optimal muscle-tendon morphology found by the previous steps to a reflexive feedback-based control scheme to enable application to the device. Speed adaptive behavior was observed in clinical trials, sup-

porting the notion that control schemes based on neuromuscular models can produce biomimetic behavior when applied to prosthetic limbs.

5.2 Scientific Extensions

There are several directions that future modeling studies based on this work may pursue. Among them are the following:

Model Refinement with Wire EMG, Additional Muscles In this study we found that the predictive power of our modeling approach was limited by the quality of the EMG recordings taken. This was particularly problematic in the muscles spanning the hip, and prevented validation of the model across speed. One could likely improve the results of the model and broaden its applicability by obtaining fine wire EMG measurements of the problematic muscles. Signals collected from fine wire are known to be cleaner and less prone to artifacts than their surface counterparts, but require more invasive measurements. One could also improve upon the model by including more muscles of the leg; this would avoid some potentially compromising muscle lumpings and lead to a more complete picture of the roles of various muscles during walking.

Forward Dynamic Modeling with Reflexes One way to test the adaptability of this approach without relying upon EMG measurements is through forward dynamic modeling. As discussed in Section 1.1.2, forward-dynamic models driven by only reflexive feedback have been shown to walk stably across different terrains [21] and at different speeds[47] (through reflex parameter tuning) . These models may be improved through data-driven customization for individual subjects and the inclusion of more realistic muscle-tendon geometries and morphologies. Our current work involves scaling the model of [21] (see Figure 6-1) to align with the data-based SIMM estimates of segment inertias and muscle lines of action for individual participants. Using this model, we can re-optimize the muscle-tendon morphologies and

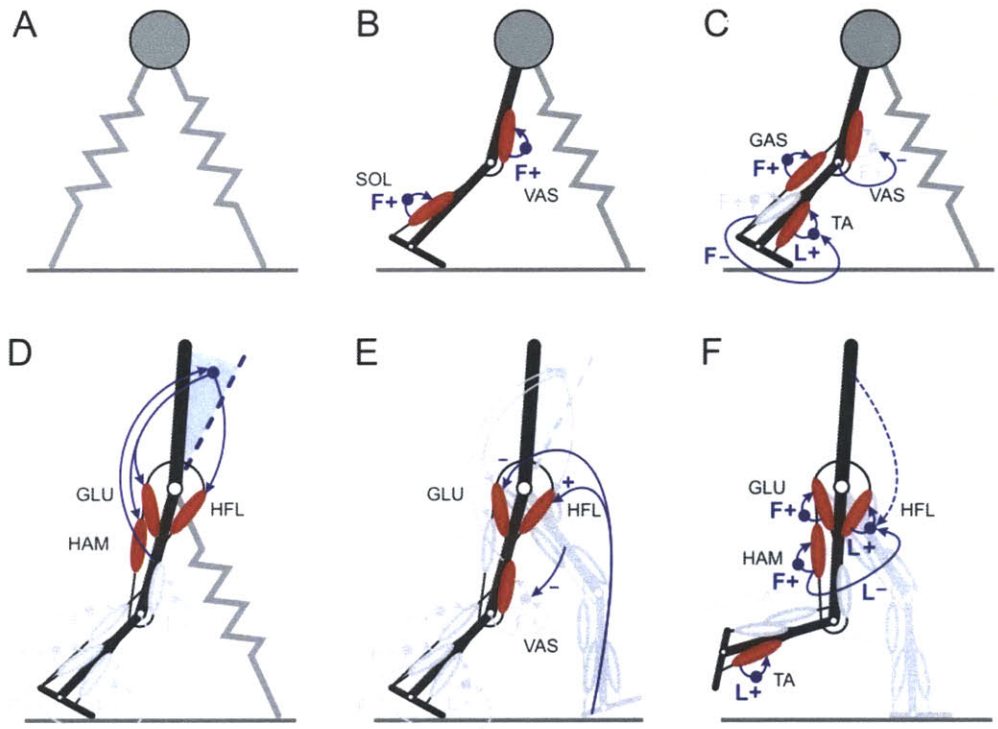

Figure 5-1: Reflex-based forward dynamic walking model. Figure credit: Geyer-Herr 2010 [21].

check agreement with the inverse analysis presented in this thesis. We can also investigate potential contributions from additional reflexes; for instance the stretch reflex implemented in [37] may be useful. We would hope to improve upon the metabolic estimates of [21] as well as to observe more terrain and speed adaptive behavior with this approach.

Three Dimensional Modeling One other obvious extension of this model is to three dimensions. All considerations in this thesis and in the Geyer-Herr forward dynamic model are for the sagittal plane, but walking is a three dimensional activity. The hip in particular is built for other degrees of freedom; our inverse model may be improved by trying to match hip kinetics for motion in the coronal (left-right) plane. One could also imagine improving upon the two-dimensional, forward dynamic representation of [21] by building a representation of the full, three-dimensional SIMM model in MATLAB Simulink. This would allow for a more realistic optimization of

muscle-tendon morphology and reflex loops as well as the investigation of behaviors other than straight line walking. One could imagine using such a three dimensional model to investigate interactions between a human and an external device such as a prosthesis, orthosis, or exoskeleton.

Application to Running One final potential scientific extension of this model is to running. The muscle-tendon morphology identified by our procedure reflects physical characteristics of the system, so it should be applicable to activities beyond walking. It would be interesting to compare our results to a similar kinematically-clamped optimization for running at a self-selected speed, particularly with a highly trained runner. The hypothesis in the latter case would be that the runner has, through training, tuned their muscle-tendon morphology to maximize their efficiency at that pace. Seeing how the two parameter sets are related would lend insight into both the similarity of the structural requirements of the tasks (walking and running) and the efficacy of the hypotheses. One could also imagine building a forward dynamic model of running, again based on reflexive feedback. In this case one would be primarily interested in the neural adaptations required to run at different speeds.

5.3 Technological Extensions

Many technological extensions of this work are also possible. The application described in this thesis may be thought of as a special, basic case of the general control paradigm shown in Figure 6-2. In the general case a neuromuscular model is used to control a biomimetic robotic leg using inputs from both intrinsic (from sensors on the device) and extrinsic (from sensors outside the device) sources. In Chapter 4 we only used intrinsic sensing and only controlled a robotic ankle-foot prosthesis, but one could imagine adding other sensors to modulate the reflexive feedback and/or using the system for coordinated control of more than one joint. Examples of potential extrinsic sensors include surface EMG electrodes on the residual limb or mounted inertial measurement units (IMUs). In particular this approach would provide a means

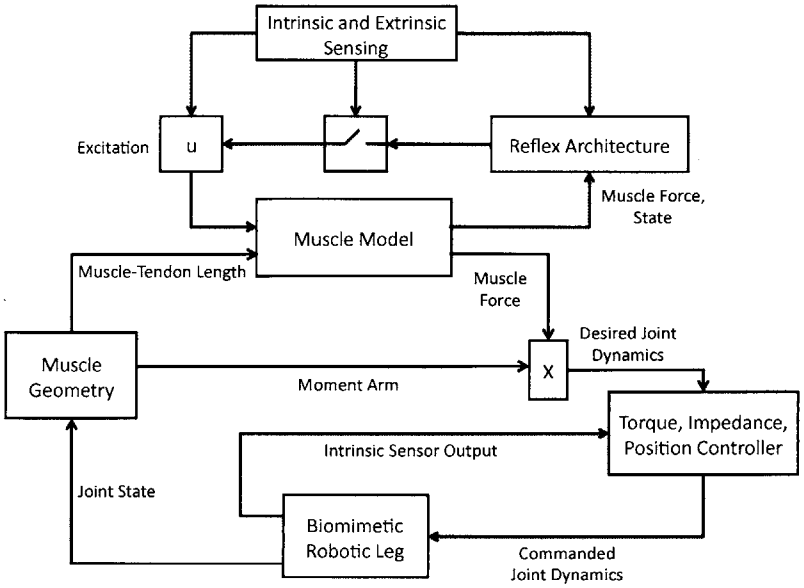

Figure 5-2: Full control paradigm for a biomimetic prosthetic leg controlled by a neuromuscular model.

to control a robotic ankle and knee together, possibly producing adaptive behavior. The paradigm could also be applied to control orthoses or exoskeletons, hopefully leading to an improvement in the performance of such assistive devices.

5.4 Summary

We have described a method for investigating the interaction between neural control and muscle-tendon structure during walking and its application to a prosthesis control problem. We believe that further work in this area will greatly increase our understanding of human locomotion and our ability to produce life-like prosthetic limbs.

Appendix A

Addressing Missing EMG Data

As mentioned in Chapter 2, full EMG data sets were difficult to obtain. This was largely due to the inherent difficulty of collecting surface EMG signals in the muscles spanning the hip. In this area the muscle geometry is more complex than the more distal regions and the muscles are buried deeper beneath the skin than the more distal muscles. The hip area is also less easy to access and more prone to motion artifacts, increasing the probability of poor measurements.

In tables A.1 and A.2 we show, respectively, the characteristics of all participants for whom EMG signals were recorded and the muscles for which reasonable profiles were obtained. Using all muscles with reasonable EMG trajectories across subjects, we formed average neural excitation and activation profiles for each muscle. These profiles are displayed in Figures 3-7 and 3-8. When performing the system identification optimization in Chapter 3 for a given subject, each unreasonable activation profile was replaced by the average activation profile for that muscle. As can be seed from Table A.2 this was a relatively rare occurrence for the muscles spanning the ankle and knee but was frequently required at the hip. This lack of quality data was the motivation behind the substitution of excitation profiles from [42] for the muscles of the hip in the analysis at the end of Chapter 3.

To justify this procedure we performed a Leave One Out Cross Validation (LOOCV) analysis on the reasonable excitation and activation trajectories for each muscle. We computed the Pearson r coefficient between each individual profile and the average of

Subject	Age	Mass	Leg Length	Ethnicity	Sport	Min. MCOT
AD	24	63.9 kg	0.927 m	Caucasian	Running	1.40 m/s
AM	22	66.3 kg	0.923 m	Polish/Chinese	Bicycling	1.50 m/s
EM	27	78.8 kg	0.944 m	Caucasian	Football	1.20 m/s
DS	24	80.2 kg	0.980 m	African	Soccer	1.00 m/s
DH	24	80.3 kg	0.953 m	African	Basketball	1.32 m/s
MC	24	72.3 kg	0.927 m	Caucasian	Running	1.49 m/s
JB	29	68.9 kg	0.933 m	Caucasian	Running	1.31 m/s
BC	26	65.0 kg	0.902 m	Caucasian	Running	1.38 m/s
DC	25	65.4 kg	1.028 m	Caucasian	Running	1.47 m/s

Table A.1: Relevant characteristics of all participants from whom EMG data were recorded. Note that Min. MCOT Speed was only estimated from metabolic data for subjects DH, MC, JB, BC, and DC. It was estimated using subject preference for participants AD, AM, EM, and DS.

Subject	Reasonable EMG Profiles
AD	TA, SOL, GAS, VAS, BFSH, RF, HAM, ILL, GMAX
AM	TA, SOL, GAS, VAS, BFSH, RF, HAM, ILL, GMAX
EM	TA, SOL, GAS, VAS, BFSH, RF, HAM, GMAX, GMED
DS	TA, SOL, GAS, VAS, BFSH, RF, HAM, GMAX
DH	SOL, GAS, VAS, BFSH, RF, HAM, ILL, GMAX, GMED, ADDL, ADDM
MC	TA, SOL, GAS, VAS, HAM, ILL, GMED
JB	TA, SOL, GAS, VAS, BFSH, HAM, ILL, GMED
BC	TA, GAS, VAS, BFSH, RF, HAM, GMED, ADDM
DC	TA, SOL, GAS, VAS, BFSH, RF, HAM, GMAX, GMED

Table A.2: Muscles with reasonable EMG profiles for each subject. Note that GMED, ADDL, and ADDM were not collected on AD, AM, EM, or DS.

the remaining reasonable profiles. The average value of these r coefficients for each muscle is shown in Table A.3. The values are, as expected, better for the more distal muscles and those where there is only one typical behavior. The muscles spanning the hip do not perform as well, except for GMED. The measured EMG signals for the adductors (ADDL, ADDM) were not deemed worthy to include in the analysis, as noted in Chapter 2. Average trajectories for all other muscles were used as needed. Some r values for included average profiles were small, but likely did not impact the analysis significantly because these activation signals were typically small in magnitude.

Muscle	Mean Excitation LOOCV r Value	Mean Activation LOOCV r Value
TA	[0.74 0.76 0.82 0.80 0.78 0.76]	[0.76 0.79 0.85 0.82 0.80 0.77]
SOL	[0.96 0.97 0.97 0.96 0.95 0.91]	[0.97 0.98 0.98 0.98 0.97 0.94]
GAS	[0.93 0.93 0.92 0.93 0.92 0.92]	[0.95 0.95 0.95 0.95 0.95 0.94]
VAS	[0.79 0.91 0.92 0.91 0.92 0.94]	[0.80 0.93 0.94 0.93 0.94 0.95]
BFSH	[0.52 0.58 0.59 0.72 0.75 0.81]	[0.55 0.64 0.64 0.77 0.81 0.86]
RF	[0.49 0.50 0.44 0.36 0.39 0.42]	[0.52 0.55 0.47 0.37 0.37 0.39]
HAM	[0.83 0.85 0.79 0.76 0.76 0.76]	[0.86 0.89 0.84 0.80 0.82 0.83]
ILL	[0.46 0.57 0.14 0.58 0.41 0.27]	[0.51 0.65 0.14 0.66 0.54 0.33]
GMAX	[0.45 0.57 0.74 0.70 0.73 0.60]	[0.45 0.61 0.79 0.6 0.79 0.65]
GMED	[0.81 0.73 0.59 0.62 0.61 0.62]	[0.84 0.75 0.60 0.67 0.66 0.64]
ADDL	N/A	N/A
ADDM	[-0.24 0.05 0.37 0.33 0.39 0.29]	[-0.31 0.01 0.36 0.37 0.37 0.33]

Table A.3: r values for LOOCV. The six values in each array refer to walking at 0.75 m/s, 1.00 m/s, 1.25 m/s, 1.50 m/s, 1.75 m/s, and 2.00 m/s, respectively. No values were computed for ADDL because there was only one set of reasonable measurements of that muscle.

Bibliography

[1] Richard af Klint, Jens Bo Nielsen, Jonathan Cole, Thomas Sinkjaer, and Michael J Grey. Within-step modulation of leg muscle activity by afferent feedback in human walking. *The Journal of physiology*, 586(Pt 19):4643–8, October 2008.

[2] Richard Af Klint, Jens Bo Nielsen, Thomas Sinkjaer, and Michael J Grey. Sudden drop in ground support produces force-related unload response in human overground walking. *Journal of neurophysiology*, 101(4):1705–12, April 2009.

[3] Frank C. Anderson and Marcus G. Pandy. Dynamic Optimization of Human Walking. *Journal of Biomechanical Engineering*, 123(5):381, 2001.

[4] Edith M Arnold, Samuel R Hamner, Ajay Seth, Matthew Millard, and Scott L Delp. How muscle fiber lengths and velocities affect muscle force generation as humans walk and run at different speeds. *The Journal of experimental biology*, pages 2150–2160, March 2013.

[5] Samuel K Au, Hugh Herr, Jeff Weber, and Ernesto C Martinez-Villalpando. Powered ankle-foot prosthesis for the improvement of amputee ambulation. *Conference proceedings : ... Annual International Conference of the IEEE Engineering in Medicine and Biology Society. IEEE Engineering in Medicine and Biology Society. Conference*, 2007:3020–6, January 2007.

[6] S.K. Au, J. Weber, and H. Herr. Powered Ankle–Foot Prosthesis Improves Walking Metabolic Economy. *IEEE Transactions on Robotics*, 25(1):51–66, February 2009.

[7] J M Brockway. Derivation of formulae used to calculate energy expenditure in man. *Human nutrition. Clinical nutrition*, 41(6):463–71, November 1987.

[8] T G Brown. On the nature of the fundamental activity of the nervous centres; together with an analysis of the conditioning of rhythmic activity in progression, and a theory of the evolution of function in the nervous system. *Journal of Physiology*, 48(1):18–46, 1914.

[9] Gary S. Chleboun. Fascicle Length Change of the Human Tibialis Anterior and Vastus Lateralis During Walking. *Journal of Orthopaedic and Sports Physical Therapy*, 37(7):372–379, July 2007.

[10] E.A. Clancy, E.L. Morin, and R. Merletti. Sampling, noise-reduction and amplitude estimation issues in surface electromyography. *Journal of Electromyography and Kinesiology*, 12(1):1–16, 2002.

[11] Steven H Collins, Martijn Wisse, and Andy Ruina. A Three-Dimensional Walking Robot with Two Legs and Knees. *The International Journal of Robotics Research*, 20(7):607–615, 2001.

[12] Neil J Cronin, Masaki Ishikawa, Michael J Grey, Richard af Klint, Paavo V Komi, Janne Avela, Thomas Sinkjaer, and Michael Voigt. Mechanical and neural stretch responses of the human soleus muscle at different walking speeds. *The Journal of physiology*, 587(Pt 13):3375–82, July 2009.

[13] M A Daley, G Felix, and A A Biewener. Running stability is enhanced by a proximo-distal gradient in joint neuromechanical control. *The Journal of Experimental Biology*, 210:383–394, 2007.

[14] Kalyanmoy Deb. *Multi-Objective Optimization Using Evolutionary Algorithms.* John Wiley & Sons, Hoboken, NJ 07030-5774, 2001.

[15] Scott L Delp and J Peter Loan. A Graphics-Based Software System to Develop and Analyze Models of Musculoskeletal Structures. *Computers in Biology and Medicine*, 25(1):21–34, 1995.

[16] M F Eilenberg. A neuromuscular-model based control strategy for powered ankle-foot prostheses. Master's thesis, Massachusetts Institute of Technology, Cambridge, MA, 2009.

[17] Michael F Eilenberg, Hartmut Geyer, and Hugh Herr. Control of a powered ankle-foot prosthesis based on a neuromuscular model. *IEEE transactions on neural systems and rehabilitation engineering : a publication of the IEEE Engineering in Medicine and Biology Society*, 18(2):164–73, April 2010.

[18] Ken Endo. *A Model of Muscle-Tendon Function in Human Walking.* PhD thesis, Massachusetts Institute of Technology, Cambridge, MA, 2012.

[19] Ken Endo, Daniel Paluska, and Hugh Herr. A quasi-passive model of human leg function in level-ground walking. *2006 IEEE/RSJ International Conference on Intelligent Robots and Systems*, pages 4935–4939, October 2006.

[20] Ken Endo, Eric Swart, and Hugh Herr. An artificial gastrocnemius for a transtibial prosthesis. *Conference proceedings : ... Annual International Conference of the IEEE Engineering in Medicine and Biology Society. IEEE Engineering in Medicine and Biology Society. Conference*, 2009:5034–7, January 2009.

[21] Hartmut Geyer and Hugh Herr. A muscle-reflex model that encodes principles of legged mechanics produces human walking dynamics and muscle activities. *IEEE transactions on neural systems and rehabilitation engineering : a publication of the IEEE Engineering in Medicine and Biology Society*, 18(3):263–73, June 2010.

[22] Hartmut Geyer, Andre Seyfarth, and Reinhard Blickhan. Positive force feedback in bouncing gaits? *Proceedings. Biological sciences / The Royal Society*, 270(1529):2173–83, October 2003.

[23] M J Grey, M Ladouceur, J B Andersen, J B Nielsen, and T Sinkjaer. Group II muscle afferents probably contribute to the medium latency soleus stretch reflex during walking in humans. *The Journal of physiology*, 534(Pt 3):925–33, August 2001.

[24] Michael J Grey, Jens Bo Nielsen, Nazarena Mazzaro, and Thomas Sinkjaer. Positive force feedback in human walking. *The Journal of physiology*, 581(Pt 1):99–105, May 2007.

[25] A. V. Hill. The Heat of Shortening and the Dynamic Constants of Muscle. *Proceedings of the Royal Society of London. Series B, Biological Sciences*, 126(843):136–195, 1938.

[26] A. V. Hill. The efficiency of mechanical power development during muscular shortening and its relation to load. *Proceedings of the Royal Society of London. Series B, Biological Sciences*, 159(975), 1964.

[27] J K Hitt, T G Sugar, M Holgate, and R Bellman. An active foot-ankle prosthesis with biomechanical energy regeneration. *J. Med Devices*, 4(1), 2010.

[28] Neville Hogan and Robert W. Mann. Myoelectric Signal Processing : Optimal Estimation Applied to Electromyography- Part I: Derivation of the Optimal Myoprocessor. *IEEE Transactions on Biomedical Engineering*, 27(7):382–395, 1980.

[29] Neville Hogan and Robert W. Mann. Myoelectric Signal Processing : Optimal Estimation Applied to Electromyography- Part II : Experimental Demonstration of Optimal Myoprocessor Performance. *IEEE Transactions on Biomedical Engineering*, 27(7):396–410, 1980.

[30] M A Holgate, A W Bohler, and T G Sugar. Control algorithms for ankle robots: A reflection on the state of the art and presentation of two novel algorithms. *Proc. of the 2nd Biennial IEEE/RAS-EMBS Intl Conf on Biomed Robots and Biomechatronics, Scottsdale, AZ*, pages 97–102, 2008.

[31] Masaki Ishikawa, Paavo V Komi, Michael J Grey, Vesa Lepola, and Gert-Peter Bruggemann. Muscle-tendon interaction and elastic energy usage in human walking. *Journal of applied physiology (Bethesda, Md. : 1985)*, 99(2):603–8, August 2005.

[32] iWalk: http://www.iwalkpro.com.

[33] Eric R Kandel, James H Schwartz, and Thomas M Jessell. *Principles of Neural Science*. McGraw-Hill, New York, NY, fourth edition, 2000.

[34] M Knikou and W Z Rymer. Effects of changes in hip joint angle on h-reflex excitability in humans. *Exp. Brain Res.*, 143:149–159, 2002.

[35] Pavitra Krishnaswamy, Emery N Brown, and Hugh M Herr. Human leg model predicts ankle muscle-tendon morphology, state, roles and energetics in walking. *PLoS computational biology*, 7(3):e1001107, March 2011.

[36] Shiping Ma and George I. Zahalak. A Distribution-Moment Model of Energetics in Skeletal Muscle. *J. Biomechanics*, 24(1):21–35, 1991.

[37] Jared Markowitz, Pavitra Krishnaswamy, Michael F Eilenberg, Ken Endo, Chris Barnhart, and Hugh Herr. Speed adaptation in a powered transtibial prosthesis controlled with a neuromuscular model. *Philosophical transactions of the Royal Society of London. Series B, Biological sciences*, 366(1570):1621–31, May 2011.

[38] T A McMahon. *Muscles, reflexes, and locomotion.* Princeton University Press, Princeton, NJ, 1984.

[39] Richard R Neptune, Kotaro Sasaki, and Steven a Kautz. The effect of walking speed on muscle function and mechanical energetics. *Gait & posture*, 28(1):135–43, July 2008.

[40] G Orlovsky, T Deliagina, and S Grillner. *Neuronal control of locomotion: from mollusc to man.* Oxford University Press, New York, NY, 1999.

[41] M L Palmer. Sagittal plane characterization of normal human ankle function across a range of walking gait speeds. Master's thesis, Massachusetts Institute of Technology, Cambridge, MA, 2002.

[42] Jacquelin Perry. *Gait Analysis.* SLACK Incorporated, Thorofare, NJ 08086-9447, first edition, 1992.

[43] J Pratt, B Krupp, and C Morse. Series elastic actuators for high fidelity force control. *Industrial Robot: An International Journal*, 29(3):234–241, 2002.

[44] A Prochazka, D Gillard, and D J Bennett. Positive force feedback control of muscles. *J Neurophsiol*, 77:3226–3236, 1997.

[45] Terence D Sanger. Bayesian filtering of myoelectric signals. *Journal of neurophysiology*, 97(2):1839–45, February 2007.

[46] T Sinkjaer, J B Andersen, M Ladouceur, L O Christensen, and J B Nielsen. Major role for sensory feedback in soleus EMG activity in the stance phase of walking in man. *The Journal of physiology*, 523 Pt 3:817–27, March 2000.

[47] Seungmoon Song and Hartmut Geyer. Regulating speed and generating large speed transitions in a neuromuscular human walking model. *2012 IEEE International Conference on Robotics and Automation*, pages 511–516, May 2012.

[48] Manoj Srinivasan and Andy Ruina. Computer optimization of a minimal biped model discovers walking and running. *Nature*, 439(7072):72–5, January 2006.

[49] R B Stein and C Capaday. The modulation of human reflexes during functional motor tasks. *Trends Neurosci.*, 11:328–332, 1988.

[50] F Sup, H A Varol, J Mitchell, T J Withrow, and M Goldfarb. Self-contained powered knee and ankle prosthesis: Initial evaluation on a transfemoral amputee. *IEEE Int Conf Rehabil Robot*, pages 638–644, 2009.

[51] Darryl G. Thelen, Frank C. Anderson, and Scott L. Delp. Generating dynamic simulations of movement using computed muscle control. *Journal of Biomechanics*, 36(3):321–328, March 2003.

[52] Brian R Umberger. Stance and swing phase costs in human walking. *Journal of the Royal Society, Interface / the Royal Society*, 7(50):1329–40, September 2010.

[53] Brian R Umberger, Karin G M Gerritsen, and Philip E Martin. A model of human muscle energy expenditure. *Computer methods in biomechanics and biomedical engineering*, 6(2):99–111, April 2003.

[54] Arthur J van Soest and Maarten F Bobbert. The contribution of muscle properties in the control of explosive movements. *Biological Cybernetics*, 69:195–204, 1993.

[55] David A. Winter. Biomechanical Motor Patterns in Normal Walking. *Journal of Motor Behavior*, 15(4):302–330, 1983.

[56] Jack M. Winters. Hill-Based Muscle Models: A Systems Engineering Perspective. In Jack M. Winters and S.L-Y. Woo, editors, *Multiple Muscle Systems: Biomechanics and Movement Organization*, chapter 5, pages 69–93. Springer-Verlag, 1990.

[57] R. C. Woledge, N. A. Curtin, and E. Homsher. *Energetic Aspects of Muscle Contraction.* Academic Press, Waltham, MA, 1985.

[58] www.renishaw.com.

[59] G T Yamaguchi, A G Sawa, D W Moran, M J Fessler, and J M Winters. A Survey of Human Musculotendon Actuator Parameters. In Jack M. Winters and S.L-Y. Woo, editors, *Multiple Muscle Systems: Biomechanics and Movement Organization.* Springer-Verlag, 1990.

[60] Felix E. Zajac. Muscle and Tendon: Properties, Models, Scaling, and Application to Biomechanics and Motor Control. *Critical reviews in biomedical engineering*, 17(4):359–411, 1989.